UiO **University of Oslo**

Jørgen Eriksson Midtbø

The low-energy enhancement
An experimental and theoretical study of nuclear level densities and γ-ray strength functions

Thesis submitted for the degree of Philosophiae Doctor

Department of Physics
Faculty of Mathematics and Natural Sciences

2019

For my mother, Nina, and my daughter, Dagny Ingebjørg, both of whom have inspired me tremendously.

Samandrag

Struktur og dynamikk i atomkjernar som vert eksiterte til høg energi, kan skildrast ved hjelp av konsepta nivåtettleik og gamma-styrkefunksjon. Desse storleikane finn bruksområde i mange ulike fagfelt, frå nukleærmedisin til astrofysikk. I denne avhandlinga studerer eg nivåtettleikar og gamma-styrkefunksjonar ved bruk av både teoretiske og eksperimentelle metodar. Nivåtettleiken og styrkefunksjonen til den eksotiske, nøytronrike atomkjernen ^{70}Ni har vorte målt ved hjelp av β-Oslometoden. Eksperimentet syner at kjerna har eit forsterka sannsyn for utsending av gammastråling med låg energi. Ved bruk av storskala skalmodelrekningar finn eg prov på at denne lågenergi-forsterkinga truleg kjem av magnetisk dipolstråling. Vidare gjer eg ei kartlegging der skalmodellen vert nytta i berekning av gamma-styrkefunksjonar i fleire hundre atomkjernar. Lågenergi-forsterkinga finst nesten over alt, og eg trekk ut systematiske tilhøve i utviklinga av forsterkinga som funksjon av proton- og nøytrontal. Skalmodellen vert òg nytta til å rekne ut den totale dipol-styrkefunksjonen til ^{51}Ti, i nydeleg samsvar med dei eksperimentelle målingane, og til å finne spinnfordelingar i ^{59,60}Ni. På den eksperimentelle sida angrip eg problemet med talfesting av usikkerheiter i Oslometoden. Eg presenterer ein full reimplementasjon av Oslometode-programvara som legg til rette for å køyre usikkerheitene gjennom metoden ved bruk av Monte Carlo-teknikkar.

Abstract

Structural and dynamical properties of nuclei at high excitation energies can be described by the concepts of nuclear level density and γ-ray strength function. These, in turn, find applications in a wide range of fields, from nuclear medicine to astrophysics. In this thesis, I study level densities and γ-ray strength functions by both experimental and theoretical methods. The level density and strength function of the exotic, neutron-rich nucleus ^{70}Ni has been measured by means of the β-Oslo method. The experiment reveals the presence of an enhanced γ-ray strength at low energies. Through use of large-scale shell-model calculations, I find evidence that this low-energy enhancement is likely to consist of magnetic dipole radiation. Furthermore, I perform a survey where the shell model is applied to calculations of γ-ray strength functions in several hundred nuclei. The low-energy enhancement is found to be near-universally present, and systematic trends in its evolution as function of proton and neutron number are inferred. The shell model is also used to calculate the total dipole strength function of ^{51}Ti, obtaining excellent agreement with experiments, and to infer spin distributions in ^{59,60}Ni. On the experimental side, the problem of uncertainty quantification in the Oslo method is tackled, and I present a full reimplementation of the Oslo method software that enables complete uncertainty propagation through the method by means of Monte Carlo techniques.

Preface

This thesis is submitted in partial fulfillment of the requirements for the degree of *Philosophiae Doctor* at the University of Oslo. The research presented here is conducted under the supervision of Dr. Ann-Cecilie Larsen, Dr. Therese Renstrøm, Professor Sunniva Siem and Dr. Signe Riemer-Sørensen.

The thesis is a collection of five papers, presented in chronological order. The papers are preceded by introductory chapters that relate them together and provide background information and motivation for the work.

Acknowledgements

List of Papers

Paper I: A. C. Larsen, J. E. Midtbø, M. Guttormsen, T. Renstrøm, S. N. Liddick, A. Spyrou, S. Karampagia, B. A. Brown, O. Achakovskiy, S. Kamerdzhiev, D. L. Bleuel, A. Couture, L. Crespo Campo, B. P. Crider, A. C. Dombos, R. Lewis, S. Mosby, F. Naqvi, G. Perdikakis, C. J. Prokop, S. J. Quinn, and S. Siem. *Enhanced low-energy γ-decay strength of* ^{70}Ni *and its robustness within the shell model*, Phys. Rev. C **97**, 054329 (2018), doi:10.1103/PhysRevC.97.054329, arXiv:1805.00856 [nucl-ex]

Paper II: J. E. Midtbø, A. C. Larsen, T. Renstrøm, F. L. Bello Garrote and E. Lima. *Consolidating the concept of low-energy magnetic dipole decay radiation*, Phys. Rev. C **98**, 064321 (2018), doi:10.1103/PhysRevC.98.064321, arXiv:1807.04036 [nucl-th]

Paper III: T. Renstrøm, G. M. Tveten, J. E. Midtbø, H. Utsunomiya, O. Achakovskiy, S. Kamerdzhiev, B. Alex Brown, A. Avdeenkov, T. Ari-izumi, A. Görgen, S. M. Grimes, M. Guttormsen, T. W. Hagen, V. W. Ingeberg, S. Katayama, B. V. Kheswa, A. C. Larsen, Y.-W. Lui, H.-T. Nyhus, S. Siem, D. Symochko, D. Takenaka, and A. V. Voinov. *Experimental γ-decay strength in* ^{59,60}Ni *compared with microscopic calculations*, arXiv:1804.08086 [nucl-ex]. *Submitted to Phys. Rev. C.*

Paper IV: S. N. Liddick, A. C. Larsen, M. Guttormsen, A. Spyrou, B. P. Crider, F. Naqvi, J. E. Midtbø, F. L. Bello Garrote, D. L. Bleuel, L. Crespo Campo, A. Couture, A. C. Dombos, F. Giacoppo, A. Görgen, K. Hadynska-Klek, T. W. Hagen, V. W. Ingeberg, B. V. Kheswa, R. Lewis, S. Mosby, G. Perdikakis, C. J. Prokop, S. J. Quinn, T. Renstrøm, S. J. Rose, E. Sahin, S. Siem, G. M. Tveten, M. Wiedeking, and F. Zeiser. *Benchmarking the extraction of statistical neutron capture cross sections on short-lived nuclei for applications using the β-Oslo method. Submitted to Phys. Rev. C.*

Paper V: J. E. Midtbø, A. C. Larsen, T. Renstrøm, F. L. Bello Garrote, and E. Lima. *A new software implementation of the Oslo method with complete uncertainty propagation*, arXiv:1904.13248 [physics.comp-ph]. *To be submitted to Nucl. Instrum. Methods Phys. Res. A.*

Contents

Contents

List of Figures

Chapter 1

Introduction

The atomic nucleus is arguably among the most difficult microscopic physical systems in the world to model. It is a many-body system that interacts with itself and the environment through all the four forces of nature.[1] On the energy scale at which atomic nuclei exist as bound entities, the parameters that govern their interactions are difficult to derive from fundamental theories of physics. Matters are worsened further when we want to study the behaviour of highly excited nuclear states. They are characterised by a high density of energy levels, which makes it experimentally difficult to resolve them individually through techniques like γ-ray spectroscopy. The high excitation energy and density of levels also makes theoretical modelling difficult, owing to the enormous complexity of the quantum-mechanical wave functions involved.

On the other hand, the complexity of the problem is also what makes studies of atomic nuclei so interesting. Nuclei are highly diverse, ranging from the single proton at the core of the hydrogen atom, via few-particle systems such as α particles, that can be solved with impressive precision by microscopic *ab initio*-methods, to heavy nuclei, such as uranium, consisting of hundreds of strongly interacting protons and neutrons, where the most successful models are inspired by fluid and statistical mechanics more than by particle physics. When traversing the nuclear chart, the breadth of nuclear physics becomes apparent: Some nuclei are spherical, others are shaped like rugby balls or even pears. Some nuclei are stable, others are radioactive and decay, by charge-changing processes or nuclear fission. Some nuclei have simple, ordered excitation-energy levels, others exhibit complicated level structures with levels of differing nuclear shapes. However, common to all nuclei is that the density of levels increases with excitation energy, bringing with it quantum-mechanical wave functions and transition probabilities of increasing chaoticity. In order to describe these nuclear states in a microscopic theory, quantum-mechanical many-body wave functions with millions or even billions of components are required. This can be achieved, for example, by use of large-scale shell-model calculations.

Knowledge of nuclear behaviour at high excitation energy is a vital component in several other fields of science, from production of medical isotopes, via nuclear power and nuclear forensics, to astrophysics. Most central to this thesis is *heavy-element nucleosynthesis*, which concerns the formation of elements heavier than iron in our universe. Heavy-element nucleosynthesis occurs through two main processes, known as the slow (s) and rapid (r) neutron-

---

[1]Although they are not all equally strong. Notably, the interaction of gravity is many orders of magnitude weaker than the strong, weak and electromagnetic interactions, and can safely be neglected for nuclear-physics applications. Still, as atomic nuclei make up the vast majority of the mass of matter around us, the gravitational pull on each and every nucleus sums up to the highly non-negligible effects of gravity on macroscopic length scales.

capture processes. The s process, taking place in late stages of stellar burning in asymptotic giant-branch stars, proceeds by alternating neutron capture and β decay on stable seed nuclei to produce elements as heavy as lead [1]. Much less is known of the r process, although a giant leap forward was taken in 2017 with the discovery of a neutron-star merger with confirmed of r-process nucleosynthesis [2]. The r process consists of rapid, successive neutron captures by bombardment of neutrons on unstable, very neutron-rich nuclei. Much information is lacking on the neutron-rich nuclei in question, concerning everything from lifetimes and binding energies to neutron-capture cross sections – to the degree that even the exact 'path' of the r process in the nuclear chart is unknown [3]. Studies of statistical nuclear properties help mitigate this, providing theoretical and experimental insights that constrain the models of both s- and r-process nucleosynthesis.

When writing this thesis, I have tried to follow a principle of thoroughness. I want the text to be as self-sufficient as possible, by writing out arguments and explanations in detail. Particularly so for the chapter on the Oslo method, where few comprehensive reviews exist, and many of the crucial details are scattered throughout various published articles. I have done this mostly to force myself to understand the details properly, but also in an effort make it accessible to readers who are in the process of learning the subject, such as master students.

The thesis is structured as follows. In Chapter 2, I begin with a discussion of nuclei through the lens of theoretical models. The main focus of the chapter is on the nuclear shell model and configuration-interaction theory, which forms a cornerstone of the research presented in this thesis. Chapter 3 proceeds by going into the subject of *statistical* nuclear behaviour – nuclear state and decay properties at high excitation energies, with concepts such as level densities and γ-ray strength functions. I put particular emphasis on the *low-energy enhancement* of the γ-ray strength function, discussing the theoretical and experimental evidence for this phenomenon, including my own research contributions. I then make a leap over to the experimental side, devoting Chapter 4 to the Oslo method, a technique for studying nuclear behaviour in the statistical regime. Here, I also present the work I have done on a reimplementation of the Oslo method software tools, that provides novel capabilities for quantification of uncertainties in the Oslo method. In Chapter 5, I give my summary and outlook, before presenting the scientific articles that make up this thesis, with a short introduction to and a full reprinting of each of them, in Chapter 6.

Chapter 2

Nuclear models

In this chapter, I discuss theoretical modelling of the atomic nucleus. I will briefly discuss the vastly different models that exist to describe the same system, and why there isn't a single unified model to describe nuclear physics. The main focus of the chapter is on one particular model, the nuclear shell model. Since large-scale shell-model calculations constitute a large part of the research that comprises this thesis, I go into details about the mathematical framework of configuration-interaction shell-model calculations, as well as some of the technical aspects of performing large-scale shell-model calculations. At the end of the chapter, I discuss the different effective interactions that I have used in my work.

2.1 The nuclear problem

The atomic nucleus is by definition a subatomic system. The realm of subatomic physics is described at the fundamental level by one of the most elegant, and also well-tested, theories of modern physics, namely the Standard Model of particle physics [4]. According to the Standard Model, the nucleus consists of elementary particles called quarks. The quarks are spin-1/2 fermions, and they are present in the nucleus in two distinct species, called up (u) and down (d). They have fractions of the elementary charge of $+2/3e$ and $-1/3e$, respectively. The quarks tend to bind together in threes and form stable, compound particles called nucleons. The nucleons are of two varieties: protons (uud) and neutrons (udd). The protons have charge $+e$, while the neutrons have charge zero. The quarks are bound together by the strong force of quantum chromodynamics (QCD), mediated by force-carrying bosons called gluons. The residual fields of the strong force on the surface of nucleons is also what makes them bind together with other nucleons – however, the interaction has very short range.

Due to a peculiarity of quantum field theory known as renormalisation [4], the strength of the interaction between quarks depends on the energy scale at which they interact, and the interaction is stronger the less energy is involved. For quarks bound inside atomic nuclei, the force is very strong and does not allow a perturbative expansion. This is a major problem for theoretical nuclear physics. At higher energies, such as those involved when protons collide at the Large Hadron Collider at CERN [5], the interaction is much weaker and QCD can be calculated perturbatively.

In addition to the strong force, the quarks are subject to the electroweak interaction, mediated by the $W^{\pm}$ and Z^0 bosons and the photon. The electroweak interaction gives rise to Coulomb repulsion between the positively-charged protons within the nucleus. Furthermore, through exchange of the charged $W^{\pm}$
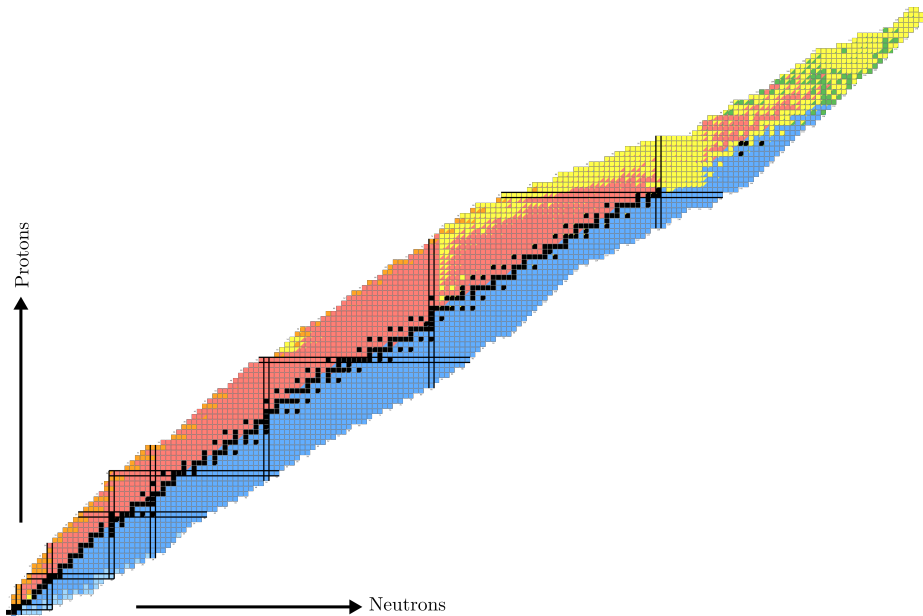
Figure 2.1: The chart of atomic nuclei. Magic numbers of Z and N are indicated by solid lines. The nuclei in black squares are stable. Unstable nuclei are coloured according to their primary mode of decay: β^+ (red); β^- (blue); fission (green); proton emission (orange); and neutron emission (light blue). Secondary modes of decay are indicated by insets of a different colour. The figure is made using the code in Ref. [6] with experimental data from Ref. [7].

bosons, an up quark can change into a down quark and vice versa, which means that protons and neutrons can transform into each other. The process requires the emission of an electron or positron, $e^\pm$ to conserve the electromagnetic charge, as well as a very light particle known as an electron neutrino (or antineutrino), ν_e ($\bar{\nu}_e$). Spontaneous conversion between protons and neutrons, with emission of an electron (positron) together with an electron antineutrino (neutrino), is known as $\beta^\pm$ decay.

Since the quarks are strongly confined inside nucleons, it means that for low-energy nuclear physics, the nucleons are the relevant degrees of freedom. This is both a blessing and a curse: On the one hand, one does not have to worry about the quarks, but on the other, the force between the nucleons, which is the residual of the forces between the quarks, cannot be calculated easily from QCD. This problem has led particle physics and nuclear physics, although they are closely related, into very different paradigms.

The playground of nuclear physics is the chart of nuclides, shown in Fig. 2.1. The black 'line' traced out by the stable nuclei is known as the valley of β stability. Many more nuclei than those shown in Fig. 2.1 are expected to be bound, but have not yet been discovered experimentally. Figure 2.2 shows a theoretical
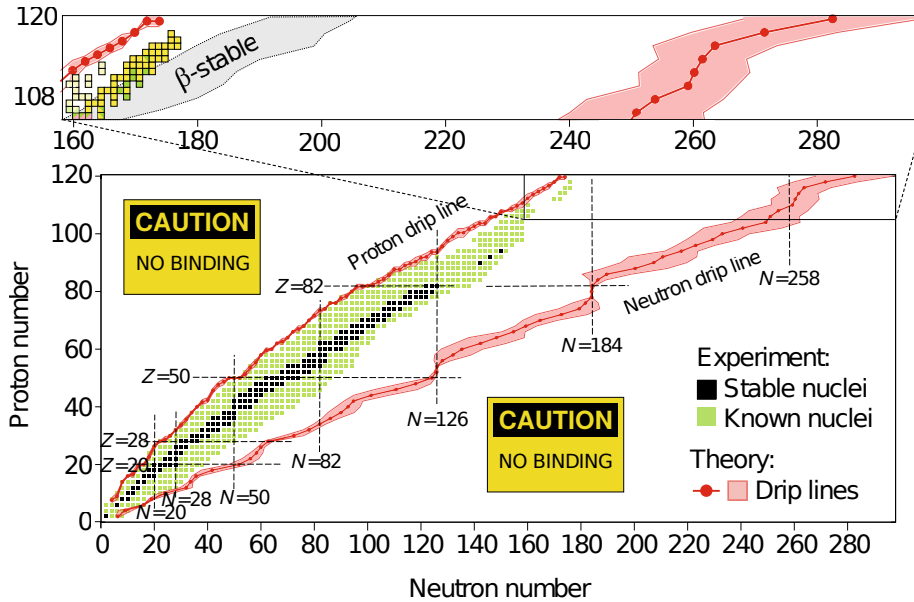
Figure 2.2: Theoretical prediction of the edges of the landscape of bound nuclei. The figure is reprinted with permission from Ref. [8].

prediction of the limits of the nuclear landscape, adapted from Ref. [8]. The ridges of the nuclear valley are bordered to the left by the *proton drip line*, where the addition of more protons makes the nucleus fragment, and to the right by the *neutron* drip line, where the addition of more neutrons does the same. Notice that the distance is much larger from the β-stable valley to the neutron drip line than to the proton drip line, due to the strong Coulomb repulsion between protons. As the rapid neutron capture (r) process of astrophysical nucleosynthesis is expected to take place at, or close to, the neutron drip line, Fig. 2.2 illustrates the vast amount of work remaining in order to obtain a good understanding of the nuclear-physics conditions for the r process [3].

2.2 Nuclear models

Many models exist to describe nuclei that are both quantitatively and qualitatively very different. One conceptually simple, yet powerful, model is the liquid drop model [9], which includes the Bethe-Weizäcker formula (also known as the semi-empirical mass formula) [10]. The Bethe-Weizäcker formula is based on modelling the nuclear binding energy (from which one can derive the nuclear mass) by a sum of terms describing different aspects of the nucleus: volume, surface area, electrical Coulomb repulsion between protons, quantum-mechanical pairing effects and the asymmetry between protons and neutrons. The name liquid drop model is due to the similarity with the physics of a drop of liquid:
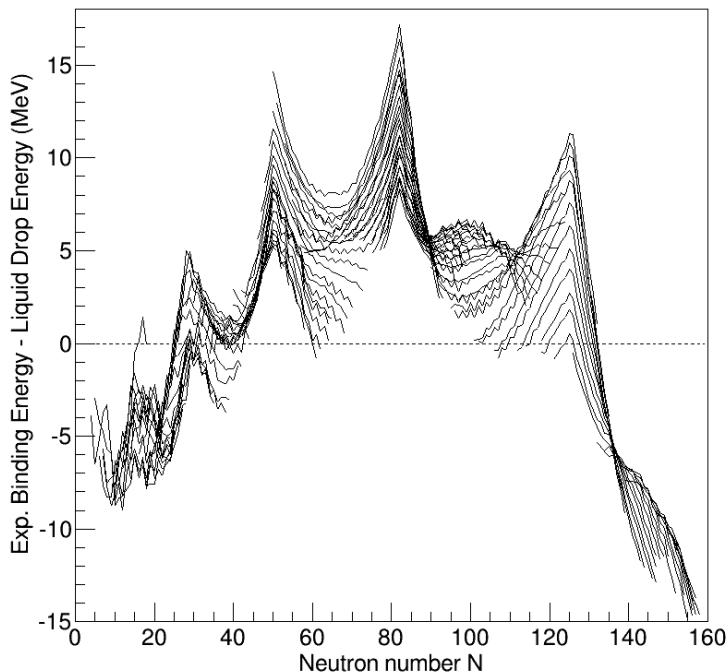
Figure 2.3: Difference between the liquid drop model prediction and experimental measurements, as function of neutron number. The figure is reprinted with permission from Ref. [13].

The stability of the drop depends on the ratio between volume and surface. The surface tension holds the drop together against the repulsive pressure between the molecules within the volume, but only if the drop is small enough. The liquid drop model is very successful at describing the gross properties of nuclei. For instance, it correctly predicts that the binding energy per nucleon has a maximum in the middle of the nuclear chart, at about ^{56}Fe. It also explains why some isotopes are more tightly bound, and thus more stable, than others, *i.e.* the valley of β stability in Fig 2.1. The liquid drop model has also been successfully applied to explain numerous other facets of nuclear behaviour and dynamics, such as collective motion giving rise to rotational and vibrational spectra [11] and fission [12].

2.2.1 Magic numbers

It is well known that there are systematic differences between the liquid drop prediction and experimental values, as shown in Fig. 2.3. This discrepancy is due to a quantum mechanical effect similar to that which makes atomic electrons structure themselves in electron shells. For that reason, it is known as

nuclear shell structure. Evidence for nuclear shell structure was discovered independently by Goeppert Mayer [14, 15] and Haxel, Jensen and Suess [16] in 1949, earning Goeppert Mayer and Jensen the Nobel Prize in Physics for 1963 [17].

The shell model was a fantastic innovation because it naturally explains the *magic numbers*, the tendency for nuclei with a certain number of protons and/or neutrons to exhibit an additional degree of stability relative to their neighbours. The magic numbers are the reason for the discrepancies in Fig. 2.3. The experimentally verified magic numbers are 2, 8, 20, 28, 50, 82 and 126. Protons and neutrons are independent subjects to the magic numbers. A nucleus with a magic number of both protons and neutrons is called a doubly-magic nucleus, and such nuclei are very stable compared to their neighbours. The maxima of the peaks in Fig. 2.3 are located at the magic numbers.

2.3   Constructing the shell model

The shell model is based on a mean-field model for the nucleus, where each nucleon moves in an average, spherically symmetric potential set up by all the other nucleons. However, the crucial insight that Goeppert Mayer and the other inventors had, was the inclusion of a strong *spin-orbit* term which makes the nucleon energy sensitive to the coupling between its orbital angular momentum and spin. I will now go through the mathematical construction of the shell model.

Assume that each nucleon is a non-interacting spin-1/2 fermion moving in a spherical three-dimensional harmonic oscillator potential set up by the other nucleons. Hence, the time-independent Schrödinger equation is

$$\hat{H}\psi(\vec{r}) = \left(-\frac{\hbar^2}{2m}\nabla^2 + V(\vec{r})\right)\psi(\vec{r}) = E\psi(\vec{r}), \qquad (2.1)$$

where $\hat{H}$ is the Hamiltonian operator, $\psi(\vec{r})$ is the wave function, $\hbar = 197.3\,\text{eV}\,\text{nm}/c$ is Planck's reduced constant, $m \approx 0.94\,\text{GeV}/c^2$ is the mass of the nucleon and E is its energy. The harmonic oscillator potential is

$$V = \frac{1}{2}\omega^2(x^2 + y^2 + z^2), \qquad (2.2)$$

where ω parametrises the strength of the oscillator. This gives rise to stationary states with energy levels $E_{n_x n_y n_z} = \hbar\omega(n_x + n_y + n_z + 3/2)$. By transforming to spherical coordinates, $(x, y, z) \rightarrow (r, \theta, \phi)$, the solutions may equivalently be described by the quantum numbers (n, l, m), where

$$n_x + n_y + n_z = 2(n-1) + l. \qquad (2.3)$$

Here, n is called the radial quantum number, l the orbital quantum number and m the magnetic quantum number. The energy levels are degenerate in m. In these coordinates, the eigenstate wave functions are

$$\psi_{nlm}(\vec{r}) = R_{nl}(r)Y_{lm}(\theta, \phi). \qquad (2.4)$$

N	n, l	orbital	parity
0	1, 0	$1s$	+
1	1, 1	$1p$	−
2	2, 0	$2s$	+
	1, 2	$1d$	+
3	2, 1	$2p$	−
	1, 3	$1f$	−
4	3, 0	$3s$	+
	2, 2	$2d$	+
	1, 4	$1g$	+

Table 2.1: Table of quantum numbers for the first four major shells of the three-dimensional harmonic oscillator.

Under the operation of parity change, $\hat{P}$, which turns right-handed coordinate systems into left-handed ones, the spherical harmonics Y_{lm} transform as

$$\hat{P}Y_{lm}(\theta, \phi) = (-1)^l Y_{lm}(\theta, \phi), \tag{2.5}$$

while the radial wave function $R_{nl}(r)$ is invariant under parity transformations. In other words, the solutions ψ_{nlm} are eigenstates of parity with eigenvalue ± 1. By introducing the *major shell number* $N = 2(n-1) + l$, the solutions can be categorised as shown in Table 2.1. Spectroscopic notation is adopted, labelling the orbitals as nl with $n = 1, 2, 3, ..., l = s, p, d, f, g, h, i, ...$ corresponding to $l = 0, 1, 2, 3, 4, 5, 6, ...$ By adding a spin-orbit term to the potential, so that (in spherical coordinates)

$$V = \frac{1}{2}\omega^2 r^2 + C\hat{l} \cdot \hat{s}, \tag{2.6}$$

the energy eigenvalues are modified to

$$E_{nlj} = \hbar\omega \left[2(n-1) + l + 3/2\right] + C\frac{\hbar^2}{2} \left\{ \begin{matrix} -l \\ l+1 \end{matrix} \right\} \text{ for } j = \left\{ \begin{matrix} l+1/2 \\ l-1/2 \end{matrix} \right\}. \tag{2.7}$$

The solutions $\psi_{nljj_z}(\vec{r})$ to the new Hamiltonian remain eigenstates of parity. The spectroscopic notation is extended as nl_j, so that *e.g.* $1f_{5/2}$ encodes $n = 1$, $l = 3$, $j = 5/2 = l - 1/2$. A level with a given nl_j is called an *orbital*. The nucleons, being fermions, are subject to the Pauli exclusion principle, whereby no two particles can occupy the same quantum state. However, for a given total angular momentum j there exist $2j + 1$ physically separable sub-states of different z projection $j_z \in \{-j, -j+1, ..., j-1, j\}$. Hence, each orbital has room for $2j + 1$ nucleons. A schematic representation of the resulting energy level scheme is shown in Fig. 2.4. The left hand side of the figure shows the energy levels without the spin-orbit term. Moving towards the right hand side,
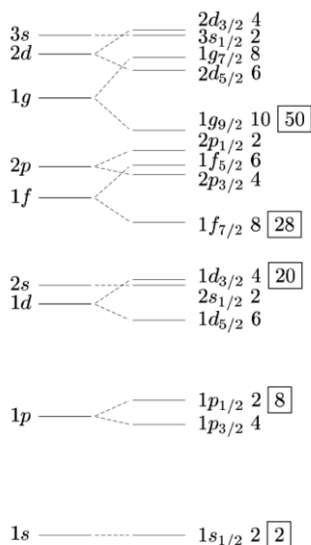
Figure 2.4: The orbital structure of the shell model. The figure is from Ref. [18].

the spin-orbit coupling is turned on and the spin degeneracy is lifted.[1] The numbers marked by squares indicate the running sum of the number of available states below, and they are identical to the magic numbers. The magic numbers appear where there are large gaps between neighbouring orbitals – meaning that the energy required to excite a nucleon between the orbitals is high, so that the nucleonic configuration becomes strongly bound. The effects of the spin-orbit coupling are evident, where for example the $1g$ level is split into $1g_{7/2}$-$1g_{9/2}$, forming the shell gap at $N/Z = 50$. This also changes the simple picture where all the orbitals in each major shell N have the same parity. Orbitals of opposing parity being lowered by the spin-orbit interaction into the major shell below are called *intruder orbitals*. In the case of $1g_{9/2}$, it is a positive-parity orbital intruding in the intrinsically negative-parity major shell $N = 3$.

The configuration of a nucleus is the product of the configurations of each of its individual nucleons. The total angular momentum, or total spin, J of a nucleus is the vector sum of the angular momenta of all its constituent nucleons, and the total parity π is the product of the parities of each individual nucleon. Hence, to go from the one-particle shell model to a model for many interacting nucleons seems complicated. However, fortunately, nucleons prefer to couple in pairs to cancel out their angular momenta. This leads to the astounding fact that all even-even nuclei, that is nuclei with an even number of both protons and neutrons, have $J^{\pi} = 0^{+}$ in their ground states. Furthermore, in many

---

[1]The energy of different members of the same major shell in Fig. 2.4 is not completely degenerate even without spin-orbit splitting. This is because the potential used for this figure also includes an orbit-orbit splitting term [18].

cases it leads nuclei with an odd number of protons or neutrons to have their spin dictated by the last, unpaired nucleon. Thus, for example, ^{41}Ca, with one unpaired neutron added on top of the doubly-magic ^{40}Ca, has $J^\pi = 7/2^-$ in its ground state, which can be understood as the last neutron occupying $1f_{7/2}$, which is in the negative-parity fp shell.

2.3.1 Nuclear deformation

For nuclei in regions away from magic numbers, the assumptions underpinning the simple shell-model picture break down, notably the assumption of a spherical mean field. In fact, most nuclei are deformed. Nuclear deformation can be described by a modification of the shell model where spherical symmetry is broken by decoupling the harmonic oscillator strengths of the axes (Eq. (2.2)). This gives rise to the Nilsson model [19]. Figure 2.5 shows how the single-particle energies of the orbitals, and hence the shell gaps and magic numbers, change as function of deformation. Notice how the deformation lifts the energy degeneracy of the magnetic sub-states. The gradient of the orbitals depends on the angular momentum, with the largest momenta getting the steepest ascent and descent. Hence, orbitals that are far from the Fermi surface in the spherical shell model can be key components of the wave functions for deformed nuclei. For this reason, orbitals of comparatively high l in a given mass region (such as the $g_{9/2}$ orbital in the $fpg_{9/2}$ shell) are sometimes referred to as *deformation-driving* orbitals.

2.4 Electromagnetic transitions

Nuclei can transition between their different quantum states by emission or absorption of electromagnetic radiation, *i.e.* photons. Electromagnetic radiation has a multipole expansion whereby it is decomposed in electric and magnetic components of increasing multipolarity:

$$XL = E1, M1, E2, M2, \text{ etc.} \tag{2.8}$$

For nuclear transitions, there is a strong suppression of higher-order multipole radiation. The lowest-order, $L = 1$, is preferred, and for a given L, E is preferred over M. This means that a transition between two quantum levels will proceed by as low multipole order as possible. However, the transitions are also subject to *selection rules*. They dictate that a transition between levels with angular momenta J_1, J_2 can only proceed via transitions with $L \geq |J_1 - J_2|$. Transitions between levels both having $J = 0$ are not allowed. The parities of the intial and final levels must be equal for $M1, E2, M3, ...$, and opposite for $E1, M2, E3, ...$ Since low L are favoured, this leads nuclei to prefer to transition between levels with small angular momentum differences.
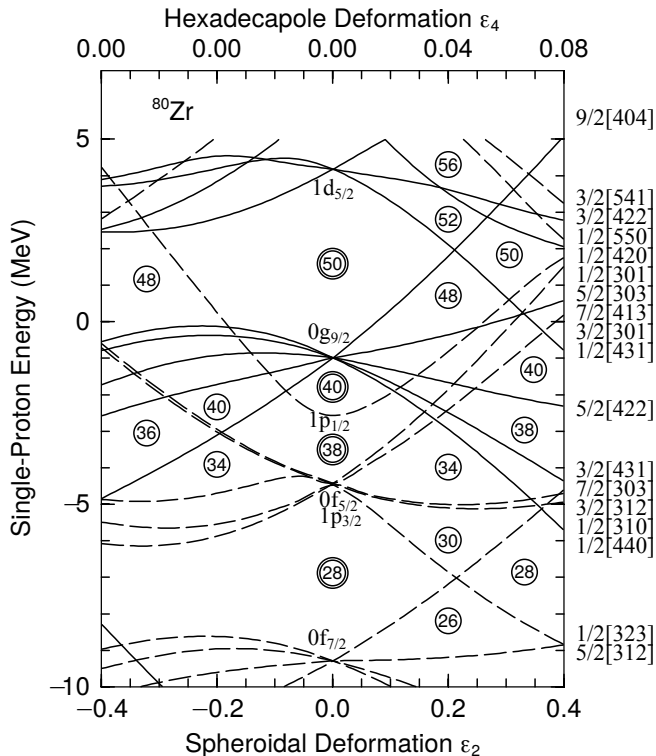
Figure 2.5: Single-particle orbitals in the Nilsson model of deformed nuclei. The figure shows how the energies of the orbitals are modified as function of the deformation parameter. The figure is reprinted with permission from Ref. [20].

2.4.1 Transition matrix elements

The nucleus is tightly bound together, with a binding energy per nucleon of about 8 MeV for most nuclei [21]. Thus, the total energy of an eigenstate of the many-body nuclear Hamiltonian is negative and of the order of hundreds of MeV. The energy difference between excited states in a nucleus, on the other hand, is of the order of a few MeV. This large energy separation means that when calculating transition probabilities between excited states, first-order perturbation theory is usually sufficient. The transition rate, *i.e.* the transition probability per second, for a transition between states $|i\rangle$ and $|f\rangle$ (carrying some given total angular momenta and magnetic sub-states J_i, m_i and J_f, m_f) via multipolarity XL, is given to first order in perturbation theory by [22]

$$T_{i \to f}(XL\mu) = \frac{8\pi(L+1)}{L\hbar[(2L+1)!!]^2} \left(\frac{E_\gamma}{\hbar c}\right)^{2L+1} |\langle f|\hat{O}_{L\mu}|i\rangle|^2, \qquad (2.9)$$

where $\hat{O}_{L\mu}$ is the multipole operator for electromagnetic transitions involving a photon with angular momentum L and z-projection μ, and $(2L+1)!! =$

11

$1 \cdot 3 \cdots (2L + 1)$. The dependence on z projection can be removed by averaging over initial and summing over final m states:

$$\sum_{\mu, m_f} |\langle J_f m_f | \hat{O}_{L\mu} | J_i m_i \rangle|^2 \equiv \frac{1}{2J_i + 1} |\langle J_f || \hat{O}_{L\mu} || J_i \rangle|^2 \equiv B(XL; J_i \to J_f), \quad (2.10)$$

where we have defined the *reduced transition matrix element* $|\langle a || \hat{O} || b \rangle|^2$ and the *reduced transition strength* $B(XL; J_i \to J_f)$.

For the case of $M1$ radiation, which is central to this thesis, the transition matrix elements of transitions between shell model orbital states are composed of an orbital and a spin term, and for a transition between orbitals $a = n_a l_{a j_a}$, $b = n_b l_{b j_b}$, it is given by [23]

$$\langle a | \hat{O}(M1) | b \rangle = \sqrt{\frac{9}{8\pi}} (-1)^{l_a + j_a + 3/2} \sqrt{(2j_a + 1)(2j_b + 1)} \begin{Bmatrix} 1/2 & 1/2 & 1 \\ j_b & j_a & l_a \end{Bmatrix}$$
$$\times \delta_{l_a, l_b} \delta_{n_a, n_b} g_q^s \mu_N \qquad (2.11)$$
$$+ \sqrt{\frac{3}{4\pi}} (-1)^{l_b + j_b + 3/2} \sqrt{(2j_a + 1)(2j_b + 1)} \begin{Bmatrix} l_a & l_b & 1 \\ j_b & j_a & l_a \end{Bmatrix}$$
$$\times \delta_{l_a, l_b} \delta_{n_a, n_b} \sqrt{l_a(l_a + 1)(2l_a + 1)} g_q^l \mu_N$$

Here, the curly braces are Wigner $6j$ symbols, which are coupling coefficients for the combination of the angular momentum vectors involved in the decay, and g_q^s and g_q^l are gyromagnetic ratios, factors that decide the strength of the magnetic coupling. Their free-nucleon values are $g_p^{l,\text{free}} = 1$, $g_p^{s,\text{free}} = 5.586$ for protons and $g_n^{l,\text{free}} = 0$, $g_n^{s,\text{free}} = -3.826$ for neutrons. The nuclear magneton μ_N is $\mu_N = e\hbar/2m_p = 0.10515 ce$ fm, where $m_p = 938.27$ MeV/c^2 is the proton mass [24].

2.5 The shell model as a configuration-interaction basis

The shell model is a powerful conceptual model, enabling us to understand many of the gross properties of the nuclear chart, such as the magic numbers. However, real nuclei are much more complicated than what the simple shell model picture of non-interacting nucleons allows. In reality, all the nucleons interact with each other, and to obtain a good microscopic description of nuclear properties, these interactions should be modelled. A model where interactions between all nucleons (or all constituents of other many-body quantum systems) are modelled is called a *full configuration interaction theory* [25].

Since the nucleus is so complex, it is imperative for both model complexity and computational costs to find a way to reduce the number of degrees of freedom as much as possible without losing the relevant physics. From this viewpoint, the shell model is convenient since it naturally separates out certain degrees of freedom as more relevant than others. Specifically, one can exploit the magicity of certain nuclei by assuming that they form an inert, or closed,

core, and approximate the nucleus as being described by the extra nucleons outside the core, the *valence* nucleons.

This opens up the possibility to perform configuration-interaction calculations on systems that are way too complex to handle in full configuration. Some much-used closed cores are ^{16}O, ^{40}Ca, ^{48}Ca, ^{56}Ni, ^{100}Sn and ^{132}Sn. Typically, a given core is used for studies of nuclei within the major shell above the closure. For example, ^{40}Ca is much used as a core for calculating nuclei in the fp shell, such as isotopes of Sc, Ti and Fe. It is also possible to exploit a closed core to study systems with fewer nucleons than the core, by treating the holes in the core as valence particles. In this thesis, I refer to configuration-interaction calculations with a closed core as *shell-model calculations*.

All shell-model calculations employ some form of restriction of the Hilbert space of available basis states, called a *truncation*. In principle, there are infinitely many possible single-particle states in the harmonic oscillator basis. Therefore, in addition to closing off the core, one has to limit the number of orbitals to include above the core. Calculations involving all orbitals down to zero energy are known as no-core shell-model calculations [26]. The choice of truncation and the resulting valence orbitals is called the model space of the calculation. A model space may encompass anything from one or a few orbitals, to a full major shell or even several major shells. A calculation involving excitations over a major shell gap is called an $X\hbar\omega$ calculation, referring to the number X of harmonic oscillator quanta of energy required for the excitation. It is even possible to use this as a truncation requirement, by allowing only configurations with at most N excitations across the shell gap. In Papers II [27] and IV in this thesis, I have employed such a $1\hbar\omega$ truncation. A calculation within a single major shell is sometimes called a $0\hbar\omega$ calculation.

Shell model calculations have been used extensively to predict and explain the structure of nuclei [26, 28, 29]. Since the dimensionality of the calculations grow quickly with the number of orbitals included, most shell-model calculations are performed within one major shell. This is often enough to capture many of the important facets, such as orbital occupation structure and transition rates, of the lowest-lying excited states of the nucleus. However, as the excitation energy increases, more and more high-energy configurations become accessible to the nuclear wave-functions, and a larger model space is required to give a realistic description. When calculating electromagnetic transitions, the selection rules also come into play. Because of the parity flip, calculations of $E1$ transitions within the shell model require the inclusion of orbitals from two major shells. $M1$ and $E2$ transitions can be calculated within $0\hbar\omega$.

A myriad of approaches and approximations to configuration-interaction calculations have surfaced over the years [26, 30–32]. One very successful example is the Monte-Carlo Shell Model (MCSM) of Otsuka *et al.* [29].[2] Based on sampling within subsets of the Hilbert space, the method can tackle model spaces far out of reach of full-configuration calculations. Another interesting avenue is the symplectic shell model (*e.g.* [33]), where symplectic groups are used to con-

---

[2]Not to be confused with the Shell model Monte Carlo (SMMC) method [31].

struct the Hilbert space in terms of monopole and quadrupole excitations, in a manner very different from the single-particle orbital picture. The symplectic shell model seems to give a promising description of deformed nuclei [34]. A third innovation, of particular interest to applications at high excitation energy, is the recently developed method of stochastic level density estimation in the shell model [35]. Rather than solve the Hamiltonian exactly, the method counts the number of eigenvalues within each excitation-energy bin. This makes it applicable to model spaces that are too large to be exactly diagonalised.

I note in passing that it is completely possible to describe deformed nuclei using the spherical shell model as a full-configuration basis [36]. However, to obtain a physical description it is necessary to include the deformation-driving orbitals, and this often requires large model spaces.

2.6 Effective interactions

When a suitable model space has been selected for the nucleus under study, there still remains the question of what forces govern the interactions. As discussed in the introduction, the forces between nucleons are the residual interactions from the colour dynamics of the QCD interaction between the constituent quarks, as well as the electroweak interactions responsible for charge-changing processes and protonic Coulomb repulsion. In principle, then, one should be able to calculate the effective interaction from the Standard Model of particle physics. In practice, however, this is not possible, because the strong interaction is not perturbative at the energy scale of low-energy nuclear physics. It means that a perturbative expansion of the interaction strengths is not guaranteed to contain terms of decreasing importance. There are techniques to get around this, such as lattice QCD [37], but they are not yet sufficiently developed to be extensively used for making effective interactions.

Another way to exploit insight from the Standard Model is through *effective field theory*. Here, one derives an approximate theory based on turning off degrees of freedom in QCD in a well-defined way [38]. Then one obtains a systematic theory involving nucleons, as well as one or several force-mediating bosons. The lightest charge-neutral effective boson, or *meson*, is the pion. This *chiral* effective field theory lends itself to perturbative expansions [38]. Still, the parameters of the meson-nucleon interactions must be fitted to data. With such an interaction at hand, there exist methods to calculate the effective interactions between nucleons in a given shell-model model space [39, 40].

The most brute-force way, however, of obtaining an effective shell model interaction is to simply fit the interaction parameters to experimental values. This is an optimisation problem: Make a guess for the interaction parameters, perform shell-model calculations to predict the level structure of some nuclei, compare to experimental values and update the parameters until reaching sufficient agreement. It is often advantageous to use a theoretically predicted interaction as a starting point for the optimisation search. This approach has led to many of the most-used shell model interactions on the market [41–43].

Some of these will be discussed in more detail below.

2.7 Performing shell-model calculations

To obtain the eigenstates of the shell model Hamiltonian, an advanced computational framework is required. I now discuss some aspects of this. The following is inspired by Ref. [23].

2.7.1 Many-body states

The first step is to choose and construct a representation of the basis of all available many-particle wave functions. Since the nucleons are fermions, the many-particle wave functions must be anti-symmetrised in order to obey the Pauli exclusion principle. The easiest way to construct the set of many-particle basis states is by taking products of the single-particle wave functions $\psi_i \equiv \psi_{nljj_z}(\vec{r})$ and anti-symmetrising them by writing them as so-called Slater determinants,

$$\phi_\mu(\vec{r}_1, \vec{r}_2, ..., \vec{r}_n) = \frac{1}{\sqrt{k!}} \begin{vmatrix} \psi_{\mu_1}(\vec{r}_1) & \psi_{\mu_1}(\vec{r}_2) & \dots & \psi_{\mu_1}(\vec{r}_n) \\ \psi_{\mu_2}(\vec{r}_1) & \psi_{\mu_2}(\vec{r}_2) & \dots & \psi_{\mu_2}(\vec{r}_n) \\ \vdots & \vdots & \ddots & \vdots \\ \psi_{\mu_n}(\vec{r}_1) & \psi_{\mu_n}(\vec{r}_2) & \dots & \psi_{\mu_n}(\vec{r}_n) \end{vmatrix}. \tag{2.12}$$

where $\mu = nljj_z$ and k is the number of particles. For computation efficiency in practice, the wave functions need to be represented as compactly and easily as possible. This is achieved with a formalism known as occupation representation or second quantisation. The basic idea is to represent the set of all N possible Slater determinants as a (very long) vector, where each position in the vector corresponds to a unique Slater determinant. A many-body wave function, which is a superposition of Slater determinants, can then be represented as a vector in this space,

$$\vec{x} = (x_1, x_2, ..., x_N). \tag{2.13}$$

The numbers x_i encode the amount of weight each Slater determinant, *i.e.* each orbital configuration, has in the wave function – hence the term occupation representation. In the formalism of second quantisation, the single-particle states ψ_i are represented using creation and annihilation operators $\hat{a}_i^\dagger, \hat{a}_i$, such that

$$|\psi_i\rangle = \hat{a}_i^\dagger |0\rangle, \tag{2.14}$$

$|0\rangle$ being the vacuum state or a closed, inert core. The operators are required to obey anti-commutation relationships,

$$\hat{a}_i \hat{a}_j + \hat{a}_j \hat{a}_i \equiv \{\hat{a}_i, \hat{a}_j\} = 0, \tag{2.15}$$

$$\hat{a}_i^\dagger \hat{a}_j^\dagger + \hat{a}_j^\dagger \hat{a}_i^\dagger \equiv \{\hat{a}_i^\dagger, \hat{a}_j^\dagger\} = 0. \tag{2.16}$$

This enforces the Pauli exclusion principle, since any repeated creation of the same single-particle state destroys the wave function: $\hat{a}_i^\dagger \hat{a}_i^\dagger |\Psi\rangle = 0$. We thus ensure that each single-particle state occurs only once. Any n-particle Slater determinant $|\phi_\mu\rangle$ can now be represented as a product of creation operators,

$$|\phi_\mu\rangle = \hat{a}_{\mu_1}^\dagger \hat{a}_{\mu_2}^\dagger \cdots \hat{a}_{\mu_n}^\dagger |0\rangle. \tag{2.17}$$

Solving the many-body problem amounts to finding the eigenvectors $\vec{v}_k$ and eigenvalues E_k of the many-body Hamiltonian H in this basis. It is customary to assume that the interactions between nucleons restrict themselves to two kinds: Single-particle interactions, *i.e.*, the interaction of a particle with the mean field set up by the core, and two-body forces between the valence nucleons. This is a simplification, as there will realistically be three-body and higher-order forces between the valence nucleons. However, the lack of higher-order forces can to some degree be accounted for by modifying the effective one- and two-body forces [26]. Letting $|i\rangle$ denote a single-particle state and $|kl; J\rangle$ a two-particle state coupled to spin J, the Hamiltonian can then be represented as a sum of terms:

$$H = \sum_{i=1}^{N} \varepsilon_i \hat{n}_i + \sum_{i,j} \sum_{k,l<i,j} \sum_{J} V_{ijklJ} \hat{T}_{ijklJ}, \tag{2.18}$$

where ε_i and $\hat{n}_i$ are the single-particle energy (SPE) and single-particle number operator, respectively, of orbital i, and V_{ijklJ} and $\hat{T}_{ijklJ}$ are the two-body matrix element (TBME) and two-body transition density, respectively, of each two-body configuration combination $ijklJ$. Here i, j and k, l are the single-particle orbitals of the nucleon pairs connected by the operator, and J is the total angular momentum of the pair, given by $J = |J_i - J_j|, ... |J_i + J_j|$, with the requirement that J is even. There is no need to discriminate between the J of the i, j and k, l pair because $\hat{T}$ can only connect nucleon pairs coupled to the same J. It is customary to write the single-particle energies and two-body matrix elements as[3]

$$\varepsilon_i = \langle i|H|i\rangle, \ \ V_{ijklJ} = \langle ij; J|H|kl; J\rangle. \tag{2.19}$$

The equivalences can be shown exploiting the orthonormality and completeness of the single- and two-particle bases $\{|i\rangle\}$ and $\{|ij; J\rangle\}$. Note that there exist different conventions for normalisation factors on the TBMEs between shell model codes.

2.7.2 Angular momentum coupling

When designing a shell-model code, a choice has to be made on how the angular momentum coupling between the single-particle states is handled. Quantum-mechanical angular momentum algebra dictates that when coupling together

---

[3]The notation emphasises that H is represented in a discrete basis, hence the term matrix element.

two angular momentum eigenstates

$$\hat{J}_1^2|j_1m_1\rangle = j_1(j_1+1)|j_1m_1\rangle, \ \ \hat{J}_2^2|j_2m_2\rangle = j_2(j_2+1)|j_2m_2\rangle \qquad (2.20)$$

to make a total angular momentum state $|jm\rangle$ satisfying

$$\hat{J}^2|jm\rangle = (\hat{J}_1 + \hat{J}_2)^2|jm\rangle = j(j+1)|jm\rangle, \qquad (2.21)$$

the *coupled* eigenstate $|jm\rangle$ is related to the *uncoupled* basis states $|j_1m_1j_2m_2\rangle = |j_1m_1\rangle \otimes |j_2m_2\rangle$ by

$$|jm\rangle = \sum_{m_1=-j_1}^{j_1} \sum_{m_2=-j_2}^{j_2} |j_1m_1j_2m_2\rangle\langle j_1m_1j_2m_2|jm\rangle, \qquad (2.22)$$

where the coefficients $\langle j_1m_1j_2m_2|jm\rangle$ are the Clebsch-Gordan coefficients [44]. The fact that the total angular momentum is not an additive quantum number (because the associated group is non-Abelian) makes it cumbersome to construct many-body states with total J as a good quantum number. An alternative way to construct and represent coupling states of angular momentum is by using the magnetic sub-states m, defined by

$$\hat{J}_z|jm\rangle = m|jm\rangle. \qquad (2.23)$$

The group associated with $\hat{J}_z = \hat{J}_{z,1} + \hat{J}_{z,2}$ coupling *is* Abelian, that is,

$$\hat{J}_z|jm\rangle = (\hat{J}_{z,1} + \hat{J}_{z,2})|jm\rangle = (m_1 + m_2)|jm\rangle. \qquad (2.24)$$

This means that when constructing a many-body Slater determinant from single-particle states having $\hat{J}_{z,i}$ eigenvalues $m_1, m_2, ..., m_N$, the Slater determinant will be an eigenstate of the total $\hat{J}_z = \hat{J}_{z,1} + \cdots + \hat{J}_{z,N}$ with eigenvalue $M = m_1 + \cdots + m_N$. The Slater determinants will *not*, in general, be eigenstates of total angular momentum. However, because the Hamiltonian is rotationally invariant, so that it commutes with both the total and the z-projection angular momentum operators, its eigenstates – linear combinations of the Slater determinants – will also be eigenstates of total angular momentum. The use of $\hat{J}_z$ to construct many-body states of good total M is known as an M scheme. In contrast, the use of many-body states with good total J is known as a J scheme.

2.7.3 KSHELL

For the work presented in this thesis, I have used the shell-model code KSHELL [45], written by Professor Noritaka Shimizu of the Center for Nuclear Study at the University of Tokyo. It uses the M scheme to perform calculations. It is constructed in a way that makes it very efficient and scaleable, enabling calculations in model spaces of up to M-scheme dimension $d = 10^{10}$.

KSHELL represents coordinate x_i in the wave function $\vec{x}$ as a double-precision floating-point number, which takes eight bytes of memory. For a moderately

large model space of $d = 10^8$, then, one wave function vector takes 8×10^8 B $= 0.76$ GB. To solve the eigenvalue problem it is necessary to store hundreds of full wave functions in memory simultaneously. This very quickly exceeds the available memory on most computers. The solution is to use a supercomputer. I have mainly used the Norwegian high-performance computer Fram[4], located at the University of Tromsø. It consists of 1004 computer nodes, each with 32 CPU cores and 64 GB memory [47]. KSHELL utilises a hybrid OpenMP + MPI parallelisation scheme to take maximal advantage of the computing power. OpenMP parallelisation is used to distribute the calculation over the CPU cores within a node. The OpenMP calculations have access to the same memory resources, meaning that the calculations can be closely coupled. In contrast, MPI parallelisation is used to distribute calculations over several compute nodes. The passage of information between compute nodes is much slower than communication within a single node, so it is crucial to distribute the computation in a smart way to limit the need for inter-nodal information exchange. KSHELL exploits symmetry groups in the Hamiltonian, such as spherical symmetry and invariance under parity, to split the calculation into as many disjunct sectors as possible [48]. Disjunct means that different parts of the vectors are not connected by an action of the Hamiltonian, *i.e.*, that the Hamiltonian is block-diagonal. An illustration of this is given in Fig. 2.6, taken from Ref. [48].

Diagonalisation of H to obtain the eigenvectors and eigenvalues involves acting repeatedly with H on vectors in the space (more on this below). When H is block-diagonal, it means that the vectors themselves can be distributed in sectors over the different MPI nodes, with little need for communication between the nodes. KSHELL automatically discovers the optimal distribution of sectors for load balancing. Because of the huge dimension of the space, the matrix elements of H would take up a very large amount of memory. Since memory is a bottleneck in shell-model calculations, KSHELL does not store the matrix elements, but instead generates them on-the-fly in the calculations.

The Hamiltonian, being Hermitian, has as many eigenvalues and eigenstates as its dimension. From a physics viewpoint, only the lowest tens or hundreds of states are of interest. Instead of diagonalising the entire matrix (which would be practically impossible), KSHELL uses the Lanczos algorithm to iteratively obtain the lowest-energy eigenstates [49]. The Lanczos algorithm is based on constructing a subspace, the Krylov space of H, given by

$$\text{span}\left\{ \vec{x}, H\vec{x}, H^2\vec{x}, ..., H^p\vec{x} \right\},\tag{2.25}$$

where $\vec{x}$ is a starting vector, often referred to as the *pivot* vector, that is usually taken as a random vector. By this process, the eigenvectors with the largest (negative) eigenvalues will be filtered out. This can be seen by considering that any vector $\vec{x}_k$ can be written as a linear combination of the eigenvectors $\vec{v}_i$

---

[4]Fram ('Forward') is the name of the polar expedition ship used by Norwegian explorers Fridtjof Nansen, Otto Sverdrup, Oscar Wisting and Roald Amundsen between 1893 and 1912 [46].
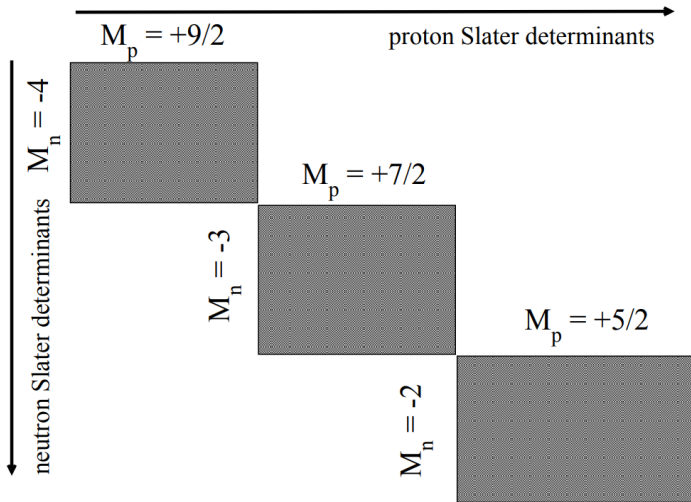
Figure 2.6: Illustration of the block-diagonal form of the Hamiltonian that can be obtained from exploitation of symmetries. The figure is reprinted with permission from Ref. [48].

(because H is Hermitian, so the eigenspace spans the whole Hilbert space):

$$\vec{x}_k = \sum_i c_{i,k} \vec{v}_i \tag{2.26}$$

for suitable coefficients $c_{i,k}$. If $\vec{x}_0$ is acted upon by H to produce $\vec{x}_1$, we see that

$$\vec{x}_1 = H\vec{x}_0 = \sum_i c_{i,0} H\vec{v}_i = \sum_i c_{i,0} E_i \vec{v}_i. \tag{2.27}$$

After p repeated applications of H, the different eigenvector components $\vec{v}_i$ will be weighted by their eigenvalue to the power p,

$$\vec{x}_p = \sum_i E_i^p c_{i,0} \vec{v}_i. \tag{2.28}$$

The eigenvectors with the largest eigenvalues will thus dominate more and more in the vectors $\vec{x}_k$, causing the filtering. KSHELL recursively expands the Krylov subspace until a set convergence criterion is reached, based on a user-defined number of desired eigenstates. However, the required memory for the calculation increases with each additional Krylov expansion. To avoid an arbitrarily large memory need for slowly converging problems, KSHELL uses a modification to the Lanczos algorithm known as the Thick-Restart Lanczos Method [50]. It performs a restart by projecting down into a smaller subspace every time the set maximum number of Lanczos vectors is reached.

In addition to the largest-eigenvalue selection, it is possible to apply even more filtering by running KSHELL in J-projection mode. In this case, the user selects a specific total J for the eigenstates, and only wave function components of that J are filtered out. This is a convenient way to split a calculation involving many states into pieces, and I have used this approach for most of the calculations presented in this thesis. The J projection also solves another problem: Transition strengths in the M scheme with $M = 0$ cannot be calculated between states of the same J, because the Clebsch-Gordan coefficient vanishes. When J-projection mode is used, the wave functions for each J are represented using $M = J$ Slater determinants.

After having obtained the eigenvalues and corresponding eigenvectors, KSHELL allows calculation of transition strengths between the states. Operators for $M1$, $E1$ and $E2$ are implemented, subject to the selection rules described above. It is also possible to calculate Gamow-Teller β-decay strengths by combining calculations for neighbouring nuclei.

A major obstacle for shell-model calculations is the dimension of the wave functions, *i.e.* the size of the basis, which determines (i) whether the calculation can be done at all and (ii) how expensive it will be in terms of CPU time. The dimension of the calculation in a given model space is a function of the number of valence protons and neutrons in the space. In the very simplest case, the valence space consists of a single proton or neutron. Then, the dimension is simply the number of single-particle orbitals that the particle can occupy (and the energy levels are just the single-particle energies). However, as soon as more particles are introduced, the calculation of all possible many-particle configurations becomes a combinatorial problem. Figure 2.7 shows the number of M-scheme basis states in the sd shell as function of proton and neutron number. Notice that the dimension is symmetric between the lower and upper shell closures, and largest in the middle of the shell. This illustrates the mathematical similarities between particles and holes: In the bottom of the shell, there are few valence particles available to make the many-body configurations, and at the top of the shell there are few holes to do the same. It also illustrates why mid-shell nuclei are more difficult to describe microscopically.

2.8   An overview of shell-model interactions

For the work presented in this thesis, I have utilised several different effective interactions. Some are well-known and well-tested, others are custom.

2.8.1   Universal *sd* interaction

Among the most widely-used interactions on the market is the *universal sd interaction* (USD) for the sd shell, using ^{16}O as the inert core. It was originally made by Wildenthal in 1984 [51] by a fit to 380 distinct energy states in the sd shell nuclei. In 2006, Brown and Richter published two revised interactions, called USDA and USDB, which included 608 states in the fit [41]. The
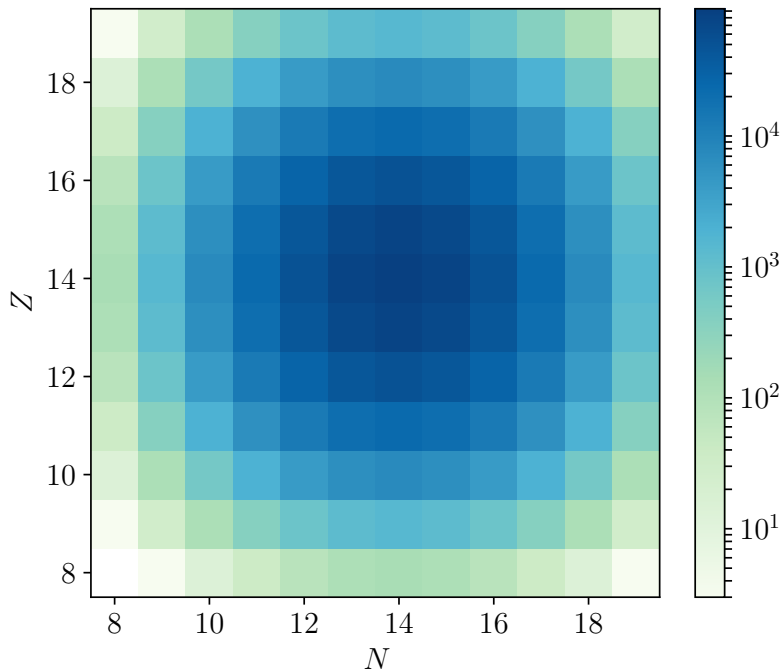
Figure 2.7: The number of M-scheme basis states in the sd shell (^{16}O core) as function of proton and neutron number.

fits are based on a theoretically calculated effective interaction from Ref. [39]. The interactions assume isospin symmetry, *i.e.* equivalence between proton and neutron interactions, and consist of three single-particle energies and 63 two-body matrix elements. The fits do not take into account the full 66 degrees of freedom, but instead consider a subspace spanned by linear combinations of the interaction parameters. The linear combinations are chosen so that they are uncorrelated and explain as much as possible of the data. Thus, it is a form of a principal components regression [52]. The interaction parameters that are not determined from the fit are kept to their theoretical values. For USDA, 30 linear parameter combinations are used, while for USDB the number is increased to 56. The USDA fit has an rms deviation between calculated and experimental energies of 170 keV, while the deviation is decreased to 130 keV with USDB. To borrow terminology from the field of machine learning, they represent two different trade-offs between *bias* and *variance* – USDA having slightly larger bias, while USDB potentially has a larger variance and could be somewhat overfitted [52]. In Paper II [27], I calculated levels and $M1$ transition strengths of all the sd shell nuclei with the USDA interaction.

2.8.2 GXPF

Another standard in the shell model literature is the GXPF1 interaction for the fp shell by Honma $et\ al.$ [42]. It is obtained in the same way as the USD interaction, by starting with a theoretical prediction and varying a subset of linear combinations of the interaction parameters. The fp shell has (assuming isospin symmetry) four single-particle energies and 195 two-body matrix elements. The fit was done by varying 70 linear combinations of the TBMEs, and they obtain an rms deviation of 168 keV between the fitted and experimental levels.[5] The GXPF1 interaction was revised in Ref. [53] to give a better description of new experimental data on neutron-rich fp nuclei. The modified interaction is called GXPF1A, and this is the interaction that I have used for calculations in the fp shell, $e.g.$ for the calculations on ^{59,60}Ni in Paper III [54].

2.8.3 SDPF-MU

For calculations involving more than one major shell, it is infeasible to obtain interaction parameters by a fit to experimental data, as the computational demands to find the eigenstates are very high in most cases. Utsuno $et\ al.$ got around this by combining the existing USD and GXPF1 interactions into the SDPF-MU interaction [55]. However, the existing fits provide no information on the TBMEs for the cross-shell interactions. For this, they use a phenomenological model known as the monopole-based universal interaction, V_{MU}, based on a central mean-field potential plus a tensor component consisting of meson-exchange terms [56]. The interaction is able to explain nuclear deformations and their evolution as function of neutron and proton number. I used SDPF-MU to calculate levels and $E1$ and $M1$ transition strengths of ^{29}Si and ^{44}Sc in Paper II [27], as well as ^{51}Ti in Paper IV.

2.8.4 JUN45

Another much-used interaction is JUN45, which consists of the $f_{5/2}$, p and $g_{9/2}$ orbitals built on a ^{56}Ni core [57]. It is based on fits to 400 experimental energies, concentrated on isotope chains with $Z = 30 - 32$ and isotone chains with $N = 46 - 50$. 45 linear combinations are varied in the fit, and the resulting interaction obtains an rms deviation of 185 keV. The model space is different from the sd and fp shells in that it splits the f and g orbitals, with $f_{7/2}$ and $g_{7/2}$ outside the valence space. This requires a larger $quenching\ factor$ to be applied on the gyromagnetic ratios g_q^s of Eq. (2.11) than for other interactions [57]. The authors show that the best agreement with experimental data is obtained with $g_q^s = 0.7g_q^{s,\mathrm{free}}$, while the recommended value for GXPF is $g_q^s = 0.9g_q^{s,\mathrm{free}}$ [42]. I have used JUN45 extensively in Paper II [27].

---

[5]This number is subject to some uncertainty, because parts of the levels in the fit were calculated with the MCSM and modified by an empirical correction called FDA* [42].
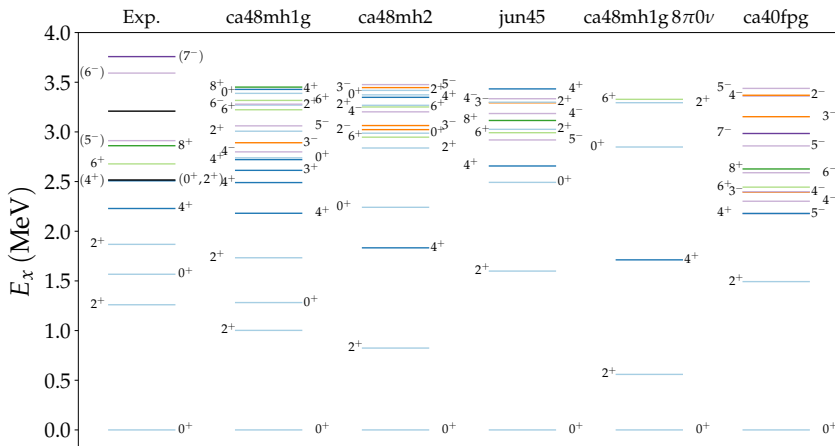
Figure 2.8: The low-energy level scheme of ^{70}Ni compared to shell-model calculations with different interactions. The figure is reprinted with permission from Ref. [59], included in this thesis as Paper I.

2.8.5 CA48MH

As the mass number increases beyond $A \sim 40$, the valley of β stability begins to deviate significantly from the $Z = N$ line. Nuclei with slightly more neutrons than protons are favoured due to the Coulomb repulsion between the latter. For shell-model calculations, it is thus useful to employ closed cores with $N > Z$, such as $^{48}_{20}$Ca. For this core, we have not been able to find any experimentally fitted interactions. Instead, we have used a purely theoretical interaction calculated by Professor Morten Hjorth-Jensen [39]. This interaction is included in the NuShellX@MSU interaction library [58] and called CA48MH1. The library also includes another version of the interaction, called CA48MH2, where the neutron-neutron TBMEs have been replaced with the interaction parameters from Ref. [43], and the proton-proton $f_{7/2}$ TBMEs have been modified.

I have mainly used CA48MH in Paper I [59], where we study ^{70}Ni by shell-model calculations. The ^{56}Ni core is not a reliable choice for calculations of Ni isotopes because the $Z = 28$ shell gap is rather 'soft' – meaning that configurations involving proton excitations from the $f_{7/2}$ orbital play a role in their structure. Because we wanted to calculate many energy levels, we were not able to include the full model space of CA48MH in our calculations due to computational limitations. We applied a truncation where we limited the number of proton excitations from the $f_{7/2}$ orbital to two. We used the CA48MH1 interaction, but increased the single-particle energy of the $g_{9/2}$ orbital significantly, from -1.795 MeV to $+1.7$ MeV. We refer to the resulting interaction as CA48MH1g. The resulting level scheme, compared with experimental data as well as other calculations is shown in Fig. 2.8. With CA48MH1g, we obtained satisfactory agreement with the experimental level structure of ^{70}Ni, including

the excited 0^+ state at around 1.5 MeV and the onset of negative-parity states at ~ 3 MeV. Note how the JUN45 interaction does not reproduce the experimental spectrum well, pushing the excited states to very high energies – likely due to the lack of proton excitations from $f_{7/2}$.

Chapter 3

Statistical nuclear properties

Above a certain excitation energy, it is impractical or even infeasible to resolve individual nuclear states experimentally using spectroscopy, because the level spacings are small compared to the experimental resolution. Exactly where this region starts is a matter of debate, since naturally it varies from experiment to experiment and from nucleus to nucleus, but to talk about statistical nuclear properties the excitation energy should at least be above the pairing gap, which is the energy required to break a pair of nucleons. This region is known as the *quasi-continuum*. It is different from the *continuum* found at even higher E_x, where the level spacing is so small that the resonance widths of the levels actually overlap.[1] Nevertheless, the quasi-continuum is in the realm of *statistical* nuclear properties [61]. Since individual levels and transitions cannot be resolved experimentally, it is instead fruitful to describe the nucleus by averages, using concepts that encompass the gross properties of many states at once. In this chapter I will introduce the *level density*, which describes the number of levels per unit of energy, and the *γ-ray strength function*, which gives the probability of radiative decay between levels. The γ-ray strength function is given an in-depth treatment, as studies of its features, especially at low γ-ray energy, forms the core of this thesis. I put particular emphasis on the *low-energy enhancement* of the strength function, discussing its historical and current experimental and theoretical status. As part of this discussion, I present and discuss my own work on the low-energy enhancement, notably through use of large-scale shell model calculations.

3.1   Level density

It is an experimental fact that nuclei exhibit discrete energy levels. As the excitation energy increases, the energy spacing between adjacent levels tends to decrease. This is a feature common to many quantum systems. For instance, the energy levels of the electron in the hydrogen atom are (under certain ap-

---

[1]Any unstable quantum state has a resonance width, Γ, which is proportional to the probability of decay, and hence inversely proportional to the lifetime of the state. It is a physical width with units of energy, and a measurement of the energy of the state yields values randomly distributed according to $\sim E \pm \Gamma/2$. This can be understood qualitatively by the quantum-mechanical time evolution of an unstable state. A stable (stationary) state $\psi_n(\vec{r})$ has a time evolution given by $\Psi_n(\vec{r}, t) = \psi_n(\vec{r})e^{-iE_n t/\hbar}$, while for an unstable state of decay width Γ it is $\tilde{\Psi}_n = e^{-\Gamma t/\hbar}\psi_n(\vec{r})e^{-iE_n t/\hbar} = e^{-it(E_n - i\Gamma)/\hbar}\psi_n(\vec{r})$. Informally speaking, the unstable state acquires a 'complex energy' $E_n - i\Gamma$. It can be shown that this gives rise to an energy-dependent cross-section for the state of the form $\sigma(E) \propto \frac{\Gamma^2}{(E-E_n)^2+\Gamma^2}$ – the Lorentzian function, a bell-shaped curve of half-width Γ, known as a resonance [60].

proximations) given by [44]

$$E_n = \frac{E_0}{n^2}, \tag{3.1}$$

where $E_0 \approx -13.6$ eV is the ground state energy and $n = 1, 2, 3, \ldots$ labels the levels of increasing energy. Evidently, the spacing between levels decreases rapidly with energy. When the spacing becomes small enough, it becomes meaningful to speak of a *density* of levels per energy. Because the evolution of the level energies in many quantum systems is similar to Eq. (3.1), broadly speaking, the density of levels tends to grow exponentially with energy.

There exist several phenomenological models for nuclear level density. One popular choice is the constant-temperature formula, where the level density is given by [62–64]

$$\rho_{\mathrm{CT}}(E_x) = \frac{1}{T_{\mathrm{CT}}} \exp\left(\frac{E_x - E_0}{T_{\mathrm{CT}}}\right). \tag{3.2}$$

Here, T_{CT} is the nuclear temperature, which is assumed to be constant. In an analogy to classical physics, this can be thought of as the nucleus *melting* with increasing E_x, with the added heat going into breaking nucleon pairs, causing a phase transition – without increasing the temperature of the nucleus [62]. Another much-used model is the Fermi gas model, where the nucleons are modelled as a gas of non-interacting fermions [65]. A popular variety is known as the back-shifted Fermi gas, where the level density is given a translational degree of freedom by a parameter known as the back-shift energy. The back-shifted Fermi gas level density is given by the formula [64, 66]

$$\rho_{\mathrm{BSFG}}(E_x) = \frac{1}{12\sqrt{2}\sigma(E_x)a^{1/4}(E - E_1)^{5/4}} \exp\left(2\sqrt{a(E - E_1)}\right), \tag{3.3}$$

where a is called the level density parameter, E_1 is the back-shift parameter, and $\sigma(E_x)$ is the *spin-cutoff parameter* (see below).

Since many aspects of nuclear dynamics are dependent on the spin and parity of the states involved, it is often necessary to decompose the level density into partial level densities for different spins and parities. The two quantities are simply related by

$$\rho(E_x) = \sum_{J,\pi} \rho(E_x, J, \pi). \tag{3.4}$$

It is somewhat confusing, but customary, to use the same symbol ρ for both types of level density. The γ-ray strength function, which is the topic of the next section, involves the partial level density. A separate quantity to the level density is the *state* density, which is the density found from counting all physically distinct quantum states available – distinguishing even between energy-degenerate quantum numbers such as magnetic sub-states J_z of the same energy level.

For many applications, it is necessary to know the distribution $g(E_x, J)$ of spins J at a given E_x. The spin distribution is defined such that

$$\rho(E_x, J) = g(E_x, J)\rho(E_x). \tag{3.5}$$

Here, $\rho(E_x, J) = \sum_\pi \rho(E_x, J, \pi)$ is the level density for both parities combined. It is usually assumed that, at high enough E_x, the distribution of parities is equilibrated, such that

$$\rho(E_x, J, \pi) \approx \frac{1}{2}\rho(E_x, J). \tag{3.6}$$

It is customary to assume the Ericson spin distribution [62, 66],

$$g(E_x, J) = \exp\left(\frac{-J^2}{2\sigma^2(E_x)}\right) - \exp\left(\frac{-(J+1)^2}{2\sigma^2(E_x)}\right) \tag{3.7}$$

$$\approx \frac{2J+1}{2\sigma^2(E_x)}\exp\left(\frac{-(J+1/2)^2}{2\sigma^2(E_x)}\right), \tag{3.8}$$

where $\sigma(E_x)$ is the spin-cutoff parameter. The distribution is derived for the statistical nuclear regime, and cannot be expected to hold at the lowest excitation energies or for very large values of J. It depends on E_x only through $\sigma(E_x)$. The Ericson distribution is a probability distribution in J, so it is normalised,

$$\sum_J g(E_x, J) = 1. \tag{3.9}$$

Its expectation value is $\langle J \rangle_g \approx \sigma$. Figure 3.1 shows a plot of g for $\sigma = 6$.

Even though the Ericson formula is widely accepted, the resulting distribution is highly dependent on the spin-cutoff parameter σ. There exist many models for σ, such as the rigid-body moment of inertia (RMI) estimate proposed by von Egidy and Bucurescu in 2005 [67, 68], given by

$$\sigma^2(E_x) = 0.0146A^{2/3}\frac{1 + \sqrt{4a(E_x - E_1)}}{2a}, \tag{3.10}$$

where A is the mass number of the nucleus, and a and E_1 are the level density and back-shift parameters of the back-shifted Fermi Gas model, Eq. (3.3). Another spin-cutoff parametrisation, based on the constant-temperature model for level density (Eq.(3.2)), is due to Guttormsen *et al.* [69], and models σ^2 as a linear function in E_x,

$$\sigma^2(E) = \sigma_d^2 + \frac{E - E_d}{S_n - E_d}\left[\sigma^2(S_n) - \sigma_d^2\right]. \tag{3.11}$$

The discrete-spin-cutoff parameter σ_d is determined by fitting to the spin distribution of known discrete levels at $E_x = E_d$, while $\sigma(S_n)$ is estimated using Eq. (3.10) evaluated at $E_x = S_n$.
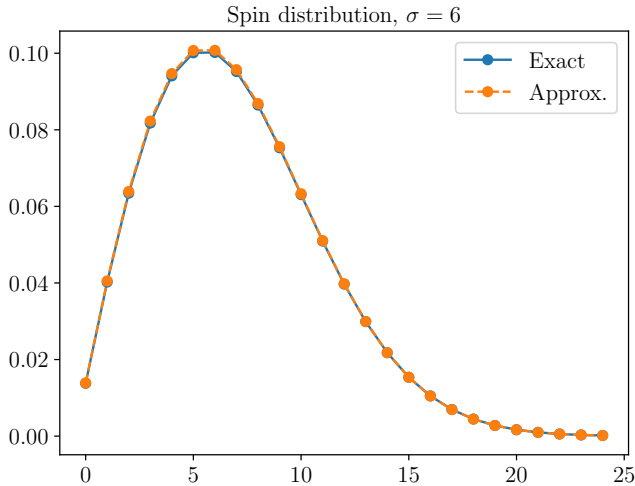
Figure 3.1: Ericson spin distribution for $\sigma = 6$. Shown are both the exact and the approximate formula in Eq. (3.8), demonstrating that the approximation is excellent.

Both the value and the E_x dependence of $\sigma(E_x)$ are important. The experimental Oslo method, which will be discussed in detail in the next chapter, relies on normalisation to auxiliary data, and this normalisation procedure involves the spin distribution. In Paper III in this thesis, the spin distribution was a major source of uncertainty in the analysis, because the nuclei studied, ^{59,60}Ni, are quite light. To model their spin distribution microscopically, I performed large-scale shell-model calculations, calculating up to 300 levels of each spin for each nucleus and fitting Eq. (3.8) for separate bins of E_x to obtain $\sigma(E_x)$. As can be seen in Fig. 3.2 (i), the microscopic calculations give a spin distribution that is excellently described by the Ericson formula. Figure 3.2 (ii) shows the evolution of $\sigma(E_x)$ as function of excitation energy. Shown are also three analytical formulas for $\sigma(E_x)$, namely *(i)* the von Egidy and Bucurescu parametrisation from 2009 [70], labelled 'E&B2009'; *(ii)* their 2005 estimate (Eq. (3.10) [67, 68]), labelled 'RMI'; and the spin-cutoff parametrisation of Guttormsen *et al.* (Eq. (3.11) [69]), labelled 'Recommended'. It is interesting to see that our microscopic calculations closely follow the Guttormsen parametrisation.

It is very difficult to measure spin distributions directly, although they can be inferred from certain types of experiments [71]. Hence, for most applications one must rely on model-based formulas or microscopic calculations such as shell-model calculations or the Hartree-Fock-Bogoliubov combinatorial model of Goriely *et al.* [72].
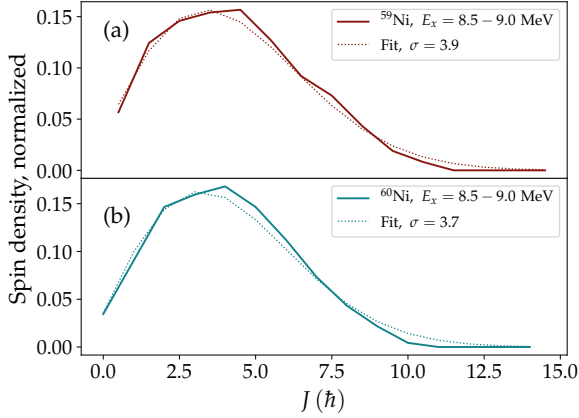
(i)
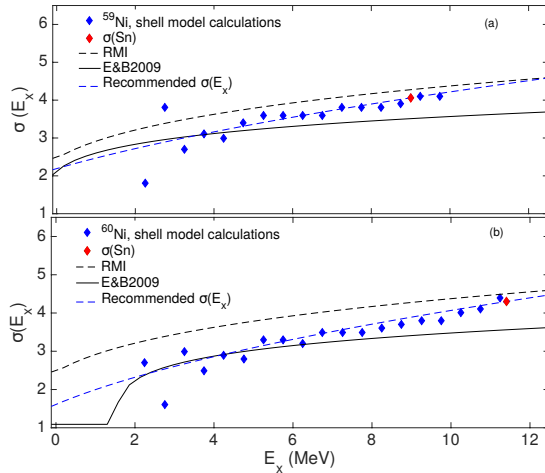
(ii)

Figure 3.2: Calculated spin distributions of ^{59,60}Ni. The top figure (i) shows the distribution of spins for $E_x = 8.5 - 9.0$ MeV together with fits determining $\sigma(E_x)$ using Eq. (3.8), while the bottom figure (ii) shows the fitted $\sigma(E_x)$ as function of excitation energy up to the neutron separation energy, together with different analytical spin-cutoff models. The figures are from Ref. [54], included in this thesis as Paper III.

3.2 The γ-ray strength function

The overarching topic of this thesis is the γ-ray strength function, often shortened as γSF. Other names are used interchangeably, such as radiative strength function or photon strength function. I will sometimes just refer to it as the strength function. It has been the topic of many experimental and theoretical studies, and is an important tool in several branches of nuclear physics. Notably, it finds widespread use in nuclear astrophysics as an ingredient in models of heavy-element nucleosynthesis networks, which is the study of how heavy elements are formed in the Universe [3]. The strength function is defined separately for each multipolarity XL of γ radiation as [73]

$$f_{XL}(E_\gamma, E_i, J_i, \pi_i) = \frac{\langle \Gamma_\gamma^{XL} \rangle (E_\gamma, E_i, J_i, \pi_i)}{E_\gamma^{2L+1}} \rho(E_i, J_i, \pi_i) \tag{3.12}$$

$$= \frac{16\pi}{9\hbar^3 c^3} \langle B(XL) \rangle (E_\gamma, E_i, J_i, \pi_i) \rho(E_i, J_i, \pi_i). \tag{3.13}$$

Here Γ_γ^{XL} denotes the partial decay width of a level at excitation energy E_i, carrying spin J_i and parity π_i, decaying with a γ ray of energy E_γ and multipolarity XL, and $B(XL)$ is the corresponding reduced transition strength as defined in Eq. (2.10).[2] The quantity $\langle \Gamma_\gamma^{XL} \rangle (E_\gamma, E_i, J_i, \pi_i)$ $(\langle B(XL) \rangle (E_\gamma, E_i, J_i, \pi_i))$ denotes the *average* Γ_γ^{XL} $(B(XL))$ value in the vicinity of the initial excitation energy E_i, for decays with γ-ray energies in the vicinity of E_γ. In practice, the vicinity is defined by some energy binning, typically 200 keV. For most of what follows, L will be 1, *i.e.* considering only dipole radiation, since it dominates at the relevant E_x. In Appendix A, I give a detailed derivation of the γ-ray strength function in terms of the underlying fundamental quantities.

The γ-ray strength function is an average quantity that describes the probability for a nucleus to emit γ radiation of a certain energy E_γ. By turning Eq. (3.12) around,

$$\langle \Gamma_\gamma^{XL} \rangle (E_\gamma, E_i, J_i, \pi_i) = \frac{E_\gamma^{2L+1} f_{XL}(E_\gamma, E_i, J_i, \pi_i)}{\rho(E_i, J_i, \pi_i)}, \tag{3.14}$$

we see how f can be thought of as an ingredient in a *probability model* for the nucleus, providing the mean value of the probability distribution of partial decay widths Γ_γ at the given E_i, J_i and π_i,

$$\Gamma_\gamma = \epsilon \langle \Gamma_\gamma \rangle, \tag{3.15}$$

where ϵ is the relative variation between individual partial decay widths. This variation is usually assumed to be given by the Porter-Thomas distribution [74]. The Porter-Thomas model says that the individual partial decay widths,

---

[2]The partial decay width Γ_γ must not be confused with the *total* decay width of a level, $\Gamma_{\gamma,\text{tot}} = \sum_{E_\gamma} \Gamma_\gamma$.

normalised to the average partial width, has a χ^2 distribution with one degree of freedom,

$$\frac{\Gamma_\gamma}{\langle \Gamma_\gamma \rangle} \sim \chi^2_{\nu=1}. \tag{3.16}$$

It arises naturally in a model where the wave functions of individual states are completely chaotic, as if governed by a Gaussian orthogonal ensemble (GOE) [61]. In statistical decay simulation codes such as RAINIER [75], an input γ-ray strength function and level density are combined with random draws from the Porter-Thomas distribution (as well as a model for the level spacing distribution, *e.g.* the Wigner distribution [76]) to generate an artificial level scheme and decay widths of the levels.

It is interesting to investigate whether Porter-Thomas fluctuations can be found within configuration-interaction shell-model calculations – *i.e.*, whether the configuration-interaction shell model includes enough complexity to approach the behaviour of a GOE. Figure 3.3 shows the distribution of

$$y = \frac{B(M1)}{\langle B(M1) \rangle} \tag{3.17}$$

for ^{60}Ni calculated with the GXPF1A interaction for Paper III [54]. Figure 3.3a shows the distribution of y values for three selected individual initial levels with $E_i = 7.29$, 9.24 and 12.81 MeV, including 580, 1284 and 340 individual $B(M1)$ values, respectively. The average $\langle B(M1) \rangle$ is calculated separately for each E_i. Also shown is a χ^2 distribution with one degree of freedom, $\nu = 1$, *i.e.*, the Porter-Thomas distribution. The y distributions do appear to fluctuate around the Porter-Thomas distribution. In Fig. 3.3b, I have plotted the distribution of y values for different *ranges* of initial excitation energies. Each range consists of 50 initial levels, having a mixture of all available spins, and for each level I have calculated the relative $B(M1)$ values by normalising to the average $B(M1)$ for transitions from that level. The resulting distributions include all normalised $y = B(M1)/\langle B(M1) \rangle$ transitions from all 50 levels. With the increased statistics, it is clear that the distributions closely match the Porter-Thomas distribution. In Fig. 3.3c, I have plotted the relative error, *i.e.*, each y distribution divided by the $\chi^2_{\nu=1}$ curve. The relative error is close to 1 for low y values. It increases with increasing y, as should be expected since the number of transitions, as well as the $\chi^2_{\nu=1}$ value, becomes very small. These results are consistent with other studies [77, 78].

3.3 The generalised Brink–Axel hypothesis

The strength function as it stands in Eq. (3.12) depends on four quantities: The γ-ray energy of the transition, and the excitation energy, spin and parity of the initial state. Furthermore, we should separate between *upward* and *downward* strength functions, $f_\uparrow$ and $f_\downarrow$, describing photo-absorption and decay,
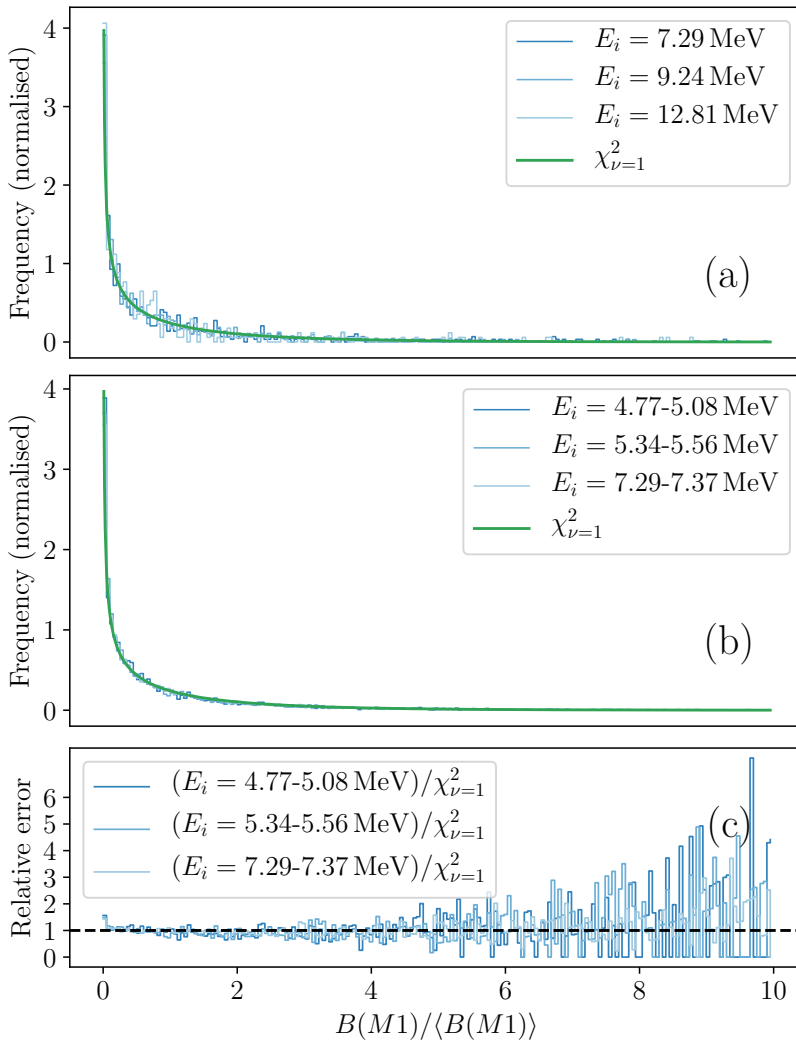
Figure 3.3: Distribution of $B(M1)/\langle B(M1)\rangle$ values from a shell-model calculation of ^{60}Ni, compared to the Porter-Thomas distribution, $\chi^2_{\nu=1}$. The calculation was done for Paper III, using the GXPF1A interaction, and contains only positive-parity levels. Panel (a) shows the distribution for selected specific initial levels, while panel (b) shows the distribution for an ensemble of initial levels. Panel (c) shows the relative difference between the distributions in (b) and the $\chi^2_{\nu=1}$ distribution. See the text for details.

respectively. It is however customary to assume that the strength function is approximately independent of excitation energy, spin, parity and direction, *i.e.*,

$$f_{\uparrow/\downarrow}(E_\gamma, E_i, J_i, \pi_i) \approx f(E_\gamma). \tag{3.18}$$

This assumption, a requirement of the Oslo method as well as in many applications, is known as the generalised Brink–Axel hypothesis. A topic of much debate over the last decades, as well as numerous experimental and theoretical studies, the Brink–Axel hypothesis continues to be a contentious issue. The hypothesis was originally formulated by David Brink in his doctoral thesis [79]. It was posed there in the context of $E1$ excitations on the ground state of even-even nuclei, and states that the cross-section to excite the nucleus is independent of whether the excitation happens from the ground state or from an excited state, or in Brink's own words [79],

> ... if it were possible to perform the photoeffect on an excited state, the cross section for absorption would have the same energy dependence as for the ground state.

Isolated, the Brink hypothesis is an assumption of E_x independence of the upwards $E1$ strength function. However, by invoking the principle of detailed balance [22], Brink applied the hypothesis to the calculation of neutron-resonance decay widths [79], thereby connecting the upward and downward strength functions. Peter Axel in 1962 published an article where he pointed to the usefulness of Brink's idea, which had so far not been widely applied [80]. The hypothesis has subsequently been generalised by others to assume independence also from spin and parity, and that the independence holds not only for $E1$ but for the dipole strength function in general [81–85].

In the Oslo method, the generalised Brink–Axel (gBA) hypothesis is implicit since the method relies on a global fit of f to decay spectra from a large range of excitation energies, the spectra being a mix of spins and parities. A study was done where the spectra of ^{238}Np were split into different regions of E_x, and the Oslo method was used to extract the strength function separately for different initial and final excitation energies [85]. They found the gBA hypothesis to be upheld as a function of excitation energy. Similar results have been found also for other nuclei [86, 87].

When the γ-ray strength function is studied by means of photo-excitations on the ground state, the low-energy part of the strength function cannot be resolved because there are no γ-ray transitions with energy smaller than the excitation energy of the first excited state. Also, where the strength function can be resolved at low E_γ, it is based on few states and subject to the low-energy structure of the nucleus as well as Porter-Thomas fluctuations. In contrast, studies of the downward strength function based on decays between highly excited states allow extraction of the strength function down to near $E_\gamma = 0$. The latter type of experiments have revealed a non-zero value of the strength function in the limit of vanishing E_γ (which will be discussed in detail in Section 3.4 below). It can be argued that this apparent difference between the upwards and

downwards strength functions constitutes a violation of the gBA hypothesis. On the other hand, one could argue that the absence of states renders the strength function unavailable, and that there simply is no low-energy upwards strength function built on the ground state.

3.3.1 Strength functions from shell-model calculations

A full-configuration shell-model calculation provides detailed information about single nuclear levels and their decay probabilities. Even though the detailed structure of states at high E_x are unlikely to be correctly represented by calculations, due to their sensitivity to model space and interaction parameter details, the *average* properties of the calculated states can still provide valuable insight. For the purpose of statistical nuclear properties, it is desirable to turn these detailed predictions into level densities and γ-ray strength functions.

From a set of nuclear levels characterised by excitation energy, spin and parity, $\{(E_x', J', \pi')_i\}_{i=1}^N$, the level density can be extracted by choosing an energy bin size ΔE and counting how many levels there are in each bin, *i.e.*, a histogram, and dividing by the bin size:

$$\rho(E_x, J, \pi) = \frac{(\text{number of levels with } E_x' \in E_x \pm \Delta E/2, J' = J \text{ and } \pi' = \pi)}{\Delta E}.$$
(3.19)

Figure 3.4 shows the positive-parity level density of ^{60}Ni calculated within the shell model. In the upper panel I have plotted the partial level density for each spin, $\rho(E_x, J, \pi = +)$, and in the lower panel they are summed together. The calculation includes up to 300 levels of each spin and illustrates how the spin distribution affects the density of levels. For the most frequently occurring spins, $J \sim 3 - 4$, the 300 levels are used up much more rapidly, reaching an excitation energy of only ~ 9 MeV for the highest-energy level, while the highest-spin levels are all covered up to 15 MeV. The calculated total level density is thus only complete up to 9 MeV.

Extracting the γ-ray strength function is a little more involved. The starting point is Eq. (3.13), which reveals that the necessary ingredients are the level density at the initial excitation energy, $\rho(E_i, J_i, \pi_i)$, and the average reduced transition strength $\langle B(E_\gamma, E_i, J_i, \pi_i) \rangle$. The latter involves not only the initial energy E_i, but also the final energy $E_f = E_i - E_\gamma$. The average is taken within energy bins ΔE of both E_i and E_f. This gives the strength function $f_{XL}(E_\gamma, E_x, J, \pi)$.

We typically want to compare calculated strength functions with experimental ones, extracted by *e.g.* the Oslo method. The experiments usually invoke the gBA hypothesis and present a strength function that only depends on E_γ. The simplest way to remove the dependence on the gBA-invariant parameters is to average over them, *i.e.*,

$$f_{XL}(E_\gamma) \equiv \frac{1}{N_{E_i} N_{J_i} N_{\pi_i}} \sum_{E_i, J_i, \pi_i} f_{XL}(E_\gamma, E_i, J_i, \pi_i).$$
(3.20)
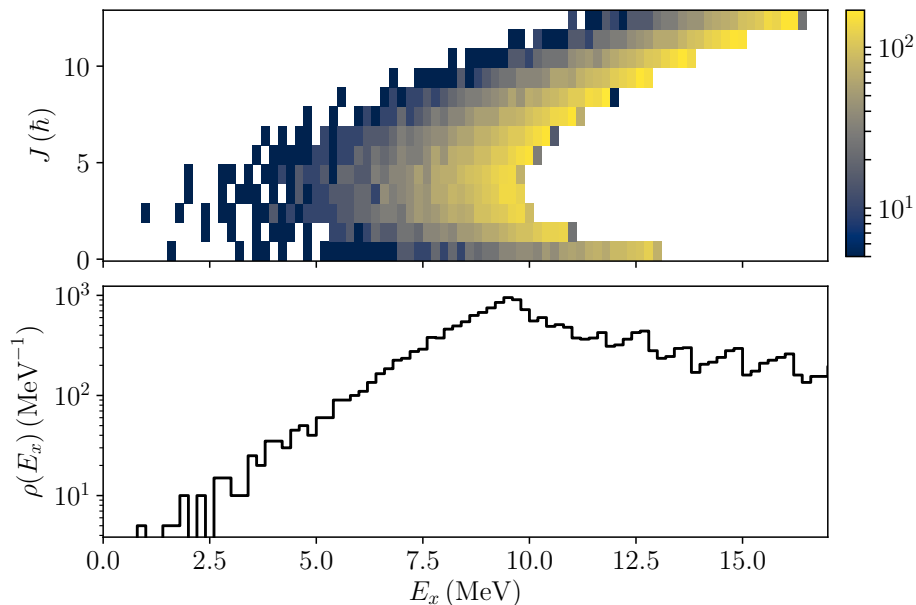
Figure 3.4: Extracted level density per spin (upper panel) and summed over all spins (lower panel) for ^{60}Ni, calculated in the shell model. The calculation was done for Paper III, using the GXPF1A interaction, and includes up to 300 levels of each spin. Only positive-parity states are included.

The average is taken only over bins where f is non-zero, *i.e.*, that contain at least one transition. Figure 3.5 shows calculated $M1$ strength functions for ^{60}Ni. The upper panels show the 'raw' strength function $f_{M1}(E_\gamma, E_i, J_i, \pi_i)$ for two different spins. Above a certain E_x threshold, the strength functions vary very little between E_x bins, in agreement with the gBA hypothesis. The lower panel shows strength functions averaged over E_x for different spins. The curves are practically identical except for small variations that can be attributed to Porter-Thomas fluctuations between the individual transition strengths that went into the strength functions, again confirming the gBA hypothesis. The shape of the strength functions will be discussed next.

3.3.2 Resonances in the strength function

The overall shape of the γ-ray strength function is similar for most nuclei. It is dominated by the $E1$ *giant dipole resonance* (GDR), which is a large peak structure, or *resonance*, with maximum at around 15-20 MeV depending on the nucleus [88]. The GDR can be understood as a collective mode of excitation where the protons and neutrons oscillate against each other [89]. There exist a
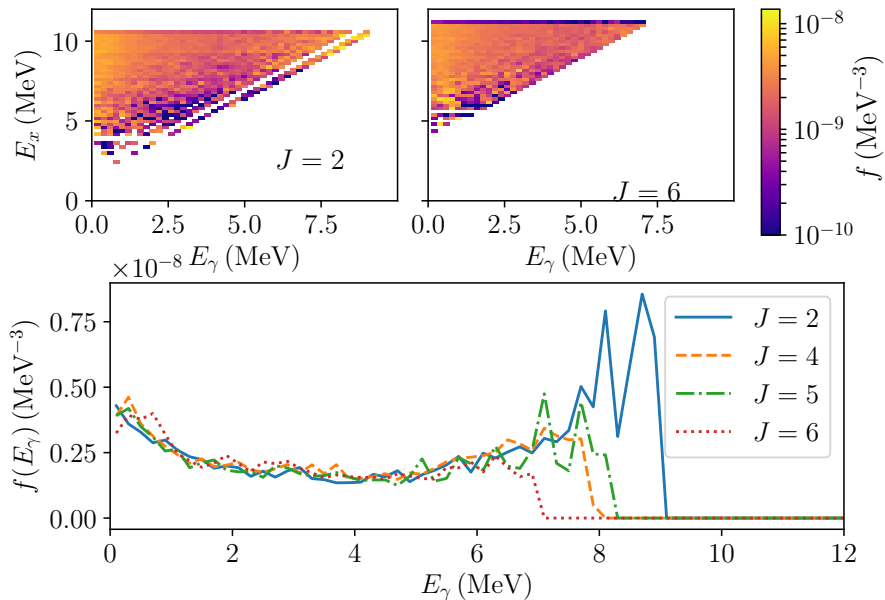
Figure 3.5: Calculated $M1$ γ-ray strength functions for ^{60}Ni. The upper panels show $f_{M1}(E_\gamma, E_i, J_i, \pi_i)$ for two select spins, while the lower panel shows averages taken over E_x for different spins. The calculation was done for Paper III, using the GXPF1A interaction, and includes up to 300 levels of each spin. Only positive-parity states are included.

number of models to describe the GDR, the simplest of which is the standard Lorentzian (SLO) as suggested by Brink [79] and reiterated by Axel [80],

$$f_{E1,\text{SLO}}(E_\gamma) = \frac{1}{3\pi^2\hbar^2c^2}\sigma_r\Gamma_r\frac{E_\gamma\Gamma_r}{(E_\gamma^2 - E_r^2)^2 + E_\gamma^2\Gamma_r^2}, \qquad (3.21)$$

where σ_r and E_r are the peak cross section and the centroid energy, respectively, of the resonance [79, 90]. Although the dipole strength function is dominated by the GDR, it also exhibits other features for many nuclei. The so-called $E1$ pygmy dipole resonance is found at γ-ray energies near neutron threshold in some nuclei near closed shells (Ref. [91] and references therein). The $M1$ strength function also has a *giant magnetic dipole resonance* (GMDR), which is interpreted in the shell model as originating from spin-flip transitions between orbital pairs of $j = l\pm 1/2$ [92].[3] Some nuclei also have an $M1$ *scissors resonance* at $E_\gamma \sim 3$ MeV [82, 92, 93]. It can be interpreted as a scissors-like motion of

---

[3]In the lower panel of Fig. 3.5, it is probably the GMDR that appears in the blue curve at the highest γ-ray energies.

protons against neutrons, hence the name, and it is correlated with nuclear deformation.

3.4 The low-energy enhancement

In 2004, Voinov, Algin *et al.* published an Oslo-method experiment on ^{56,57}Fe that contained a novel and controversial finding: Contrary to all theoretical models available at the time, the γ-ray strength function was found to increase, rather than decrease, as E_γ approached zero [94]. Figure 3.6 shows the measured strength functions in the original publication. This became the topic of much debate in the years to come, concerning whether this was an experimental fluke, an error in the Oslo method, or in fact a physical truth. Notably, Krtička *et al.* investigated the low-energy strength function of ^{96}Mo by two-step cascade spectra using a ^{95}Mo$(n,\gamma\gamma)^{96}$Mo reaction, and did not find evidence of the low-energy enhancement [95]. All the while, more and more Oslo analyses kept showing the same low-energy enhancement for other nuclei, including $^{93-98}$Mo. The matter was largely settled in 2012, when Wiedeking *et al.* confirmed its existence in ^{95}Mo using a different experimental technique [96]. A measurement using that same technique was recently performed on ^{56}Fe, again confirming Oslo-method measurements [97]. Over the years, it has been referred to by various names, such as *soft pole* [98], *low-energy enhancement (LEE)* [27], *up-bend* [99], *zero limit* [100] and *low-energy magnetic radiation (LEMAR)* [101]. It was shown by Larsen *et al.* in 2013, via measurements of angular distributions for the case of ^{56}Fe, that the enhancement is of dipole type [102], but its electromagnetic character ($E1$ or $M1$) has remained elusive.

The status of the low-energy enhancement is summarised in Fig. 3.7, which shows all nuclei that have been measured and analysed with the Oslo method so far. For each nucleus, we have considered whether the γ-ray strength function in the original publication shows a low-energy enhancement or not. Yellow stars are cases where there is a clear enhancement, red circles are cases without any visible enhancement, and blue diamonds are cases that are unclear.

In parallel with the experiments, a large amount of theoretical work has been done to interpret the LEE. Litvinova and Belov were able to explain the LEE observed in ^{94,96,98}Mo, as well as the absence of any LEE in the measurements of ^{116,122}Sn, by a finite-temperature version of quasiparticle random phase approximation (QRPA) theory [135]. In their model, it is the $E1$ strength function that changes its low-energy behaviour at non-zero nuclear temperature, causing a low-energy enhancement, as shown in Fig. 3.8a. Their model predicts that the low-energy enhancement drops to zero as $E_\gamma \to 0$. The cyan band in Fig. 3.8a represents the spread between different nuclear temperatures, and while the band encapsulates the experimental measurement, their model does not reproduce the rapid onset of the LEE below $E_\gamma = 2$ MeV with a single temperature value.

Simultaneously, in 2013, Schwengner, Frauendorf and Larsen published an article where they studied the LEE within the configuration-interaction shell
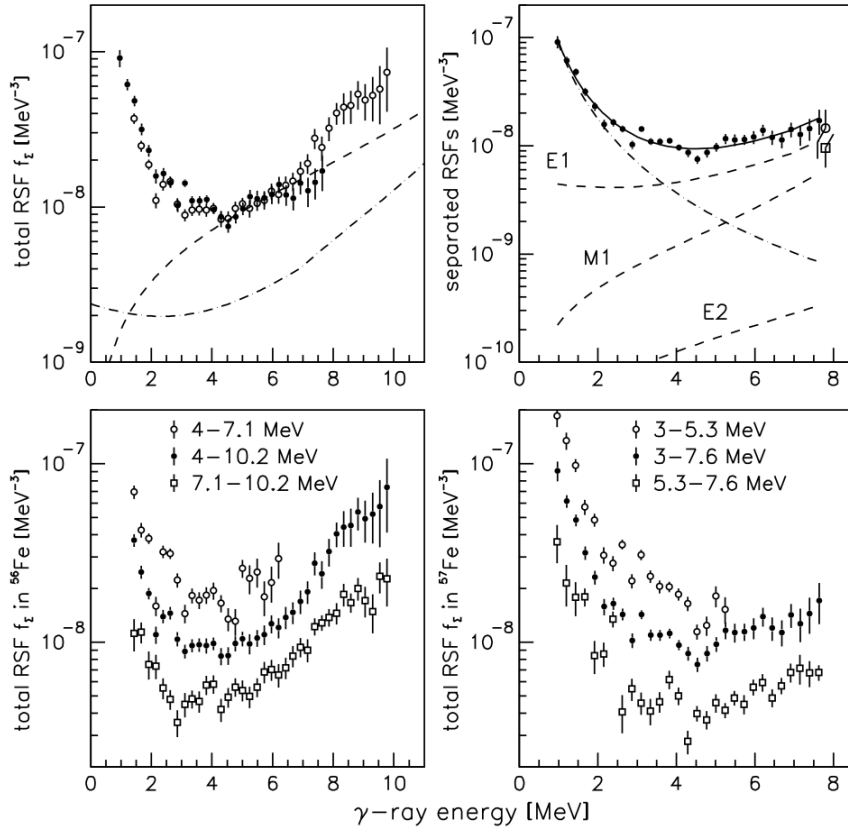
Figure 3.6: The first measurement of the low-energy enhancement of the γ-ray strength function, in ^{56,57}Fe. The panels show, in clockwise order from the top left: (*i*) the extracted strength functions for ^{56,57}Fe (open and solid circles, respectively); (*ii*) a fit of the ^{57}Fe strength function and a decomposition into models for $E1$, $M1$ and $E2$ components plus the unknown low-energy enhancement; (*iii*) the ^{57}Fe strength function extracted for different excitation-energy regions, with the upper and lower curves offset by a factor to allow visual separation; and (*iv*) the same as (*iii*) but for ^{56}Fe. The figure is reprinted with permission from Ref. [94].
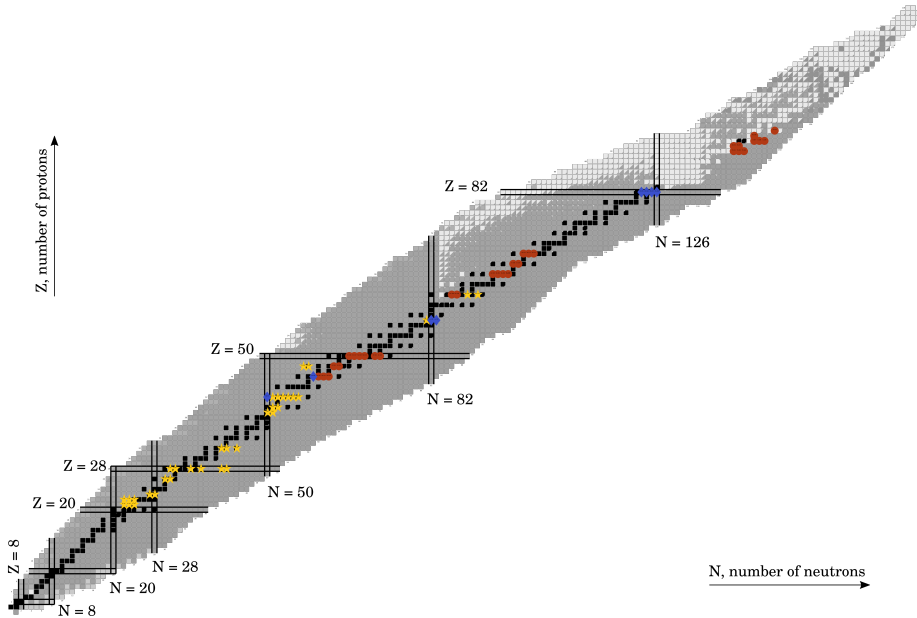
Figure 3.7: A chart of nuclides indicating all nuclei that have been studied with the Oslo method. Yellow stars are cases where the low-energy enhancement has been seen, red circles are cases where no low-energy enhancement was seen, and blue diamonds are cases that are unclear with respect to the enhancement. The publications of Oslo-method analyses that form the basis for the figure are found in Refs. [54, 59, 69, 87, 94, 96, 98, 99, 102–134]. The figure is reprinted with permission from Ref. [27], included in this thesis as Paper II.

model [136]. They also considered Mo isotopes, and were able to explain the LEE as strong $M1$ transitions between closely-spaced energy levels. Their result for ^{96}Mo is shown in Fig. 3.8b. While the two explanations are seemingly at odds, the picture may not be so black and white. While working on Paper II in this thesis, we discovered that the way the γ-ray strength function was extracted in Ref. [136] leads to an overestimation of the absolute strength[4]. In principle, it is thus possible that both the $E1$ and $M1$ mechanisms are needed to explain the LEE.

Subsequently, more work has been done on the low-energy enhancement within the framework of the shell model. Brown and Larsen studied ^{56,57}Fe, and were again able to explain the LEE as an $M1$ feature [137].[5] They looked

[4]The problem has to do with the level density. The definition of the strength function includes the *partial* level density for a given spin and parity, but in some cases, the total density of several spins has been used instead. See the Appendix of Ref. [27] for more details.

[5]However, also in this work there is an issue with the absolute value of the calculated $M1$ strength function, so the agreement could be less good than it appears from the paper. In fact, the $M1$ strength presented is unreasonably high, as the addition of an $E1$ component
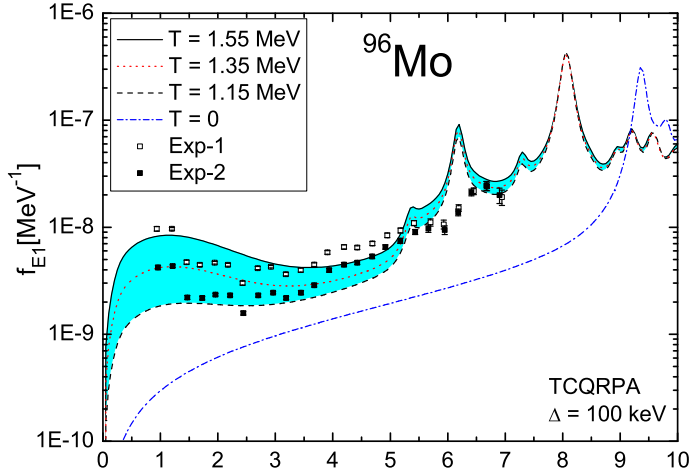
(a)
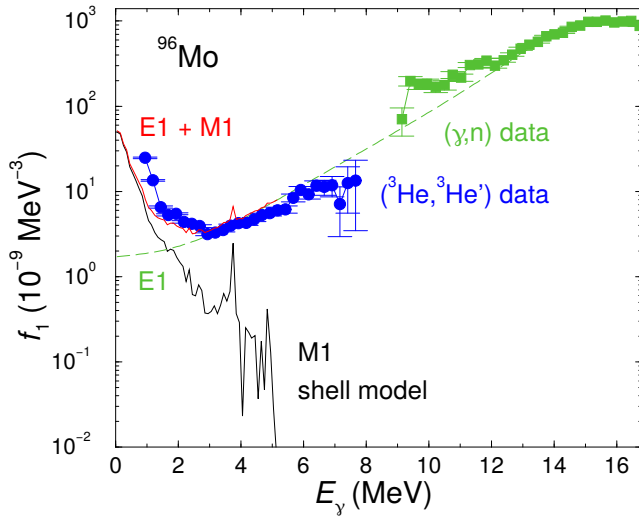
(b)

Figure 3.8: The thermally unblocked QRPA $E1$ γSF model (a) and a shell-model calculation of the $M1$ γSF (b) of ^{96}Mo, compared to data from Ref. [98]. The open and closed squares represents two different absolute normalisations of the same measurement. The figures are reprinted with permission from Refs. [135] and [136], respectively.

at the contribution to the strength function from transition components between different shell-model orbitals, and found that transitions within high-l orbitals are driving the enhancement. Karampagia *et al.* studied the strength function of ^{49,50}Cr and ^{48}V using a toy model where only the $f_{7/2}$ orbital was included [138]. They found that the slope of the LEE depended on the coupling strength of the $T = 1$ matrix elements of the two-body interaction.[6] In 2017, Schwengner, Frauendorf and Brown published another shell-model study where they calculated the $M1$ γ-ray strength functions of ^{60,64,68}Fe [101]. They found evidence for a bi-modality in the low-energy strength, where the low-energy enhancement is diminished as the neutron number increases towards the middle of the $fpg_{9/2}$ shell, while a scissors resonance simultaneously grows in. They predict that the two phenomena are coupled together and may be related to nuclear deformation. Sieja presented the first shell-model calculation of a γ-ray strength function, for ^{44}Sc, that included both $M1$ and $E1$ strength in the same framework [139]. She found a large $M1$ enhancement and a flat behaviour of the $E1$ strength at low γ-ray energy.

A question of profound importance for r-process nucleosynthesis research is whether or not the LEE persists for nuclei approaching the neutron drip line. It has been shown by Larsen and Goriely that the low-energy enhancement influences (n, γ) capture cross sections calculated with Hauser-Feschbach theory – and that it influences neutron-rich nuclei the most [140]. This is because the neutron separation energy gets lower close to the neutron drip line, increasing the importance of low-energy γ-ray transitions as modes of de-excitation of the compound nucleus after neutron capture. In Ref. [59], included as Paper I in this thesis, we present a measurement of the level density and strength function of the neutron-rich nucleus ^{70}Ni using the β-Oslo method. At the time of publication, it was the most neutron-rich nucleus that has been found to have an LEE.[7] We were able to perform shell-model calculations to extract a level density and $M1$ γ-ray strength function for ^{70}Ni, and show that the shell model indeed agrees that there should be a low-energy enhancement also for this neutron-rich nucleus. We also found that the enhancement is robust against the particulars of the chosen model space, orbital truncation and interaction parameters – whether we used a ^{48}Ca or a ^{56}Ni core, the slope of the enhancement is quite similar. We even investigated the consequence of the β-decay-selective spin population in the β-Oslo experiment (see the next chapter), and found that the γ-ray strength function is largely insensitive to spin selections. This is a theoretical validation of the generalised Brink–Axel hypothesis for $M1$ radiation as function of spin and parity.

In Paper I, we also performed a scan over the isotopes of nickel, calculating $M1$ strength functions for $^{56-70,72,74,76}$Ni, and found an LEE for *all* isotopes. This naturally begs the question: How does it look for other elements? In Ref. [27], included in this thesis as Paper II, we answer this question with

---

would overshoot the data points.

[6]The notation $T = 1$ refers to isospin formalism, where the protons and neutrons are represented as the up and down states of a two-component *isospin doublet* [24].

[7]It was recently superseded by ^{74}Zn [141].

a systematic study across 283 different nuclei. We considered nuclei in two different mass regions, the *sd* shell atop an ^{16}O core and the $f_{5/2}pg_{9/2}$ shell atop a ^{56}Ni core. The large span in mass, combined with the fine-grained resolution obtained by considering all neighbouring nuclei within one mass region, allowed us to reach novel insights. We defined the 'amount' of low-energy enhancement by the quantity

$$u(f_{M1}) = \frac{\int_0^{2\,\text{MeV}} f_{M1}(E_\gamma)\,\mathrm{d}E_\gamma}{\int_{2\,\text{MeV}}^{6\,\text{MeV}} f_{M1}(E_\gamma)\,\mathrm{d}E_\gamma}. \qquad (3.22)$$

In effect, u measures the steepness of the LEE. A very steep LEE has a large u value, while a completely flat one has $u = 1/2$. In Fig. 3.9c is the result in the form of a nuclear chart. The plot reveals several interesting trends. In each mass region, the u value takes the form of a 'bowl', meaning that it is larger near proton and neutron shell closures. This reaffirms the findings in Ref. [101] that the LEE is diminished in mid-shell, but we also see how it increases again as we approach the $N = 50$ shell closure, and even grows *steeper* across the shell. The same effect is seen, albeit less pronounced, in the *sd* shell. We interpret this with Ref. [136] as a *shears bands*-like effect. Nuclei that have proton excess and neutron deficiency relative to a doubly magic core, such as the lower-right parts of the *sd* and $f_{5/2}pg_{9/2}$ shells, has a tendency to produce strong $M1$ transitions due to rotations of a large, transverse magnetic moment. The apparent tendency for the LEE to vary as function of proximity to shell closures has led others to suggest deformation-dependent phenomenological parametrisations of the low-energy $M1$ strength function [142, 143].

Returning to Fig. 3.9, u is generally larger in the *fpg* than in the *sd* shell. We interpret this as an indication that the LEE steepens with mass number, which is consistent with the fact that few LEE cases have been seen experimentally above $A = 100$ (more on this in Section 3.4.1 below). The mass dependence can be explained by considering that the mass of a nucleus is proportional to the average l of the orbitals available around the Fermi surface – compare Fig. 2.4. Hence it is consistent with the findings in Ref. [137] that the LEE is driven by high-l orbitals. Finally, we note that the lowest u value in Fig. 3.9 is $\sim 1/2$, corresponding to a flat low-energy $M1$ strength. This is in itself important, because most phenomenological models of γ-ray strength functions used in *e.g.* nucleosynthesis network calculations assume that the strength function drops as $E_\gamma \to 0$ [90]. Simultaneously with the publication of Paper II, another shell model study was published by Sieja, considering $A > 100$ nuclei [144]. She finds strikingly similar results. Figure 3.10 shows her calculations for $Z = 52$ isotopes and $N = 80$ isotones. They all have an LEE, and its steepness increases with proximity to the shell closure as function of both Z and N. She also calculates the strength of a deformed, proton-rich nucleus, ^{108}Xe. There, she finds no LEE, but a flat strength function, just as we did for mid-shell nuclei in our calculations.

We also applied the shell model to investigate whether the LEE is of magnetic or electric character. As discussed in the previous chapter, $E1$ calculations
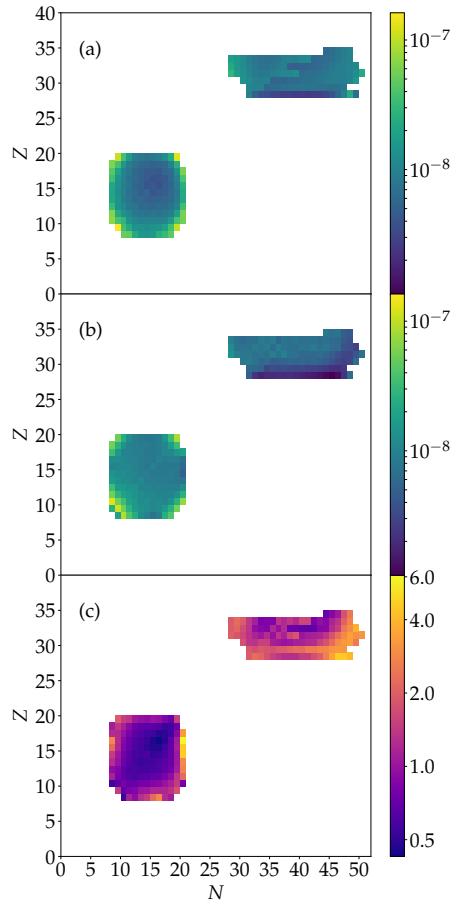
Figure 3.9: A chart of nuclides showing integrated γ-ray strengths for each nucleus. Panel (a) gives the integrated strength from 0 to 2 MeV, panel (b) from 2 to 6 MeV, and panel (c) takes the ratio of the two. See text for details. The figure is reprinted with permission from Ref. [27], included in this thesis as Paper II.
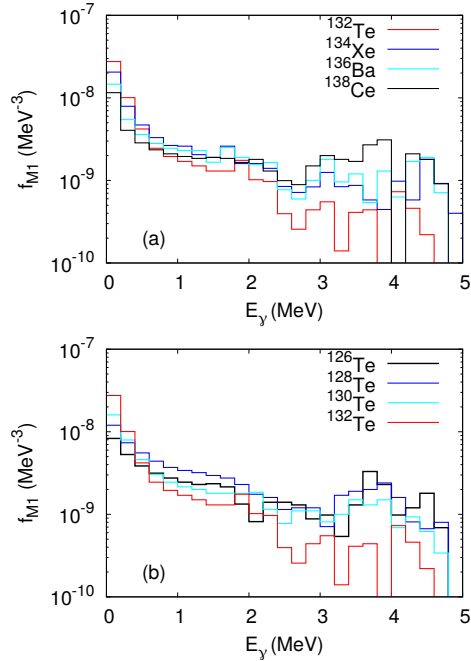
Figure 3.10: $M1$ strength functions calculated for nuclei close to the ^{132}Sn shell closure. The $N = 80$ isotones (upper panel) and $Z = 52$ isotopes (lower panel) exhibit systematic consistent with our findings in other mass regions. The figure is reprinted with permission from Ref. [144].

require large model spaces to allow cross-shell excitations, and this limits the scope of such studies. An ideal case was the neutron-rich nucleus ^{51}Ti, which has been measured using the Oslo and β-Oslo methods (Paper IV in this thesis). Using the SDPF-MU interaction in a $1\hbar\omega$ truncation scheme, we calculated both $M1$ and $E1$ strength functions based on transitions between hundreds of levels of many spins and both parities. Figure 3.11 shows the measurement and the calculation. The agreement is excellent, and the calculated LEE is clearly dominated completely by the $M1$ component, while the $E1$ component trails off as $E_\gamma \to 0$. The same behaviour was found in Paper II, where we also calculated total dipole strengths for two nuclei, ^{28}Si and ^{44}Sc. The low-energy part of the strength function is dominated by the $M1$ component, even in the case of ^{28}Si, where the $M1$ strength is approximately flat. Jones et $al.$ recently performed an experiment with the aim of settling the $E1/M1$ question for the case of ^{56}Fe, but the result was inconclusive due to insufficient statistics, although they find a slight preference for $M1$ [97].
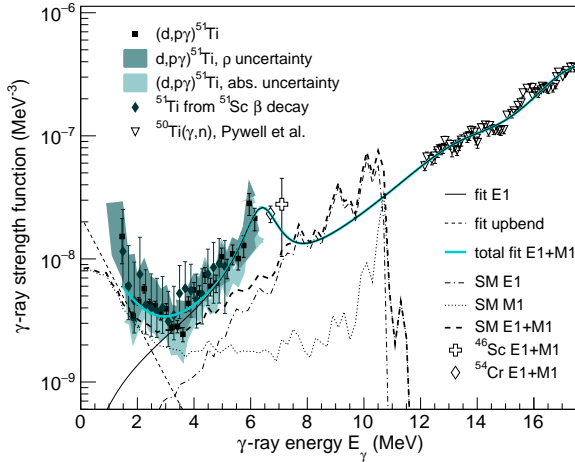
Figure 3.11: ^{51}Ti γ-ray strength function measured with the β-Oslo method and compared to theoretical calculations. The figure is from Paper IV in this thesis.

3.4.1 Is the low-energy enhancement present everywhere?

The Oslo method has technical difficulties that prevent extraction of the strength function below a certain E_γ threshold. With the old detector system at the Oslo Cyclotron Laboratory, CACTUS, this threshold is usually around $E_\gamma = 1.5$ MeV. The problem is to obtain a reliable γ-ray spectrum that is corrected for detector response effects and free of γ rays of higher generations – only primary γ rays must be present. I will discuss this in more detail in the next chapter. The result is that most of the measured strength functions that make up Fig. 3.7 do not extend below ~ 1.5 MeV. One exception is the measurement of ^{151,153}Sm by Simon *et al.* [99], which was performed with a detector set-up including Compton suppression, significantly reducing Compton background. The measurement is shown in Fig. 3.12.

A striking feature of Fig. 3.7 is how nearly every single nucleus below mass $A = 100$ has a low-energy enhancement, while almost no nuclei above $A = 100$ have it. Inspecting Fig. 3.12, we see that the enhancement in this case does not really kick in until E_γ approaches 1 MeV. It is therefore very tempting to speculate that the low-energy enhancement is present throughout the nuclear chart, as suggested in Ref. [137], but that it has been 'hiding' below experimental thresholds in $A > 100$ nuclei. Figure 3.13 illustrates this by comparing parametrisations of strength functions for ^{51}Ti and ^{151}Sm based on measurements. The LEE is parametrised by an exponential function

$$f_{\text{LEE}}(E_\gamma) = Ce^{-\eta E_\gamma} \tag{3.23}$$

with parameters tuned to match the experimental data. The parameter values
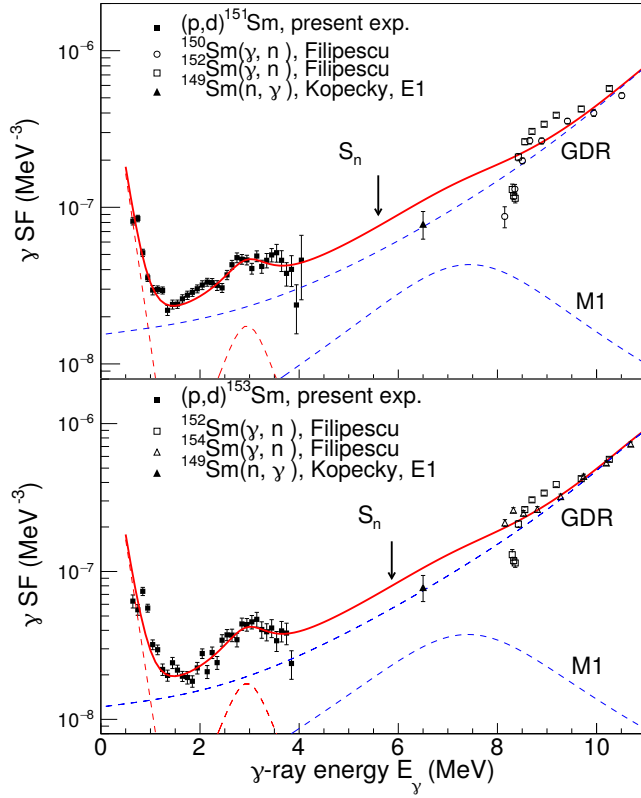
Figure 3.12: Measured γ-ray strength functions for ^{151,153}Sm (top and bottom panel, respectively). The figure is reprinted with permission from Ref. [99].

are very different in the two cases. For ^{51}Ti, the best-fit values are roughly $C = 2 \cdot 10^{-8}$ MeV^{-3}, $\eta = 1$ MeV^{-1}, while for ^{151}Sm they are $C = 2 \cdot 10^{-6}$ MeV^{-3}, $\eta = 5$ MeV^{-1}. An interesting future project would be to attempt to find a mass-dependent parametrisation of C and η, in addition to the deformation dependence suggested by Refs. [142, 143], and see how it compares to experimental data in different mass regions.
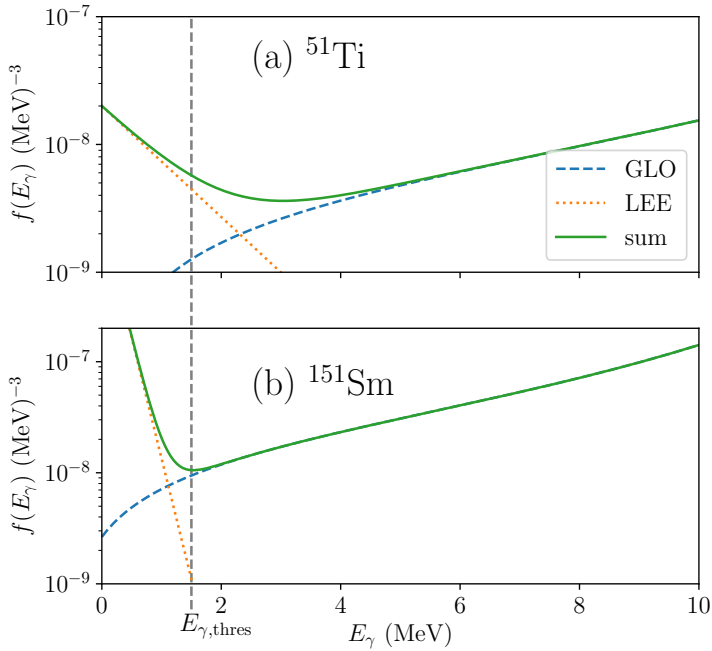
Figure 3.13: Plots of strength functions for ^{51}Ti (a) and ^{151}Sm (b), parametrised by a generalised Lorentzian [90] plus a phenomenological LEE model $f_{\mathrm{LEE}}(E_\gamma) = C\exp(-\eta E_\gamma)$. The parameters have been taken to match Paper IV in this thesis and Ref. [99], respectively. The figure illustrates how the LEE could evolve with mass and 'hide' below experimental thresholds in most $A > 100$ nuclei measured so far.

Chapter 4

The Oslo method

Having discussed the theoretical underpinnings of nuclear physics, with particular emphasis on statistical nuclear properties, I now step over to the experimental side. In this chapter, I give an in-depth discussion of the Oslo method, the technique used for all the experimental work presented in this thesis. The Oslo method is an analysis technique that can be used to extract two average quantities from an experimental dataset: The level density $\rho(E_x)$ and the γ-ray strength function $f(E_\gamma)$. It requires a two-dimensional spectrum, or matrix, sorted by excitation energy and γ-ray energy. An example of such a spectrum is shown in panel a of Fig. 4.1.

The Oslo method relies on the concept of compound nuclear decay. I thus begin this chapter with a discussion of the assumptions behind the compound nucleus picture. I then present the experimental set-up of the classic Oslo method as it is performed at the Oslo Cyclotron Laboratory. Following that, I go into the details of the Oslo method ingredients: detector response unfolding, extraction of first-generation spectra, decomposition into level density and γ-ray strength function and the subsequent normalisation of the decomposed quantities. I also present the work I have done on reimplementing and enhancing the Oslo method software by developing the code OMpy, which is the topic of Paper V [145]. I end the chapter with a discussion about the β-Oslo variety of the method, which carries with it some special challenges.
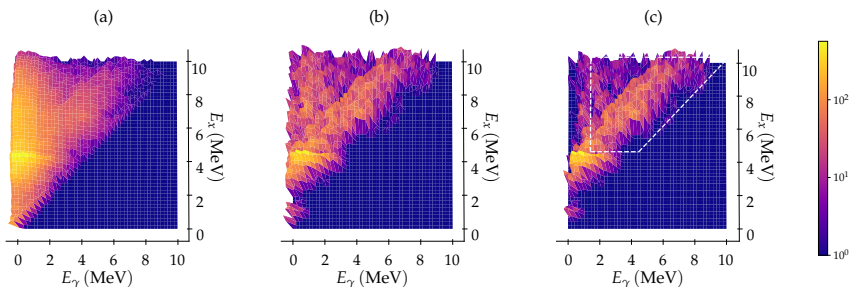
Figure 4.1: Raw (a), unfolded (b) and primary (c) excitation-energy-γ-ray-energy matrices for ^{70}Ni. The white trapezoid shows the extraction region used in the Oslo method analysis – see Section 4.5.2. The figure is reprinted with permission from Ref. [59], included in this thesis as Paper I.

4.1   The compound nucleus picture

Consider a reaction involving a light ion a and a heavy nucleus A. Assume that they form a compound nucleus B which subsequently emits another light ion c to form the nucleus C^*, which is in an excited state E_x below the threshold for particle emission. Finally C^* decays to its ground state C by emission of one or several γ rays. Schematically:

$$aA \rightarrow B \rightarrow cC^* \rightarrow c\gamma C. \tag{4.1}$$

Following Bohr's concept of compound nuclear reactions, we assume that our reaction can be decomposed in two distinct parts (see Ref. [146], also Ref. [11, Vol. I, pp. 184-185]): The formation of the compound nucleus and its subsequent decay. Under this assumption, we may factor the cross section for the reaction $aA \rightarrow c\gamma C$ as

$$\sigma(aA \rightarrow c\gamma C) = \sigma_B(aA)p(B \rightarrow c\gamma C). \tag{4.2}$$

Here, $\sigma_B(aA)$ denotes the cross section for forming the compound nucleus B from the constituents aA, and $p(B \rightarrow c\gamma C)$ is the probability for B to decay to the specific final state $c\gamma C$. This may again be factorised as

$$p(B \rightarrow c\gamma C) = p(B \rightarrow cC^*)\frac{\Gamma_\gamma}{\Gamma}, \tag{4.3}$$

where $p(B \rightarrow cC^*)$ is the probability for the compound nucleus to decay to the state $c\gamma C^*$ and Γ_γ/Γ is the branching ratio for the subsequent γ decay $C^* \rightarrow \gamma C$. Conceptually, the idea is that the time scale for formation of B is much shorter than the time scale for decay, so that the compound nucleus has time to 'forget' how it was made before it decays. This factorisation is crucial to the Oslo method because it enables a separation between formation and decay. The cross-section σ_B will generally be a function of the excitation energy, spin and parity of the populated state in the compound nucleus, $\sigma_B = \sigma_B(E_x, J, \pi)$, but, crucially, independent of the subsequent kinematics of the decay. Experimentally, only final states $c\gamma C$ are selected, so that the influence of $p(B \rightarrow cC^*)$ is removed. The dependence on $\sigma_B(aA)$ must be corrected for when comparing spectra of differing E_x, and is important for the first-generation method which I discuss below, but for a given E_x it factors out.

On the other hand, for a given E_x, J and π, the decay branching ratio depends only on the energy of the emitted photon, $\Gamma_\gamma = \Gamma_\gamma(E_\gamma)$, and since all the nucleus can do to decay is to emit a gamma ray with energy $0 < E_\gamma \leq E_x$ (since we keep to $E_x < S_n$), $\sum_{E_\gamma} \Gamma_\gamma = \Gamma$.

4.2   The experimental set-up

The Oslo method was developed at the Oslo Cyclotron Laboratory (OCL) over the last 30 years with the detector system available there at the time, and

<center>(a)   (b)</center>
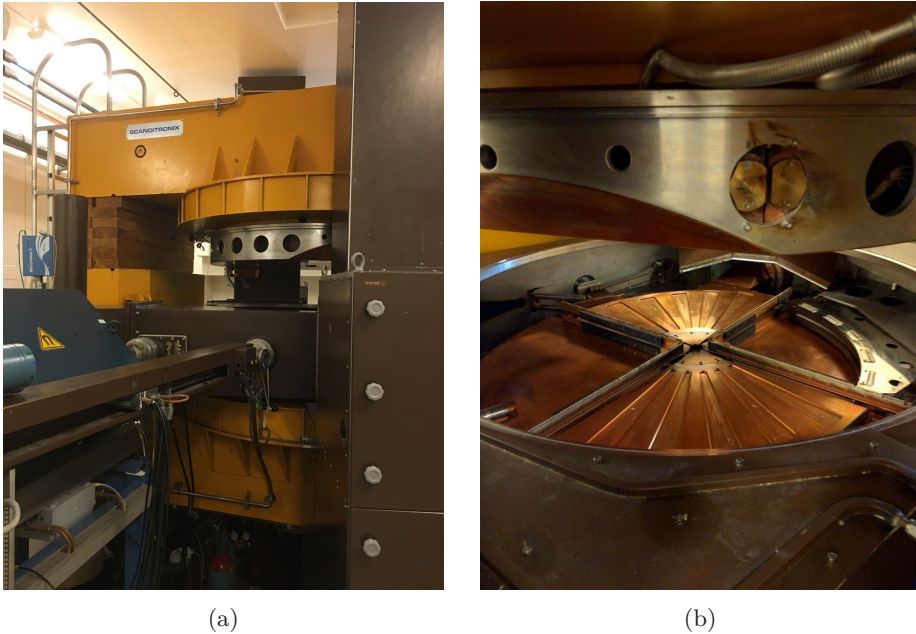
Figure 4.2: The Scanditronix MC-35 cyclotron at the Oslo Cyclotron Laboratory. Panel (a) shows the cyclotron from the outside, while panel (b) shows the inside of the radiofrequency cavity where the ions are accelerated. Pictures courtesy of Dr. A. C. Larsen.

it is instructive to explain the method by relating it to the original type of experiments. The experimental data on ^{59,60}Ni presented in Paper III [54], as well as the data on ^{164}Dy and ^{56}Fe that have been used in Paper V [145], are taken at the OCL using this set-up. However, the Oslo method is not limited to this specific experimental set-up – for instance, the β-Oslo technique used in Paper 1 in this thesis applies the Oslo method to a very different type of experiment.

In an Oslo-method experiment at the OCL, a beam of light ions (p, d, ^{3}He or α) are accelerated by the Scanditronix MC-35 cyclotron to an energy of the order tens of MeV. Figure 4.2 shows pictures of the cyclotron. The beam is then directed to the experimental hall where it impinges on a target foil in the centre of the detector station. The objective is to detect events where a beam particle interacts inelastically with a nucleus in the target X. It can either be an inelastic scattering, *e.g.* $X(p, p'\gamma)X$, or a pick-up or stripping reaction such as $^{A}_{Z}X_N(d, p\gamma)^{A+1}_{Z}Y_{N+1}$. In either case, the impinging projectile deposits energy into the nucleus, either leaving it in an excited state or forming a residual nucleus of differing proton or neutron number, also excited.

The target station in the OCL has a detector set-up consisting of a ring of segmented Si telescopes and an array of γ detectors arranged as a ball. The Si

(a)   (b)
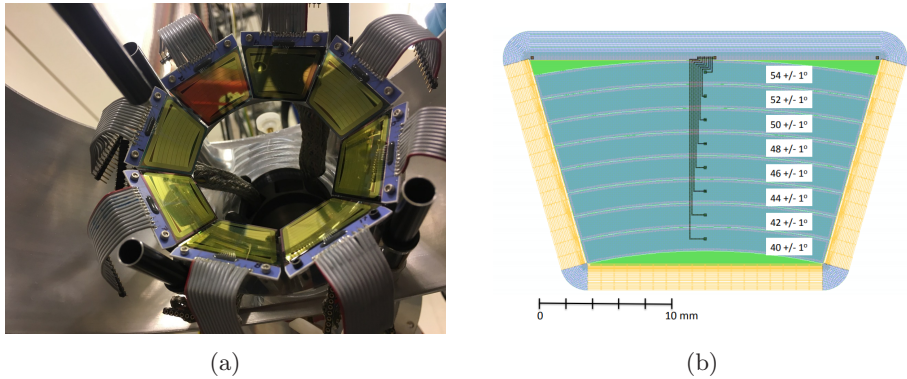
Figure 4.3: A picture of the particle telescope array SiRi (a) and an illustration of the segmentation of the front detectors (b). The picture is courtesy of Dr. A. C. Larsen, while the illustration is reprinted with permission from Ref. [147].

telescope ring, SiRi, consists of eight trapezoidal-shaped detectors as shown in Fig. 4.3. Each of these consist of a thin, 130 μm front detector and a thick, 1550 μm back detector. Light ions from the reaction pass through the front detector depositing some of their energy, before being stopped in the back detector. This enables separation between particles of different mass and charge, as well as detection of the total particle energy. The front detectors are segmented into eight separate areas with individual connectors, giving 64 separate detection areas in total. This allows determination of the two-dimensional angular position. The angular resolution relative to the beam (*i.e.* the polar angle) is about 2 degrees. Until recently the γ-detector array was CACTUS, consisting of 28 collimated $5'' \times 5''$ NaI(Tl) detectors in its full configuration, covering a solid angle of 18% of 4π, with a total efficiency at $E_\gamma = 1332$ keV of 15.2(1)%, as measured with a ^{60}Co source [148]. Very recently, CACTUS has been replaced by OSCAR[1], a vastly superior array consisting of 30 large-volume $3.5'' \times 8''$ LaBr$_3$(Ce) detectors. All the OCL data included in this thesis is taken with CACTUS. In Fig. 4.4 I show pictures of the CACTUS (a) and OSCAR (b) arrays.

If the formed nucleus has an excitation energy lower than the particle separation energy (the neutron separation energy S_n is usually the lowest), then it has to release its excess energy by electromagnetic radiation, *i.e.*, γ rays[2]. The γ rays can be detected by CACTUS, and the outgoing light particle by SiRi. Because SiRi is separated into a front and a back detector (a telescope), it is possible to discriminate between light ions of different mass and charge. As long as the particles are not too energetic, *i.e.* they are stopped completely

---

[1] Oslo SCintillator ARray

[2] With the exception of internal conversion, where the electromagnetic interaction instead kicks out one of the orbital electrons surrounding the nucleus – but this is usually negligible for the cases of interest in this thesis.

<p align="center">(a)   (b)</p>
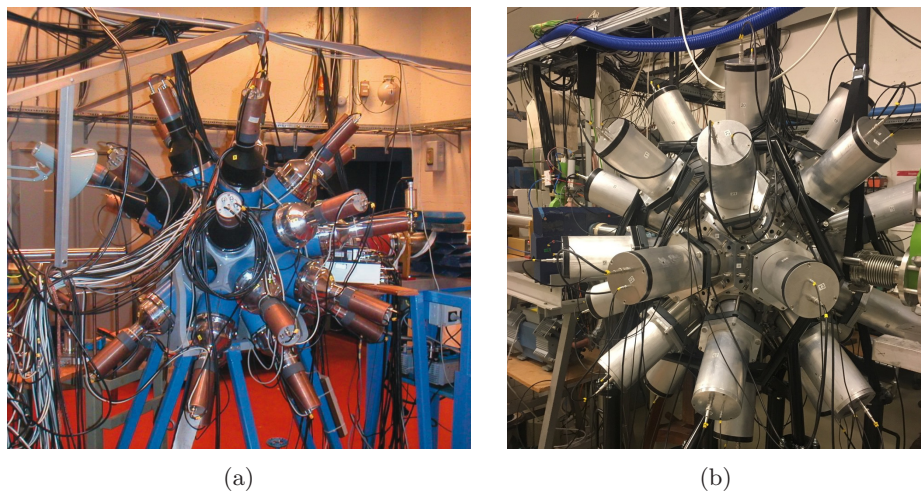
Figure 4.4: The γ-detector arrays at the Oslo Cyclotron Laboratory. Panel (a) shows the old array, CACTUS, while panel (b) shows its successor, OSCAR. Pictures courtesy of Prof. M. Guttormsen and Dr. A. C. Larsen.

inside SiRi, their full energy is known. Then, the angular resolution makes it possible to calculate the excitation energy E_x of the residual nucleus when the light ion was emitted, by using the reaction kinematics. Because of the high dependence of the reaction kinematics on angle, SiRi is often placed backwards, *i.e.* upstream in the beam relative to the target. The polar angular coverage is then 126-140 degrees. This increases the relative detection rate of inelastic events with larger angular momentum transfer as compared to forward angles, and decreases the detection rate of elastically scattered beam particles. By recording thousands of such coincidence events, we build a set of γ spectra tagged with excitation energy – an E_x-E_γ matrix. Ideally, the excitation energy range goes from $E_x = 0$ MeV all the way up to particle threshold (*e.g.* the neutron threshold, S_n). Due to experimental conditions, mainly the limited thickness to stop the particles in SiRi, this is not always possible. The only requirement to use the Oslo method is a complete set of E_x-tagged γ spectra up to some $E_{x,\mathrm{max}}$.

The steps in the Oslo method can be summarised as follows. First, the matrix of E_x-E_γ spectra, hereafter dubbed the *raw* matrix, is *unfolded* to correct for detector response effects of the CACTUS array. Then, the *first-generation method* is applied to extract the spectrum of primary γ rays at each E_x. Finally, two one-dimensional functions, the level density $\rho(E_x)$ and the γ-ray strength function $f(E_\gamma)$, are obtained by fitting their product to the primary γ-ray matrix and normalising to auxiliary data.

4.3   γ-ray energy unfolding

The first step of the Oslo method is to unfold, *i.e.*, deconvolute the γ-ray spectra for each excitation energy to compensate for the distortions to the spectral shape caused by the response of the detector to γ radiation. For example, a γ ray may produce an electron-positron pair by interacting with the detector crystal, and one or both of these may escape detection. This is known as single and double escape, respectively, and the effect in the spectrum is the appearance of artificial peaks at $E'_\gamma = E_\gamma - N m_e c^2 = E_\gamma - N \times 511$ keV for $N = 1$ (single escape) or 2 (double escape). Other effects also influence the response, such as Compton scattering and backscatter, which produces a continuous 'ridge', as well as a peak at $E_\gamma = 511$ keV from positron-electron pairs annihilating in the surroundings of the detector. A more in-depth discussion of response effects can be found in Ref. [149].

In the Oslo method, the effects of detector response are corrected by a technique known as unfolding. Let the detector response be modelled as a conditional probability distribution

$$p(E_\gamma | E'_\gamma), \qquad (4.4)$$

encoding the probability that a γ ray with true energy E'_γ is detected with energy E_γ. In Fig. 4.5, I show some response functions $p(E_\gamma | E'_\gamma)$ for the CACTUS detectors. The response functions are used in the Oslo software package [150]. Given a true γ-ray spectrum $U(E_\gamma)$, the folded spectrum $F(E_\gamma)$, *i.e.*, the spectrum seen by the detector, is then given by

$$F(E_\gamma) = \int p(E_\gamma | E'_\gamma) U(E'_\gamma) \, \mathrm{d}E'_\gamma. \qquad (4.5)$$

By discretising into energy bins of width ΔE_γ, it becomes a matrix equation

$$\vec{F} = P\vec{U}, \qquad (4.6)$$

where P is the response matrix of discrete probabilities $P_{ij} = p(E_{\gamma,i} | E'_{\gamma,j}) \Delta E_\gamma$. In principle, the unfolding procedure amounts to inverting this equation, to obtain $\vec{U}$ from $\vec{F}$. However, a straightforward matrix inversion is ill-advised, as it will produce large, artificial fluctuations in $\vec{U}$ [149, 151]. Instead, the approach taken in the Oslo method is to use an iterative technique which successively approximates U. Letting $\vec{R}$ denote the measured spectrum, the algorithm is

1. Start with a trial function $\vec{U}_0 = \vec{R}$ at iteration $i = 0$

2. Calculate the folded spectrum $\vec{F}_i = P\vec{U}_i$

3. Update the trial function to $\vec{U}_{i+1} = \vec{U}_i + (\vec{R} - \vec{F}_i)$

4. Iterate from 2 until $\vec{F}_i \approx R$. The criterion for terminating the iterations is taken as a weighted sum of the root-mean-square error of $\vec{F}_i - \vec{R}$ and the level of fluctuations in $\vec{U}_i$. The fluctuations are estimated as $\sum_l |U_{i,l} - \vec{S}_i|$, where $\vec{S}_i$ is a smoothed version of the spectrum $\vec{U}_i$.
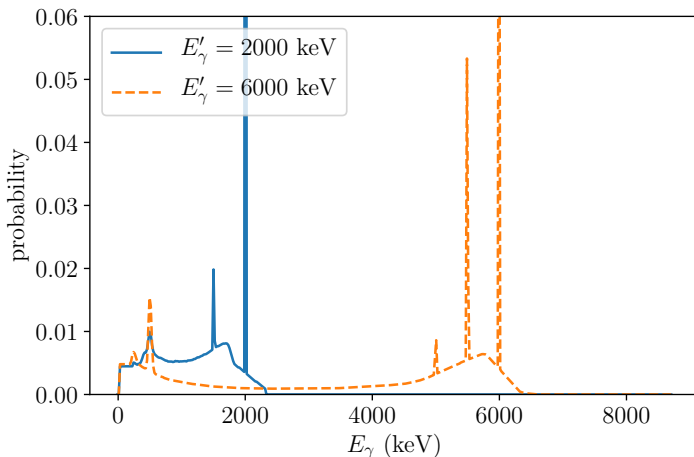
Figure 4.5: Response functions for the NaI(Tl) detectors of CACTUS for some selected incident γ-ray energies, taken from the Oslo-method software package [150]. The curves show the probability that a γ-ray with true energy E_γ' is detected with energy E_γ. Note that the full-energy peaks exceed the limit on the y axis. The response functions have not been folded with the detector resolution – hence, a realistic experimental response spectrum would exhibit peaks that are less sharp.

In addition to this, Ref. [149] presents a further refinement to the unfolding method known as Compton subtraction. It is used to further control the fluctuations in the unfolded spectrum. The basic concept behind it is to use the previously unfolded spectrum to decompose $\vec{R}$ into parts corresponding to the full-energy, single and double escape and annihilation peaks, and the 'rest' which comes from Compton scattering and backscattering from the surroundings. Each of these parts, save for the full-energy peak, are then smoothed with the detector resolution before they are subtracted from $\vec{R}$. The resulting spectrum is then multiplied up to maintain the number of counts. The idea is that this gives an unfolded spectrum with the same statistical fluctuations as in the original spectrum $\vec{R}$. An example of an unfolded γ-ray spectrum is shown in panel b of Fig. 4.1.

4.4 Extraction of the primary γ-ray matrix

The second step of the Oslo method is the determination of the *first-generation*, or *primary*, γ-ray spectrum for each excitation-energy bin. Here, an iterative algorithm is applied as described in Ref. [152]. Let $FG(E_\gamma)_{E_x}$ denote the first-generation γ-ray spectrum, i.e., the intensity distribution of γ-ray decay from a given excitation energy E_x, as function of γ-ray energy E_γ. Generally, the

nucleus will decay from E_x down to the ground state by a path involving one or several states E'_x of $0 < E'_x < E_x$, emitting a cascade of γ rays in the process. These form the *total* γ-ray spectrum. The total, or all-generations γ-ray spectrum, denoted $AG(E_\gamma)_{E_x}$, can be viewed as a superposition of the first-generation spectrum and a weighted sum of the all-generations spectra of excitation energies below,

$$AG(E_\gamma)_{E_x} = FG(E_\gamma)_{E_x} + \sum_{E'_x < E_x} n(E'_x)_{E_x} w(E'_x)_{E_x} AG(E_\gamma)_{E'_x}. \qquad (4.7)$$

Here, $n(E'_x)_{E_x}$ is a normalisation factor that corrects for the varying cross section to populate the E'_x bins, and $w(E'_x)_{E_x}$ is a weighting factor. The normalisation factor can be estimated from the total γ-ray spectrum by the relation

$$n(E'_x)_{E_x} = \frac{M(E'_x)N(E_x)}{M(E_x)N(E'_x)}, \qquad (4.8)$$

where $M(E_x)$ and $N(E_x)$ denote the average γ-ray multiplicity and the total number of counts, respectively, at excitation energy E_x. The average multiplicity can again be estimated from the spectrum by the relation

$$M(E_x) = \frac{E_x}{\langle E_\gamma \rangle}, \qquad (4.9)$$

where $\langle E_\gamma \rangle$ is the weighted-average γ-ray energy at excitation energy E_x. The weight function $w(E'_x)$ encodes the probability for the nucleus to decay from E_x to E'_x, and is in fact nothing but the normalised first-generation spectrum for E_x,

$$w(E'_x)_{E_x} = \frac{FG(E_x - E'_x)_{E_x}}{\sum_{E'_\gamma} FG(E'_\gamma)_{E_x}} \qquad (4.10)$$

By rewriting Eq. (4.7), we obtain

$$FG(E_\gamma)_{E_x} = AG(E_\gamma)_{E_x} - \sum_{E'_x < E_x} n(E'_x)_{E_x} \frac{FG(E_x - E'_x)_{E_x}}{\sum_{E'_\gamma} FG(E'_\gamma)_{E_x}} AG(E_\gamma)_{E'_x}. \qquad (4.11)$$

This is a self-consistent set of equations for the FG spectra, which we solve by an iterative procedure, starting with a set of trial functions $FG(E_\gamma)_{E_x}$ and iterating until convergence is reached. The trial functions are chosen as constant functions, *i.e.* with the same value for all E_γ. The resulting first-generation γ-ray matrix is shown in panel c of Fig. 4.1.

4.5 Decomposition into two functions

With the primary matrix at hand, the next step of the Oslo method consists of a decomposition by fitting the normalised first-generation $P(E_x, E_\gamma)$ spectra to a product of two one-dimensional functions, namely the nuclear level density, $\rho(E_x)$, and the γ-ray strength function, $f(E_\gamma)$. This decomposition and the assumptions behind it will now be discussed in detail.

4.5.1 Derivation of the decomposition equation

We want to relate the distribution of primary γ rays to the strength function and level density. This is done by considering Fermi's golden rule[3] [153, 154], which says that the probability of decay from a specific initial state i into a quasi-continuum of final states f is given to first order in perturbation theory as

$$\omega_{i \to f} = \frac{2}{\epsilon_0 \hbar} \frac{\lambda + 1}{\lambda[(2\lambda + 1)!!]^2} \left(\frac{E_\gamma}{\hbar c} \right)^{2\lambda+1} B(XL; i \to f) \rho_{\text{avail}}(f), \qquad (4.12)$$

where $\rho_{\text{avail}}(f)$ is the density of available final states f and $B(\sigma\lambda; i \to f)$ is the reduced transition probability.[4] The γ-ray strength function for a given multipolarity XL and for nuclear states with a given excitation energy E_x, spin J and parity π, as given in Eq. (3.12), is [73]

$$f_{XL}(E_\gamma, E_x, J, \pi) = \frac{\langle \Gamma_\gamma^{XL}(E_\gamma, E_x, J, \pi) \rangle \rho(E_x, J, \pi)}{E_\gamma^{2L+1}} \qquad (4.13)$$

$$= a_{XL} \langle B(XL; E_x J\pi \to (E_x - E_\gamma) J_f \pi_f) \rangle \rho(E_x, J, \pi), \quad (4.14)$$

where $\langle \cdots \rangle$ denotes an average over individual transitions in the vicinity of E_γ, E_x (in practice defined by the energy binning resolution), $\rho_{J,\pi}(E_x)$ is the density of spin-J, parity-π levels at energy E_x and a_{XL} is a constant. Taking the average over Eq. (4.12) in a vicinity around E_x, E_γ and substituting, we obtain

$$\langle \omega_{i \to f} \rangle = \frac{2}{\epsilon_0 \hbar a_{XL}} \frac{\lambda + 1}{\lambda[(2\lambda + 1)!!]^2} \left(\frac{E_\gamma}{\hbar c} \right)^{2\lambda+1} \frac{f_{XL}(E_\gamma, E_x, J_i, \pi_i)}{\rho_{J_i, \pi_i}(E_x)} \rho_{\text{avail}}(E_f), \qquad (4.15)$$

where $E_f = E_x - E_\gamma$. In the Oslo method, since the decays happen at high E_x, we assume that dipole radiation dominates. This is well supported experimentally [97, 99, 102, 125]. The selection rules dictate that dipole radiation changes the angular momentum J by at most one unit. For $M1$, the parity is unchanged, while for $E1$ it flips. This determines the density of available final states for the decay,[5]

$$\rho_{\text{avail}}(E_f) = \sum_{J_f = J_i - 1}^{J_i + 1} 3\rho(E_f, J_f, \pi_f). \qquad (4.16)$$

---

[3]Fermi's golden rule should really be called Dirac's golden rule. It was Paul Dirac who first derived it, while Enrico Fermi later coined the name 'golden rule'.

[4]This follows from the golden rule as shown in *e.g.* appendix B of Ref. [155], but the final state density has been modified to take into account the fact that the decay goes into a quasi-continuum of nuclear levels.

[5]In the case of $J_i = 1/2$ the sum runs over $J_f = \{1/2, 3/2\}$, and in the case of $J_i = 0$, the sum only runs over $J_f = 1$, since $J = 0 \to J = 0$ transitions are forbidden.

The factor 3 comes from the distinction between levels and states.[6] For a nuclear level with a given J_f, there are $2J_f + 1$ distinct magnetic substates. However, in an electromagnetic dipole decay, the total M quantum number cannot change by more than one unit, which means that only three of the magnetic substates are available, independent of J_f. We may then write the average total dipole transition rate $\langle \omega \rangle \equiv \langle \omega_{E1} \rangle + \langle \omega_{M1} \rangle$ as

$$\langle \omega_{J_i, \pi_i}(E_x, E_\gamma) \rangle = \frac{C E_\gamma^3}{\rho_{J_i, \pi_i}(E_x)} \left(f_{E1}(E_\gamma, E_x, J_i, \pi_i) \sum_{J_f = J_i - 1}^{J_i + 1} \rho(E_f, J_f, -\pi_i) \right.$$

$$\left. + f_{M1}(E_\gamma, E_x, J_i, \pi_i) \sum_{J_f = J_i - 1}^{J_i + 1} \rho(E_f, J_f, +\pi_i) \right), \tag{4.17}$$

where all constants have been grouped together and named C for brevity. Let us next define the total dipole strength function f_1 by

$$f_1 = f_{E1} + f_{M1}. \tag{4.18}$$

To factor the expression, we need to assume parity equilibration of the level density, *i.e.* $\rho(E_x, J, +) \approx \rho(E_x, J, -)$. Then we can write

$$\langle \omega_{J_i, \pi_i}(E_x, E_\gamma) \rangle = \frac{C E_\gamma^3}{\rho_{J_i, \pi_i}(E_x)} f_1(E_\gamma, E_x, J_i, \pi_i) \sum_{J_f = J_i - 1}^{J_i + 1} \rho(E_f, J_f, \text{eq}), \tag{4.19}$$

where $\rho(E_x, J_f, \text{eq})$ denotes the level density of one parity, the notation emphasising the assumption of parity equilibration.

Assuming that E_x is below the threshold energy for particle emission, and that dipole radiation dominates, Eq. (4.19) represents all possible decay modes. We may thus exploit probability conservation and write

$$P_{J_i, \pi_i}(E_x, E_\gamma) = \frac{\langle \omega_{J_i, \pi_i}(E_x, E_\gamma) \rangle}{\sum_{E_\gamma} \langle \omega_{J_i, \pi_i}(E_x, E_\gamma) \rangle} \tag{4.20}$$

$$= D E_\gamma^3 f_1(E_\gamma, E_x, J_i, \pi_i) \rho_{J_f, \text{eq}}(E_x - E_\gamma) \tag{4.21}$$

where D is another normalisation constant. Note that the density of initial states cancels out.

The final step is to remove the dependence on J and π, since we cannot discriminate between them experimentally. By the generalised Brink–Axel hypothesis, as discussed in the previous chapter, the strength function is approximately independent of E_x, J and π, so we may write

$$f_1(E_\gamma, E_x, J_i, \pi_i) \approx f_1(E_\gamma). \tag{4.22}$$

---

[6]Strictly speaking, the factor is less than 3 when J_f is less than 1. We assume that this is a small correction and can be neglected.

The normalised, experimental first-generations matrix $P(E_x, E_\gamma)$ is a superposition of the individual $P_{J_i, \pi_i}(E_x, E_\gamma)$, weighted by the probability $g_{\text{pop}}(E_x, J_i, \pi_i)$ to populate different spins and parities at each E_x:

$$P(E_x, E_\gamma) = \sum_{J_i, \pi_i} g_{\text{pop}}(E_x, J_i, \pi_i) P_{J_i, \pi_i}(E_x, E_\gamma). \qquad (4.23)$$

Inserting, this gives

$$P(E_x, E_\gamma) = DE_\gamma^3 f_1(E_\gamma) \sum_{J_i, \pi_i} g_{\text{pop}}(E_x, J_i, \pi_i) \sum_{J_f = J_i - 1}^{J_i + 1} \rho(E_x - E_\gamma, J_f, \text{eq}).$$
$$(4.24)$$

Lastly, we may write the partial level density $\rho(E_x - E_\gamma, J_f, \text{eq})$ as

$$\rho(E_x - E_\gamma, J_f, \text{eq}) = g_{\text{int}}(E_x - E_\gamma, J_f, \text{eq}) \rho(E_x - E_\gamma), \qquad (4.25)$$

where g_{int} denotes the intrinsic spin distribution of the nucleus and $\rho(E_x)$ is the total nuclear level density. Factoring out, we obtain

$$P(E_x, E_\gamma) = DE_\gamma^3 f_1(E_\gamma) \rho(E_x - E_\gamma) z(E_x, E_\gamma), \qquad (4.26)$$

where we have defined

$$z(E_x, E_\gamma) = \sum_{J_i, \pi_i} g_{\text{pop}}(E_x, J_i, \pi_i) \sum_{J_f = J_i - 1}^{J_i + 1} g_{\text{int}}(E_x - E_\gamma, J_f, \text{eq}). \qquad (4.27)$$

In the Oslo method, it is assumed that $z(E_x, E_\gamma) \approx$ constant. This is not completely correct, but the correction is believed to be small. The factor z could, however, potentially have a *systematic* impact on the end results of the method. The extracted quantities $\rho(E_x)$ and $f(E_\gamma)$ are coupled through the normalisation parameter α (see Section 4.6 below). The presence of another E_x- and E_γ-dependent factor in the decomposition equation influences this coupling. It could thus be that when α is determined by normalising $\rho(E_x)$ to auxiliary data at low and high E_x, the resulting, coupled slope of $f(E_\gamma)$ is not completely right – because the quantity being coupled is in fact not $f(E_\gamma)$, but rather $f(E_\gamma) z(E_x, E_\gamma)$. Since z is sensitive to the distribution of populated spins $g_{\text{pop}}(E_x, J_i)$, which in many cases is narrower than g_{int} but never broader, there could be a systematic correction that is missing. This would presumably be most important for experiments where the populated spin range is particularly small, such as with heavy actinide targets [156–158] or in the β-Oslo method (see Section 4.8 below). Figure 4.6 shows plots of $z(E_x, E_\gamma)$ for two different spin selection criteria. In both cases, the Ericson spin distribution (Eq. (3.8)) with the Guttormsen spin-cutoff parametrisation (Eq. (3.11)) has been used for both g_{pop} and g_{int}, with the same parameters as those used for ^{163}Dy in Ref. [133]. However, in Fig. 4.6a, the sum over J_i in Eq. (4.27) runs over all available values, while in Figs. 4.6b and 4.6c, it is restricted to $J_i = 5, 6, 7$ and
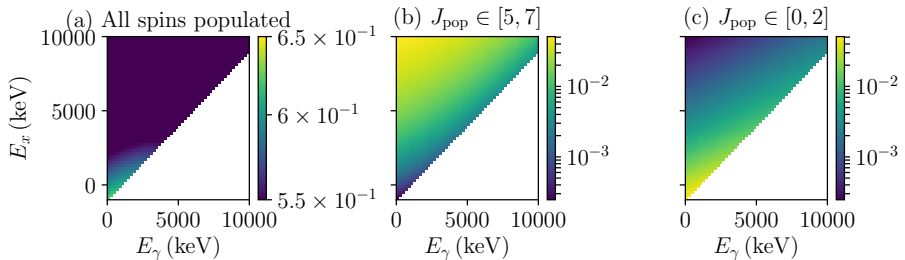
Figure 4.6: Plot of the correction factor $z(E_x, E_\gamma)$ for (a) a broad spin population range corresponding to the intrinsic spin distribution, (b) the range $J_{\mathrm{pop}} = 5, 6, 7$ and (c) the range $J_{\mathrm{pop}} = 0, 1, 2$.

$J_i = 0, 1, 2$, respectively. The case $J_i = 5, 6, 7$ is chosen because it mimics the case of the β-Oslo experiment on ^{70}Ni in Paper I [59] (see Section 4.8 below), albeit for a very different nucleus. The case $J_i = 0, 1, 2$ resembles the situation with a heavy actinide target [157].

However, it is not apparent from Fig. 4.6 what impact $z(E_x, E_\gamma)$ has on the level density and γ-ray strength function. Together with Fabio Zeiser, I have done a preliminary test where we included the z factor in the fitting module in OMpy (see below) to see what effect it has on the final result. Figure 4.7 shows a comparison of fits made to the ^{163}Dy data set from Ref. [133], which is also used in Paper V [145]. We have done four separate fits, one where we neglect the correction factor, and three fits corresponding to the three $z(E_x, E_\gamma)$ distributions shown in Fig. 4.6. Figure 4.7 shows the result of the four different fits. Panels (a) and (c) show level densities, while panel (b) and (d) show strength functions. The same fits are used in the top and bottom panels, but with different transformation parameters: In the top panels, the functions have been transformed so that their γ-ray strength functions align, while the bottom panels align the level densities instead. There is not much change in the individual fits – the relative positions of neighbouring function values appears unaltered. The slope-coupling between the level density and strength function, however, is modified. The no-correction-factor fit (blue solid line) and $g_{\mathrm{pop}} = g_{\mathrm{int}}$ (red dash-dotted curve) look identical, which indicates that neglecting the z factor is justified in cases of broad spin population. This is also consistent with Fig. 4.6a, which shows that $z(E_x, E_\gamma)$ is constant for E_x in the extraction region, 3 MeV to 6.5 MeV. The fit with $J_i = 0, 1, 2$ (green dotted line) gets a slightly modified slope coupling, giving rise to a somewhat smaller (larger) level density (γ-ray strength function) at low energies. The opposite happens, and is more pronounced, in the fit with $J_i = 5, 6, 7$ (orange dashed line).

Since the level density is the quantity that is easiest to constrain by auxiliary data at low and high E_x (see Section 4.6 below), the lower panels in Fig. 4.7 are perhaps the most interesting. If there is a systematic correction in the Oslo
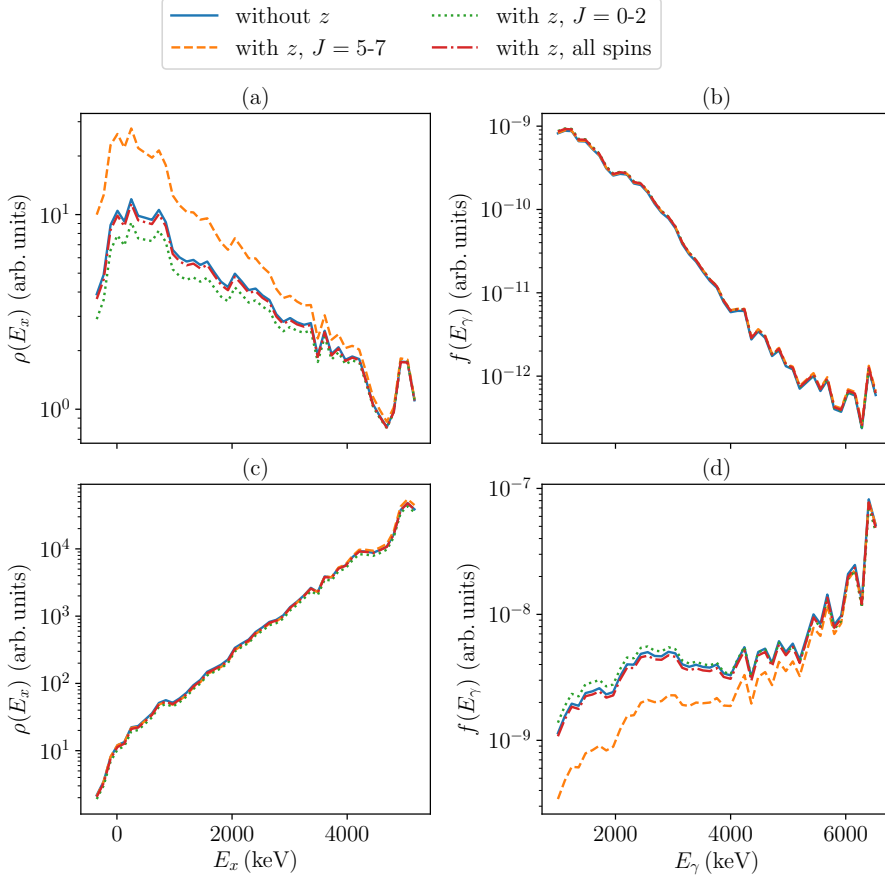
Figure 4.7: Comparison of fitted $\rho(E_x)$ (left) and $f(E_\gamma)$ (right) for ^{163}Dy [113, 133] with and without the $z(E_x, E_\gamma)$ factor included in the fit. The top (a and b) and bottom (b and c) panels show the same fits of the level density (a, c) and strength function (b, d), respectively, but with different choices of normalisation parameters. The functions in the upper panel are transformed to have matching γ-ray strength functions, while those in the lower panel are matched on level density instead. The blue, solid curves show the fit without the z factor, while the orange dashed, green dotted and red dash-dotted lines show fits corresponding to the $z(E_x, E_\gamma)$ distributions shown in panels a–c of Fig. 4.6, respectively.

method that has not been taken into account, and it affects the slope coupling, then it is likely to have resulted in an altered slope on the γ-ray strength rather than the level density.

In light of Fig. 4.7, the different $z(E_x, E_\gamma)$ in Fig. 4.6 are easier to interpret: The all-spins case in Fig. 4.6a is flat and does not alter the fit. The high-spin selection in Fig 4.6b gives rise to a $z(E_x, E_\gamma)$ that has a downward slope as function of E_γ, giving rise to an E_γ-dependent correction that tilts the γ-ray strength function counter-clockwise. The opposite happens in Fig. 4.6c, where $z(E_x, E_\gamma)$ slopes upward as function of E_γ and makes the strength function tilt clockwise. I stress that these are very preliminary results, and must be viewed with scepticism. However, if they are true, and this is a general trend, it is interesting because it could have implications for the shape and magnitude of the low-energy enhancement and for the $M1$ scissors mode. An effort is under way to further investigate the importance of the correction factor, and to see if it is worth properly including in the Oslo method analysis [159].

For the following discussion, I will assume that $z(E_x, E_\gamma) \approx$ constant, so that the Oslo method equation (4.26) is given by

$$P(E_x, E_\gamma) = D E_\gamma^3 f_1(E_\gamma) \rho(E_x - E_\gamma) \tag{4.28}$$

for a suitable normalisation constant D. This concludes the derivation of the Oslo method equation, and shows that the first-generation spectrum is proportional to the product of two functions where one depends only on E_γ and the other depends only on $E_f = E_x - E_\gamma$, enabling us to make a global fit.

4.5.2 Fitting the functions

For the discussion concerning the fitting procedure, it is convenient to exchange the γ-ray strength function $f(E_\gamma)$ by the γ-ray transmission coefficient $\mathcal{T}(E_\gamma)$. The two are related as [160]

$$\mathcal{T}(E_\gamma) = 2\pi E_\gamma^3 f(E_\gamma), \tag{4.29}$$

which gives the rewritten equation [161]

$$P_{\text{fit}}(E_x, E_\gamma) \propto \mathcal{T}(E_\gamma) \rho(E_x - E_\gamma). \tag{4.30}$$

The fit of $\rho(E_x - E_\gamma)$ and $\mathcal{T}(E_\gamma)$ to data is carried out as follows. First, we select a suitable bin size ΔE, typically $100 - 300$ keV depending on the experimental E_x resolution and to obtain sufficient statistics in each bin. The first-generation matrix is rebinned along both the E_x and E_γ axes to this bin size. We then obtain the matrix of experimental decay probabilities, $P_{\text{exp}}(E_x, E_\gamma)$, by normalising the spectrum in each E_x bin to unity. Only a region of the $P(E_x, E_\gamma)$ matrix defined by $E_{x,\text{min}} < E_x < E_{x,\text{max}}$, $E_{\gamma,\text{min}} < E_\gamma < E_{\gamma,\text{max}}$ is used in the fit. Here, $E_{x,\text{min}}$ is set to a high enough value to ensure that the decays happen in the statistical regime, $E_{x,\text{max}}$ is limited by the experimental reach or the neutron threshold, $E_{\gamma,\text{min}}$ is limited by detector thresholds and uncertainties

in the unfolding procedure, and $E_{\gamma,\max}$ is given by $E_{x,\max}$ plus the resolution of the γ detectors $\Delta E_\gamma(E_{x,\max})$. In panel c of Fig. 4.1, the first-generation spectrum of ^{70}Ni from Paper I [59] is shown with the extraction region drawn as a white trapezoid. The energy ranges for $\rho(E_x)$ and $\mathcal{T}(E_\gamma)$ are determined by this extraction region: $\rho(E_x)$ is extracted for $E_x \in [0, E_{x,\max} - E_{\gamma,\min}]$ and $\mathcal{T}(E_\gamma)$ for $E_\gamma \in [E_{\gamma,\min}, E_{\gamma,\max}]$.

For the fit of ρ and $\mathcal{T}$, we take the function value in each bin as a free parameter. For an energy span of 10 MeV, with $\Delta E = 200$ keV, this gives about 100 free parameters for ρ and $\mathcal{T}$ combined. However, each bin of $P_{\exp}(E_x, E_\gamma)$ contributes one constraint, giving $\mathcal{O}(50^2/2 = 1250)$ constraints. Hence, the fit is highly over-constrained.

For a given pair of trial functions $(\rho, \mathcal{T})$, we construct the corresponding matrix $P_{\text{fit}}(E_x, E_\gamma)$ by

$$P_{\text{fit}}(E_x, E_\gamma) = N_{E_x} \rho(E_x - E_\gamma)\mathcal{T}(E_\gamma), \qquad (4.31)$$

where N_{E_x} is a normalisation coefficient so that $\sum_{E_\gamma} P_{\text{fit}}(E_x, E_\gamma) = 1$ for each E_x bin. We fit P_{fit} by a minimal-χ^2 approach, minimising the weighted sum-of-squared errors

$$\chi^2 = \sum_{E_x, E_\gamma} \left(\frac{P_{\exp}(E_x, E_\gamma) - P_{\text{fit}}(E_x, E_\gamma)}{\sigma_{P_{\exp}}(E_x, E_\gamma)} \right)^2, \qquad (4.32)$$

where $\sigma_{P_{\exp}}(E_x, E_\gamma)$ is the matrix of standard deviations on the experimental primary spectra. The use of a χ^2 minimisation is only strictly justified if the data being fit have Gaussian errors. In our case, the counting experiments are governed by Poisson statistics, and the Gaussian distribution is a good approximation. See Appendix B for a more thorough discussion about statistics and χ^2 fitting.

4.5.3 Numerical minimisation

With the probability-theoretical considerations out of the way, it remains to obtain the best-fit estimate for ρ and $\mathcal{T}$. This is achieved by numerical minimisation. All Oslo method analyses up to now have been carried out using the Oslo software package [150], written by Prof. Magne Guttormsen, Dr. Andreas Schiller and others. In the package, a program called `rhosigchi` handles the decomposition and fit. It uses the iterative gradient descent method derived in Ref. [161] to obtain the χ^2 minimum.

A shortcoming of the original Oslo method implementation has been the estimation of the uncertainty matrix $\sigma_{P_{\exp}}(E_x, E_\gamma)$ for the χ^2 fit. Due to the lack of a complete statistical uncertainty propagation, one has had to resort to an approximate uncertainty estimation. This is discussed in detail in Ref. [161]. A major part of my PhD work is dedicated to addressing this. As a result, I have written a complete reimplementation of the Oslo method in the Python

programming language, named OMpy.[7] It is the topic of Paper V [145], and the code is available from Ref. [162]. The OMpy code uses a different minimisation approach, employing the numerical minimisation algorithm Powell [163] from the Scipy library [164]. Because of the new uncertainty propagation in OMpy, we have access to a proper uncertainty matrix $\sigma_{P_{\mathrm{exp}}}$ for the fit. The details of the uncertainty propagation is discussed below – but first, we must cover the topic of normalisation.

4.6 Normalisation

In Ref. [161], it is shown that the minimal-χ^2 fit of $\rho(E_x)$ and $\mathcal{T}(E_\gamma)$ has a degree of degeneracy in its minimum. The χ^2 value is invariant under a transformation by a continuous three-parameter Lie group $G(A, \alpha, B)$ given by

$$\rho(E_x), \mathcal{T}(E_\gamma) \xrightarrow{G} Ae^{\alpha E_x}\rho(E_x), Be^{\alpha E_\gamma}\mathcal{T}(E_\gamma). \tag{4.33}$$

Note that $f(E_\gamma)$ transforms in the same way as $\mathcal{T}(E_\gamma)$ (Eq. (4.29)). Because the normalised values of the level density and strength function span many decades, it is customary to look at them in logarithmic plots. In terms of logarithmic function values, the A and B parameters correspond to a constant shift in all values of ρ and $\mathcal{T}$, respectively, and the α parameter rotates the linear slope of both functions. Hence, α couples the normalisations together. As far as we know, there is no way to discriminate between different solutions (*i.e.* parameter values for G) using only the primary matrix. In Fig. 4.8, I show the 'raw', unnormalised fit with OMpy to the ^{164}Dy data set from Paper V [145]. Only one of the solutions gives the true shape of the functions. Obtaining this solution is called normalisation, and must be done using auxiliary data. Usually, knowledge of the discrete level structure at low E_x is used together with an estimate for $\rho(S_n)$, based on D_0 resonance spacings from (n, γ) experiments together with a spin distribution function. This is enough to determine both A and α. The B parameter can be determined from data on the average total radiative width at S_n from (n, γ) experiments, $\langle \Gamma_\gamma(S_n, J_t \pm 1/2, \pi_t)\rangle$, where J_t, π_t denote the spin and parity, respectively, of the target nucleus undergoing neutron capture. The average total radiative width is related to $\mathcal{T}(E_\gamma)$ through the relation

$$\langle \Gamma_\gamma(S_n, J_t \pm 1/2, \pi_t)\rangle$$
$$= \frac{1}{2}\left(\langle \Gamma_\gamma(S_n, J_t - 1/2, \pi_t)\rangle + \langle \Gamma_\gamma(S_n, J_t + 1/2, \pi_t)\rangle\right), \tag{4.34}$$

---

[7]OMpy is a collaborative effort. Most of the code, as well as the program structure, is designed and written by me. Fabio Zeiser has contributed the routine for χ^2 minimisation. Also, Erlend Lima is, at the time of writing, working on refining the code structure and implementing automatic code tests. My coding has also benefited immensely from discussions with both of them.
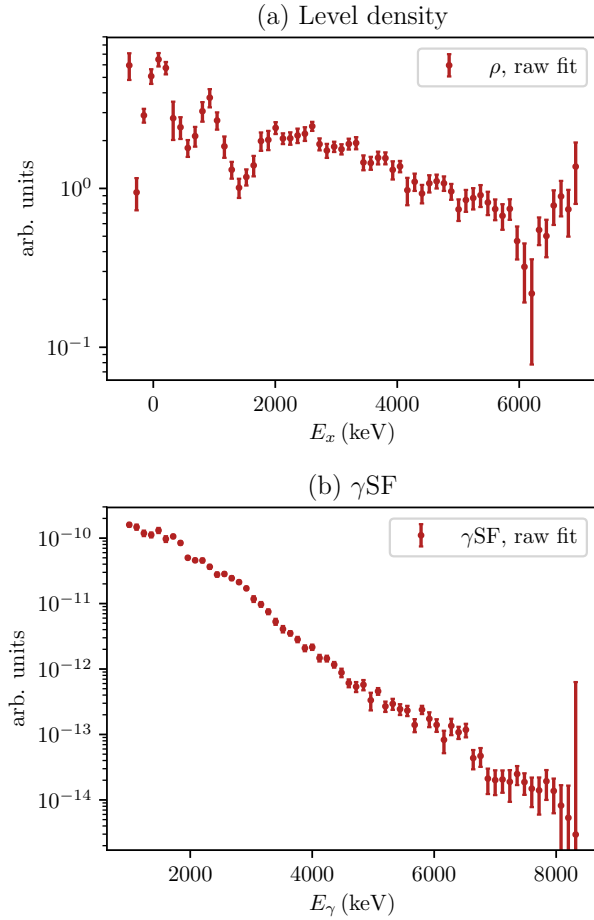
Figure 4.8: Unnormalised best-fit $\rho(E_x)$ (left) and $f(E_\gamma)$ (right) for ^{164}Dy [113, 133]. The figure is from Ref. [145], included as Paper V in this thesis.

where $\langle \Gamma_\gamma(E_x, J, \pi) \rangle$ is given by the integral

$$\langle \Gamma_\gamma(E_x, J, \pi) \rangle \qquad\qquad\qquad\qquad\qquad\qquad\qquad\qquad (4.35)$$

$$= \frac{D_0}{2\pi} \int_0^{E_x} \mathrm{d}E_\gamma \, B\mathcal{T}(E_\gamma)\rho(E_x - E_\gamma) \sum_{\pi=\pm} \sum_{I=-1}^{1} g_{\text{int}}(E_x - E_\gamma, J + I, \pi).$$

Here, g_{int} is the intrinsic spin distribution of the nucleus. See Appendix A for a derivation of the γ-ray strength function based on this integral.

The auxiliary normalisation is a major source of uncertainty for the final results of the Oslo method [165], not least because of the spin distribution, which is experimentally unknown and has to be estimated from a model, as discussed in the previous chapter.

In principle, all the three parameters of G should be combined in a probability model and fitted simultaneously. In practice, this has proven technically challenging, and usually the level density $\rho(E_x)$ is therefore normalised first to determine A and α, before using $\mathcal{T}(E_\gamma)$ with the chosen α to determine B. We have recently begun investigating methods to fit all parameters simultaneously. Statistically, it amounts to constructing a joint likelihood for the parameters A, α and B given the constraints from all auxiliary data (see Appendix B for an introduction to likelihoods):

$$\mathcal{L}(A, \alpha, B) = \mathcal{L}_{\text{discrete}}(A, \alpha) \times \mathcal{L}_{\rho(S_n)}(A, \alpha) \times \mathcal{L}_{\langle \Gamma_\gamma \rangle}(\alpha, B). \qquad (4.36)$$

Assuming Gaussian errors, the likelihoods can be constructed from χ^2's, *e.g.*,

$$\ln \mathcal{L}_{\text{discrete}}(A, \alpha) = -\frac{1}{2} \sum_{\text{discr.region}} \frac{(\rho_{\text{discrete}}(E_x) - \rho_{\text{fit}}(E_x; A, \alpha))^2}{\sigma_{\text{discrete}}^2 + \sigma_{\text{fit}}^2}. \qquad (4.37)$$

To carry out the fit and obtain a proper uncertainty quantification, it is necessary to adopt a Bayesian framework with prior assumptions on the parameters [166]. Figure 4.9 shows a preliminary test I have done with this approach, using a data set from an experiment with the $^{184}W(\alpha, p)^{187}Re$ reaction. For this, I used a slightly different set of auxiliary data, namely the experimental levels at low E_x together with data on $f(E_\gamma)$ above neutron threshold from an (n, γ) experiment [167]. The absence of experimental $\rho(S_n)$ information mimicks cases where the β-Oslo method (see below) is applied to unstable, neutron-rich nuclei, where auxiliary normalisation data other than low-energy level structure is scarce. I discuss some more details of the fit in Appendix B. The benefit of performing a simultaneous, global fit is that correlations between the parameters is taken into account. As can be seen in the figure, the correlation can be quite strong and highly non-linear. By taking proper account of the correlations, the final, quoted uncertainties on the parameter values could be reduced.

4.7 Propagation of statistical uncertainties

As already mentioned, proper quantification of uncertainties has been lacking in the Oslo method. The problem is that the unfolding and first generation
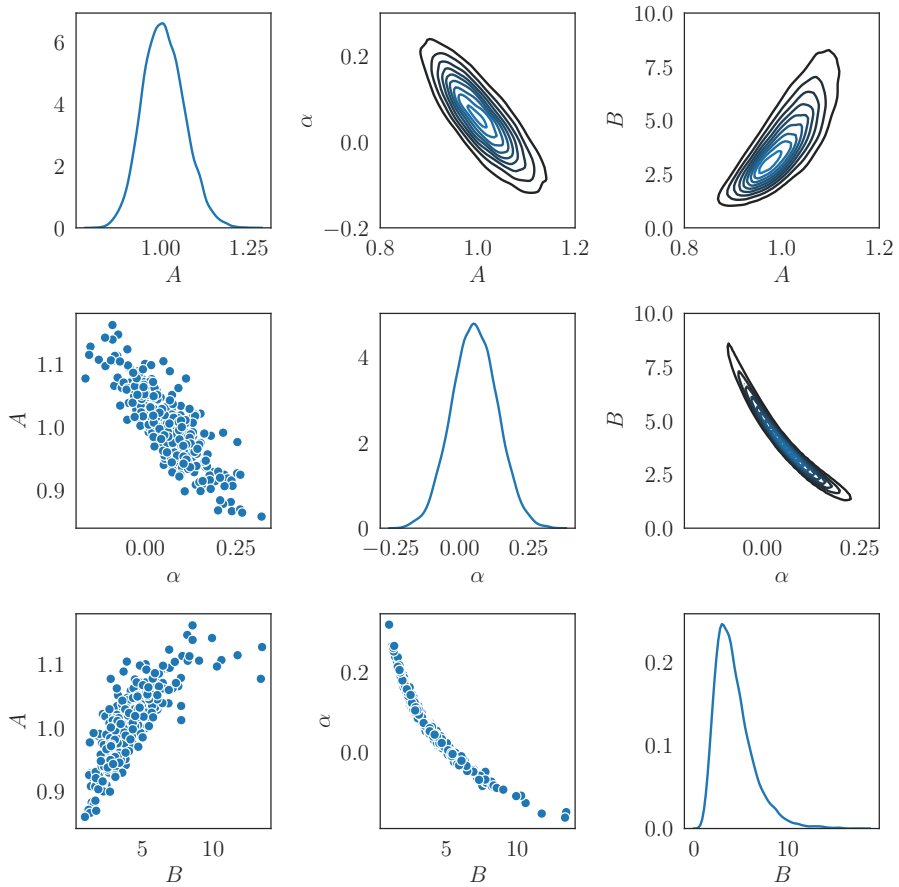
Figure 4.9: Test of a global, Bayesian fit of the transformation parameters A, α and B to auxiliary data. The data set used is from an OCL experiment with the reaction $^{184}\mathrm{W}(\alpha, p)^{187}\mathrm{Re}$. See text for details.
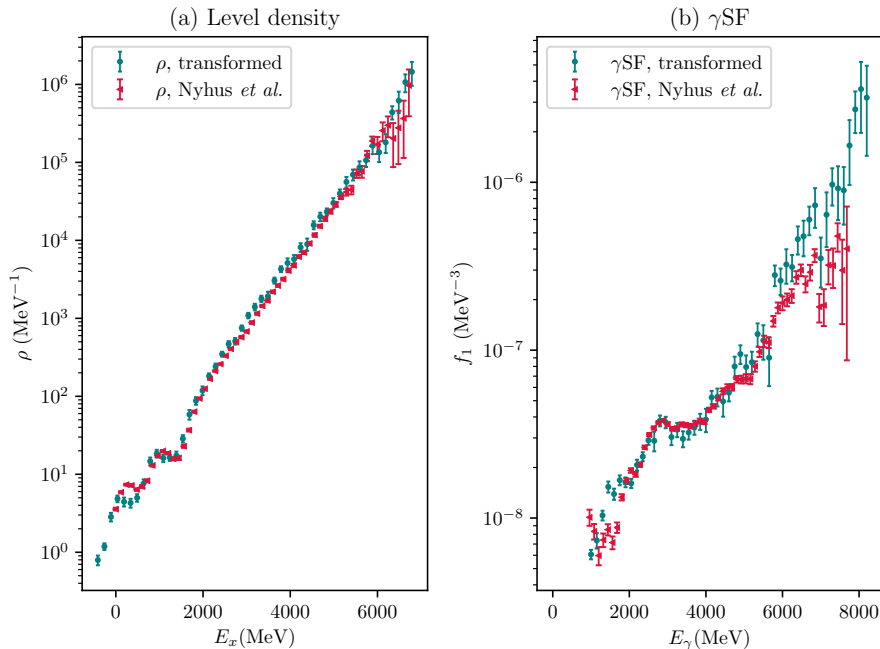
Figure 4.10: Normalised level density and γ-ray strength function of ^{164}Dy, in a comparison between the original analysis of Ref. [133] (red triangles) and a new fit using OMpy (teal circles). The figure is from Ref. [145], included as Paper V in this thesis.

methods involve complex transformations of the starting spectra. Therefore, it is difficult to keep track of the analytical uncertainty in the input spectra all the way to the final result. With the new implementation OMpy, this is amended. We use a Monte Carlo technique to propagate uncertainties by making many copies of the input E_x-E_γ matrix, and perturbing each copy with random noise distributed according to the experimental uncertainty. We assume that the number of counts in each bin of the matrix has a Poisson distribution. By running each member of this *ensemble* of perturbed matrices through the unfolding and first-generation method, we can estimate the standard error in each bin of the first-generation matrix, $\sigma_{P_{\exp}}(E_x, E_\gamma)$, and use that for the χ^2 fit. This is all discussed in detail in Paper V [145]. Figure 4.10 shows a comparison for a data set on ^{164}Dy [113, 133] between the original analysis using the Oslo-method software package [150] and a re-evaluation using OMpy.

The modularity of OMpy also opens up for other possibilities, which will be pursued in the future. For instance, the ensemble propagation technique can be applied to study the systematic uncertainties associated with the unfolding procedure. The response functions used in the unfolding are not perfect, and

there are systematic uncertainties in how well they model the actual response of the detectors. The ensemble propagation technique can be extended to gauge this uncertainty by constructing an ensemble of different response functions. Another refinement which will be considered is to separate the raw E_x-E_γ matrix into signal and background and perturb the two individually. This is required to make the assumption of Poisson distributed counts completely valid.

4.8 The β-Oslo method

I end the chapter with some words on the β-Oslo method. It is a new technique, invented in 2014 in connection with experiments at Michigan State University (MSU). The β-Oslo method is a variation of the Oslo method based on total absorption spectrometry (TAS) [123]. The idea is to obtain the excitation energy by summing all the γ rays emitted by the daughter nucleus following β decay of the parent nucleus. This eliminates the need for an auxiliary detection of the E_x value, and thus opens the possibility for applying the Oslo method to nuclei that cannot be produced via stable targets. Instead, one can produce the nuclei of interest by β decay inside the detector, and observe the β-delayed γ emission. The β-Oslo method has been applied to a number of cases so far using the SuN detector at MSU [168]: ^{76}Ge [123], ^{69}Ni [132] and ^{74}Zn [141], as well as two cases where I have been involved: ^{70}Ni [59] and ^{51}Ti, included in this thesis as Paper I and IV, respectively. A large number of β-Oslo experiments on other nuclei are planned for the near future.

In the β-Oslo method experiments that are part of this thesis, a β^--unstable nucleus is produced, separated and implanted on a double-sided silicon strip detector (DSSD) inside SuN. When it decays by converting a neutron to a proton, it emits an electron that can be detected by the DSSD (along with a neutrino that escapes detection). This provides a tag for the event. The residual nucleus (generally) ends up in an excited state and decays to its ground state by emitting a β-delayed cascade of γ rays, which are detected by SuN. The summing efficiency of SuN varies with γ-ray multiplicity and initial excitation energy, and is on average 25-30 % [59].

While allowing studies outside the reach of the standard Oslo method, the β-Oslo method also poses some new challenges. The first concerns spin population. When excited states in a nucleus are populated mainly via Gamow-Teller β decay, the range of available states are governed by the associated selection rules, which dictate that the available final states for a decay differ from the decaying state by at most one unit of angular momentum, $\Delta J_{i,j} = 0, \pm1$ [24]. The parity does not change. This means that the available spin range of the initial excitation energy levels in the nucleus under study, $g_{\mathrm{pop}}(E_x, J_i, \pi_i)$, has a width of only three spin units, and only one parity. This is, at least at high excitation energy, significantly different from the intrinsic spin distribution of the nucleus. Assuming that the subsequent γ decays are dominantly dipole, the electromagnetic selection rules allow one further unit of spin change, as well as a parity flip, bringing the available spin range after one dipole transition
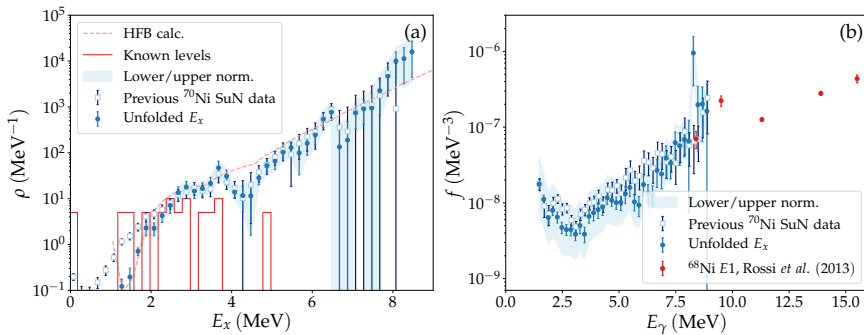
Figure 4.11: Experimental level density (a) and γ-ray strength function (b) of ^{70}Ni. The blue circles and white squares show the level density extracted with and without E_x unfolding, respectively. The figure is reprinted with permission from Ref. [59], included in this thesis as Paper I.

to $\{J_i - 2, J_i - 1, J_i, J_i + 1, J_i + 2\}$ including both parities. Hence, the spin distribution of β-populated levels has a width of three spin units in one parity, while the distribution after the primary γ decay is five units wide and includes both parities. In principle, this is a violation of the assumptions in the first-generation method, where there should be no difference between a level being populated by the nuclear reaction or by γ decay from a level above. This can lead to artificial holes in the primary γ-ray matrix at high E_x due to oversubtraction of intensity from E_x bins below. This is a problem in the ^{70}Ni analysis presented in Paper I [59], and impairs the quality of the extracted level density at high E_x. In that case, the ^{70}Co parent decays from a 6^- level, populating 5^-, 6^- and 7^- levels in the ^{70}Ni daughter. The subsequent dipole γ decay can then reach final levels with $J \in [4, 8]$ in both parities – a significantly higher available level density.

Futhermore, the restricted spin range even after one dipole decay must be taken into account when normalising to auxiliary data. For ^{70}Ni, a correction factor of 0.47 was used to compensate the difference between the total auxiliary level density at S_n and the selective population in the β-Oslo experiment [169].

4.8.1 The unfolding problem in β-Oslo events

Another important difference from the regular Oslo method is in the unfolding. Since the E_x tag for each event is given by the sum of all the E_γ measurements in the event, the dependence of the E_x-E_γ matrix on detector response effects is much more complicated. In the first analyses performed with the β-Oslo technique, no unfolding was applied to the E_x axis. Then, a separate unfolding along the E_x axis was developed. Figure 4.11a demonstrates how this affected the level density and γ-ray strength function for the case of ^{70}Ni. The most striking difference is in the level density for $E_x < 2$ MeV, where the E_x-

unfolded level density exhibits a much sharper drop below $E_x \sim 2$ MeV. This constitutes an improved agreement with the experimental level structure (red solid curve), because the 0^+ ground state and the first excited 2^+ state should not be populated by the β decay.[8]

However, the problem of β-Oslo unfolding is complicated, interesting and worth a closer inspection. I will now briefly describe work I have done together with Fabio Zeiser to try to develop an improved method for unfolding β-Oslo events. We have written a code to simulate the effect of detector response folding on E_x-E_γ matrices constructed according to the β-Oslo technique, *i.e.*, by calculating E_x for each event as

$$E_x = \sum_{k=1}^{N} E_{\gamma,k} \qquad (4.38)$$

for an event with N γ rays. In the Oslo method, we assume that the detector response folding can be modelled according to Eq. (4.5). In the β-Oslo method, in terms of (E_x, E_γ), the response of the detector is a four-variable probability distribution: Given an event with energies E'_x, E'_γ, the probability that it is detected with energies E_x, E_γ is $P(E_x, E_\gamma | E'_x, E'_\gamma)$. In matrix language, this is a rank-4 response tensor, and the operation of folding becomes

$$F(E_x, E_\gamma) = \sum_{E'_x, E'_\gamma} P(E_x, E_\gamma | E'_x, E'_\gamma) U(E'_x, E'_\gamma). \qquad (4.39)$$

Furthermore, since $E_x = \sum E_\gamma$, the E_x response is *multiplicity dependent*: An event consisting of two γ-rays will not have the same E_x response as an event of four. Also, there is mixture of the different multiplicities – for example, an event with high multiplicity will often get several γ rays in the same detector segment, so that the observed multiplicity is lower than the true multiplicity. Alternatively, some γs may escape detection altogether, giving both a too-low multiplicity and too-low E_x. The observed multiplicity may also be larger than the true multiplicity, if one registers a Compton scattered photon in a different detector segment. All this is to say, the response tensor should probably have at least two additional variables, the multiplicities M' and M, which further increases the dimensionality. This system of equations is too demanding to solve exactly, and approximations or alternative approaches must be pursued instead.

As already mentioned, the approximation that has been used in the ^{70}Ni case of Paper I [59] is to unfold the E_x-E_γ matrix *separately* along the E_γ and E_x axes. This amounts to assuming that the folding probability $P(E'_x, E'_\gamma | E_x, E_\gamma)$ can be factorised as $P(E_x | E'_x) P(E_\gamma | E'_\gamma)$. In the other analyses that have been published so far, no unfolding has been applied to the E_x axis at all.

---

[8]There is a small component of decays from an isomer of tentative spin assignment 3^+ in ^{70}Co that offers a decay path to populate the 2^+ level. The 0^+ ground state should be completely unreachable.

To test the impact of *neglecting E_x unfolding* altogether, we have simulated the folding response in a simple case with two coincident, monochromatic γ rays of energy $E_{\gamma,1} = 1300$ keV, $E_{\gamma,2} = 1700$ keV. We draw 5×10^5 events with Gaussian noise added, and sort them into an E_x-E_γ matrix as shown in Fig. 4.12. The top left panel shows the events without any detector response, and the bottom left panel shows the events after folding them with SuN response functions, as they would appear in the detector. For simplicity, we neglect the possibility of detecting the sum of both γ rays in the same detector segment. We then apply the original Oslo method γ-energy unfolding to the latter, assuming that the E_x bins are independent. The result of this is shown in Fig. 4.12c. It is apparent how the spectra are distorted by the lack of E_x unfolding.

We instead suggest a different tactic to get around the problem of factorising Eq. (4.39). Instead of sorting the events into an E_x-E_γ matrix, we keep the separate $E_{\gamma,i}$ information for each event and sort the events into a multidimensional hypercube $E_{\gamma,1}$-$E_{\gamma,2}$-$\cdots$-$E_{\gamma,N}$. In our simulation, we used $N = 2$, but the problem generalises straightforwardly. The folding equation then becomes

$$F(E_{\gamma,1}, E_{\gamma,2}) = \sum_{E'_{\gamma,1}, E'_{\gamma,2}} P(E_{\gamma,1}|E'_{\gamma,1}) P(E_{\gamma,2}|E'_{\gamma,2}) U(E_{\gamma,1}, E_{\gamma,2}), \qquad (4.40)$$

i.e. the factorisation is built in. The SuN detector has four segments in the centre, giving $N \leq 4$. This means that the unfolding can be carried out as a successive series of one-dimensional unfolding operations. In Fig. 4.13, we show the same simulated data as above, plotted against the E_γ values. The panels show how the successive unfolding puts most of the counts back in their original position. With this method, we are able to reconstruct about 80% of the events into within ± 200 keV of their simultaneous full-energy peak, delineated by the white dotted rectangle in Fig. 4.13d. After unfolding, the hypercube can be transformed into an E_x-E_γ matrix, as shown in Fig. 4.12d.

Our new method is currently undergoing testing and further development. The inclusion of many γ rays introduces issues of sparsity when the events are sorted as a hypercube, which makes the unfolding more challenging. Also, the issue of multiplicity correction needs to be addressed. Still, the tests show promise, and we hope that the method can help improve the β-Oslo technique.
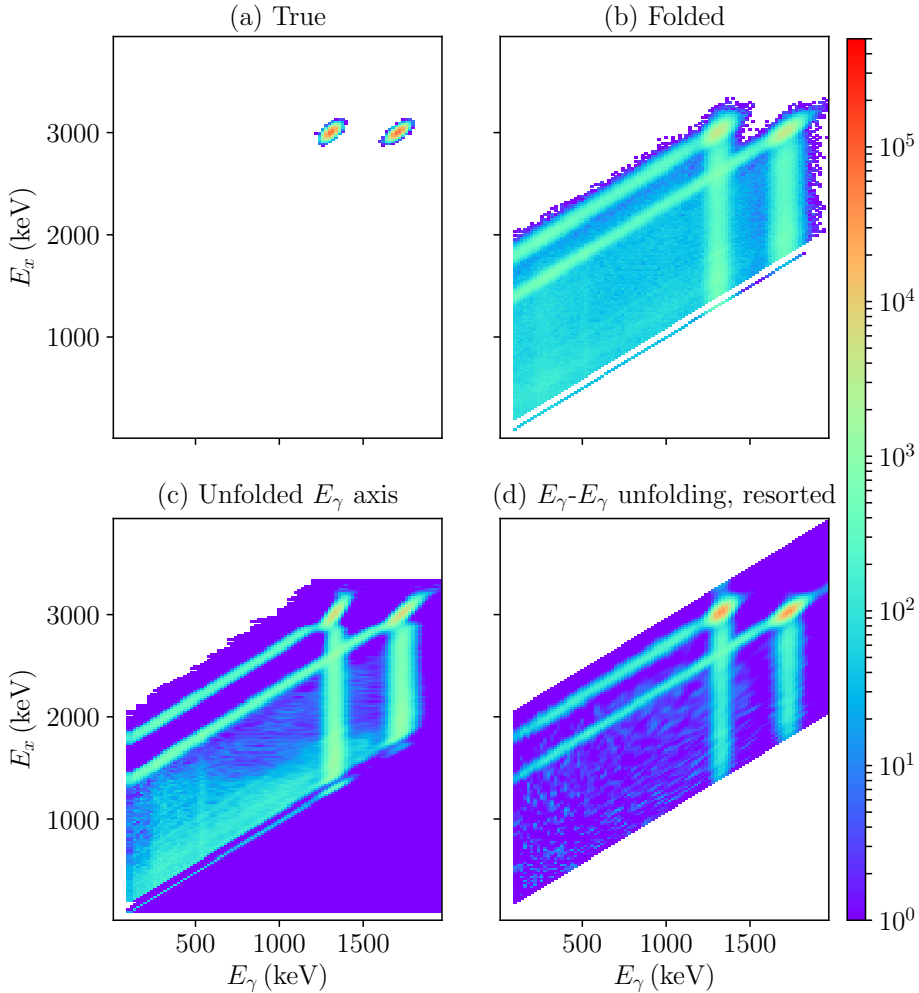
Figure 4.12: E_x-E_γ coincidence matrices of 5×10^5 events with two coincident, monochromatic γ rays of energy $E_{\gamma,1} = 1300$ keV, $E_{\gamma,2} = 1700$ keV being folded by the detector response. The panels show (a) the simulated γ rays before they are folded, (b) the events after detector response folding, (c) the events unfolded along the E_γ axis without taking into account the E_x folding dependence, and (d) the events unfolded with our new suggested method, transformed from $(E_{\gamma,1}, E_{\gamma,2})$ to (E_x, E_γ). See the text for details.
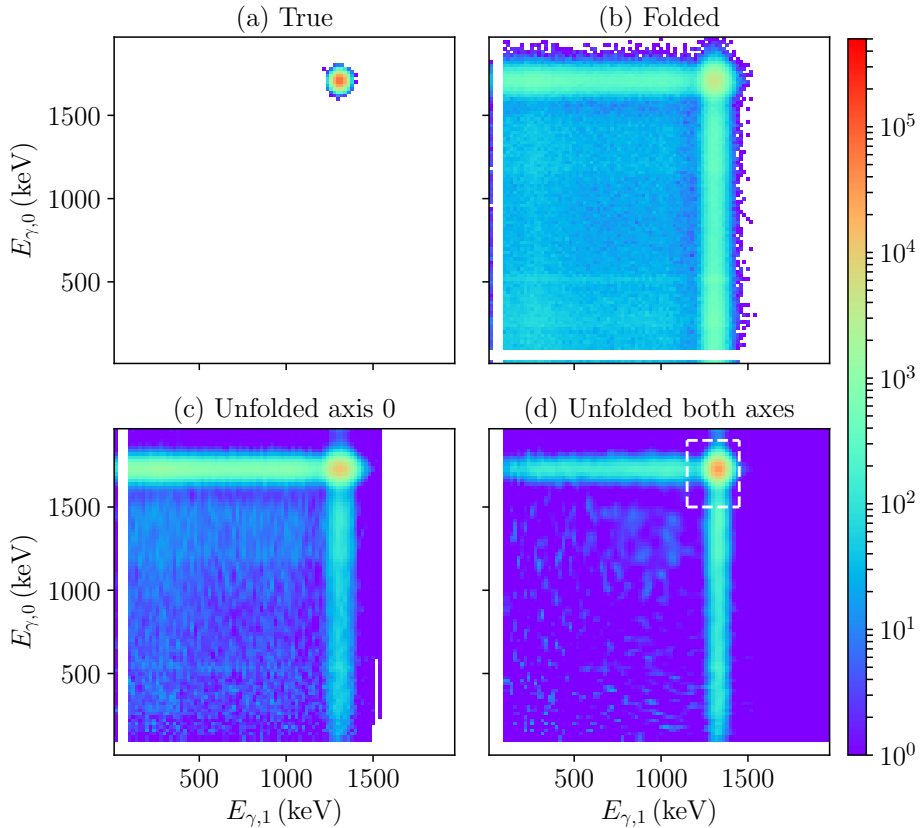
Figure 4.13: $E_{\gamma,1}$-$E_{\gamma,2}$ coincidence matrices of 5×10^5 events with two coincident, monochromatic γ rays of energy $E_{\gamma,1} = 1300$ keV, $E_{\gamma,2} = 1700$ keV. The panels show (a) the simulated γ rays before folding, (b) after folding with detector response, (c) after being unfolded along $E_{\gamma,1}$ and (d) after being subsequently unfolded along $E_{\gamma,2}$. The white dotted lines in panel (d) define a rectangle of ±200 keV around the simultaneous full-energy peak. About 80 % of the counts are reconstructed inside this rectangle after unfolding both axes.

Chapter 5

Summary and outlook

I have approached the topic of nuclear level densities and γ-ray strength functions from both the theoretical and experimental side. In Paper I, the low-energy enhancement is discovered in the neutron-rich nucleus ^{70}Ni. This, as well as the ^{51}Ti experiment of Paper IV, demonstrates the capabilities of the β-Oslo method to reach nuclei outside the scope of the conventional Oslo method. I have performed shell model calculations that agree well with the experimental level densities and γ-ray strength functions, and indicate that the low-energy enhancement in the γ-ray strength function is a robust phenomenon of $M1$ character.

In fact, it is becoming increasingly clear that the low-energy enhancement is a feature general to atomic nuclei at high excitation energy, and that it is likely to be dominated by $M1$ transitions. Through large-scale shell-model calculations on hundreds of nuclei in several mass regions, I have mapped out predictions of the shape of the low-energy enhancement in the γ-ray strength as function of neutron and proton number. The calculations consolidate the concept of the low-energy enhancement from several previous studies into a consistent picture. The shape of the enhancement varies between nuclei, and seems to depend on several factors, notably nuclear mass (or availability of high-l shell-model orbitals near the Fermi surface), and proximity to shell closures (or deformation). Additionally, there seems to be an amplified preference for steep low-energy enhancement in the *shears bands* regions, where protons couple to neutron holes to generate large, transverse magnetic moments [170].

I have also performed calculations on selected nuclei (^{29}Si and ^{44}Sc in Paper II, ^{51}Ti in Paper IV) that include both $E1$ and $M1$ strength functions in the same shell-model framework, using two major shells. These calculations further strengthen the indication that the low-energy enhancement is of $M1$ origin, with an $E1$ component that trails off as E_γ approaches zero. For ^{29}Si, the calculations do not predict a low-energy enhancement, but they still give a flat $M1$ component that dominates at low E_γ.

The distribution of spins remains one of the largest sources of uncertainty in the normalisation procedure of the Oslo method. By decomposing my shell-model calculations of ^{59,60}Ni in Paper III into levels of different spins, we have developed a novel way to constrain the spin distributions for Oslo-method analyses. Here, new innovations that further increase the capabilities of the shell model to tackle large model spaces will be very useful. Notably, reliable spin distributions that discriminate between parities will be vital in low-mass nuclei that can have large parity asymmetry reaching up to high excitation energies. The stochastic level density method of Ref. [35] is a very interesting technique for this purpose.

Experimental results and claims (as, for that matter, theoretical ones) are crucially dependent on proper estimation of uncertainties. Our new implementation of the Oslo method with the uncertainty propagation technique in Paper V is important in this regard, enabling us to present new results with greater confidence. The new code is published open-source, and written to be transparent. Hopefully, this helps other researchers study, adapt, scrutinise and enhance the Oslo method. New developments regarding detector response unfolding, quantification of systematic uncertainties and normalisation will be especially important as the β-Oslo method gains popularity and is applied to even more exotic isotopes.

I think there is good reason to expect that the low-energy enhancement is present, at energies below current experimental thresholds, in $A > 100$ nuclei. However, to discover it will require use of detectors with Compton suppression capabilities, or other methods that give better control of the detector response unfolding. Hopefully, the experimental techniques will become sufficiently refined in the years to come to enable a more detailed discrimination of the shape and magnitude of the low-energy enhancement between nuclei of differing proton and neutron numbers. Then, we can hope to settle the precise dependence of the enhancement on mass, deformation and magnetic moments.

Studies of γ-ray strength functions and their low-energy enhancements is a topic that continues to gain interest. New results, exciting experimental and theoretical advances and novel ideas should be expected in the years to come. It is a big puzzle, and I hope that my small contribution has helped to lay a few pieces in place.

Chapter 6

Papers

I begin this chapter with a brief introduction to each paper, before reprinting them all in full.

Paper 1: Enhanced low-energy γ-decay strength of ^{70}Ni and its robustness within the shell model

The paper presents a β-Oslo analysis of the low-energy γ-ray strength function of ^{70}Ni. This was, at the time of publication, the most neutron-rich nucleus where the low-energy enhancement had been seen. (It was recently succeeded by ^{74}Zn [141]). We present large-scale shell model calculations that demonstrate that the low-energy enhancement can be robustly described as an $M1$ phenomenon. We also present calculations spanning the isotopic chain of nickels, predicting a low-energy enhancement in all of them.

I am the second author of this paper, and corresponding author together with Dr. Larsen. We collaborated closely on writing the paper. My main responsibility was Section IV. I performed all the shell model work, including tuning the CA48MH1g interaction, running all calculations on the supercomputer and converting the results to level densities and γ-ray strength functions. I was also involved in discussions regarding the β-Oslo analysis. Some of the other authors also contributed theoretical calculations, while others helped with the experiment. All authors reviewed the manuscript. The article is published as Ref. [59].

Paper 2: Consolidating the concept of low-energy magnetic dipole decay radiation

The paper presents a theoretical survey of the low-energy enhancement in two different regions of the nuclear chart: The sd and $f_{5/2}pg_{9/2}$ shells. We suggest a measure for the LEE and study its evolution as function of neutron and proton number. We find a systematic dependence on proximity to shell closures, as well as a preference for regions favouring proton-particle-neutron-hole coupling leading to magnetic rotation. These findings consolidate previous theoretical works into a consistent picture. Furthermore, we compile γ-ray strength functions based on discrete, experimental data and demonstrate that they are consistent with shell model calculations and with a low-energy enhancement.

I am first author and the sole corresponding author of this paper. I planned and performed the research presented, and wrote the manuscript. The other authors contributed discussions about the results and interpretations, and they reviewed the manuscript. The article is published as Ref. [27].

Paper 3: Experimental γ-decay strength in ^{59,60}Ni compared with microscopic calculations

The paper presents measurements of γ-ray strength functions and level densities for ^{59,60}Ni. Oslo-method analyses are used to obtain the γSF below the neutron separation energy, complemented by (γ, n) measurements above neutron threshold. The analysis reveals the presence of a strong low-energy enhancement. A special challenge in this paper was the fact that the nuclei are quite light. This makes the usual models for spin distribution parameters more uncertain than is the case for heavier nuclei. To amend this, we wanted to estimate spin distributions based on the shell model calculations. By making histograms of the spin distributions in different excitation energy regions, we were able to make a series of fits to the spin distribution function parametrized by the spin-cutoff parameter σ (Fig. 3), and hence give a prediction for the evolution of σ based on microscopic calculations. To obtain complete spin distributions up to S_n, shown in Fig. 4 it was necessary to calculate as many as 300 levels of each spin. Based on the calculations, we also extracted the total level density and the $M1$ γ-ray strength function, shown in Figs. 9, 10 and 11.

I am third author and one of the main authors on this paper. I was mainly responsible for the shell model calculations and the extraction of spin distributions, level densities and γ-ray strength functions. In addition to the calculations, I was involved in the development of the unfolding technique for (γ, n) cross sections described in Section IV B. I also contributed to the writing of the manuscript. The paper has been submitted to Physical Review C and is currently in review. A preprint is available from Ref. [54].

Paper 4: Benchmarking the extraction of statistical neutron capture cross sections on short-lived nuclei for applications using the β-Oslo method

The paper presents measurements of the level density and γ-ray strength function of ^{51}Ti using both the Oslo and β-Oslo methods, using a ^{50}Ti$(d, p)^{51}$Ti and ^{51}Sc$(\beta^-)^{51}$Ti reaction, respectively. The main aim of the paper is to compare a direct measurement of neutron capture cross sections – in this case for ^{50}Ti – to that inferred indirectly by the Oslo- or β-Oslo methods. It is shown that the agreement is good. The paper also demonstrates the close agreement between the level density and γSF between the Oslo and β-Oslo methods.

I am seventh author and one of the main authors on this paper. I was mainly responsible for the shell-model calculations of the level density and $M1+E1$ γ-ray strength function. I also contributed to the writing of the manuscript. The paper has been submitted to Physical Review C and is currently in review. The version presented here is in preparation to be resubmitted to the journal after taking the referee's comments into account.

Paper 5: A new software implementation of the Oslo method with complete uncertainty propagation

The paper presents a complete re-implementation and extension of the Oslo method analysis codes, in a Python package that we have called OMpy. It enables propagation of uncertainties from the raw spectra all the way through to the extracted level density and γ-ray strength function, using a Monte Carlo technique. We apply OMpy to several data sets that have previously been published, and compare to the results of the original analyses. We thus verify that the new implementation works as intended, and demonstrate its capabilities for giving a more reliable uncertainty quantification.

I am first author and the sole corresponding author on this paper. I had the idea to do uncertainty propagation on the Oslo method by a reimplementation in Python, and developed the code. Fabio Zeiser contributed the module to fit level density and transmission coefficient to the primary matrix. Erlend Lima has worked on code structure and quality assurance, *e.g.* by implementing unit testing to root out errors. I performed the re-analyses of the data sets presented and wrote the manuscript. The other authors provided input to the code development and/or re-analyses. All authors reviewed the manuscript. The paper will be submitted to Nuclear Instruments and Methods in Physics Research Section A. A preprint is available from Ref. [145].

Paper I: Enhanced low-energy γ-decay strength of ^{70}Ni and its robustness within the shell model

Enhanced low-energy γ-decay strength of ^{70}Ni and its robustness within the shell model

A. C. Larsen,[1,*] J. E. Midtbø,[1,†] M. Guttormsen,[1] T. Renstrøm,[1] S. N. Liddick,[2,3] A. Spyrou,[2,4,5] S. Karampagia,[2]
B. A. Brown,[2,4] O. Achakovskiy,[6] S. Kamerdzhiev,[7] D. L. Bleuel,[8] A. Couture,[9] L. Crespo Campo,[1] B. P. Crider,[2,10]
A. C. Dombos,[2,4,5] R. Lewis,[2,3] S. Mosby,[9] F. Naqvi,[2] G. Perdikakis,[2,5,11] C. J. Prokop,[2] S. J. Quinn,[2,4,5] and S. Siem[1]

[1]*Department of Physics, University of Oslo, N-0316 Oslo, Norway*
[2]*National Superconducting Cyclotron Laboratory, Michigan State University, East Lansing, Michigan 48824, USA*
[3]*Department of Chemistry, Michigan State University, East Lansing, Michigan 48824, USA*
[4]*Department of Physics and Astronomy, Michigan State University, East Lansing, Michigan 48824, USA*
[5]*Joint Institute for Nuclear Astrophysics, Michigan State University, East Lansing, Michigan 48824, USA*
[6]*Institute of Physics and Power Engineering, 249033 Obninsk, Russia*
[7]*National Research Centre Kurchatov Institute, 123182 Moscow, Russia*
[8]*Lawrence Livermore National Laboratory, Livermore, California 94551, USA*
[9]*Los Alamos Neutron Science Center, Los Alamos National Laboratory, Los Alamos, New Mexico 87545, USA*
[10]*Department of Physics and Astronomy, Mississippi State University, Mississippi State, Mississippi 39762, USA*
[11]*Department of Physics, Central Michigan University, Mount Pleasant, Michigan, 48859, USA*

Neutron-capture reactions on very neutron-rich nuclei are essential for heavy-element nucleosynthesis through the rapid neutron-capture process, now shown to take place in neutron-star merger events. For these exotic nuclei, radiative neutron capture is extremely sensitive to their γ-emission probability at very low γ energies. In this work, we present measurements of the γ-decay strength of ^{70}Ni over the wide range $1.3 \leqslant E_\gamma \leqslant 8$ MeV. A significant enhancement is found in the γ-decay strength for transitions with $E_\gamma < 3$ MeV. At present, this is the most neutron-rich nucleus displaying this feature, proving that this phenomenon is not restricted to stable nuclei. We have performed $E1$-strength calculations within the quasiparticle time-blocking approximation, which describe our data above $E_\gamma \simeq 5$ MeV very well. Moreover, large-scale shell-model calculations indicate an $M1$ nature of the low-energy γ strength. This turns out to be remarkably robust with respect to the choice of interaction, truncation, and model space, and we predict its presence in the whole isotopic chain, in particular the neutron-rich ^{72,74,76}Ni.

DOI: 10.1103/PhysRevC.97.054329

I. INTRODUCTION

One of the most intriguing and longstanding scientific quests is the understanding of the fundamental building blocks in nature. Indeed, new paradigms have been established as new and improved measurements have been made available. A striking example is the standard model of particle physics [1], proven to be extremely robust and predictive. On the nuclear scale, significant progress has been made as well, but a unified theory describing all facets of nuclear structure and dynamics for all nuclei is still lacking (see, e.g., Ref. [2]).

A particularly challenging task is to properly describe nuclear properties in the energy regime where the average spacing, D, between the available quantum states is still larger than the width Γ of the state, but so small that conventional spectroscopy is impractical or nearly impossible. This region, generally known as the quasicontinuum, is of particular interest for studying nuclear dynamics such as breaking of nucleon-Cooper pairs [3], as well as γ-decay resonances (see, e.g., Refs. [4–7] and references therein).

In addition to the pure nuclear-structure motivation, the quasicontinuum is of vital importance to properly describe and understand the creation of elements heavier than iron [8,9], which has been identified as one of the "eleven science questions for the new century" [10]. A clear signature of the rapid neutron-capture process (r-process) has finally been observed: gravitational waves from a neutron-star merger event were observed with the Advanced LIGO and Advanced Virgo detectors [11], and electromagnetic counterparts show that the r-process has indeed taken place in this event [12]. Our detailed understanding of the r-process is, however, still largely hampered by the lack of crucial nuclear-physics input, such as masses, β-decay probabilities, and radiative neutron-capture, (n,γ), rates [9].

Two of the needed nuclear properties for understanding nuclear dynamics in the quasicontinuum as well as calculating astrophysical (n,γ) reaction rates are the nuclear level density (NLD) and the γ-strength function (γSF). The former is simply the average number of quantum levels per energy bin as a function of excitation energy, while the latter is a measure of the average, reduced γ-decay probability. The γSF is dominated by the $E1$ giant dipole resonance (GDR) (e.g., Refs. [13,14]).

In recent years, an unexpected enhancement in the γSF at low γ energies ($E_\gamma < 3$–4 MeV) has been observed in many
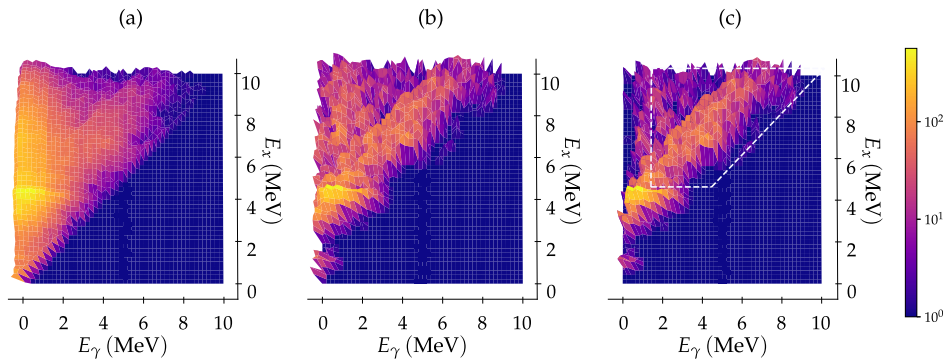
FIG. 1. (a) ^{70}Ni raw γ spectra versus E_x; (b) unfolded γ spectra corrected for the SuN response functions for both E_γ and E_x; (c) distribution of primary γ rays for each E_x bin. The dashed lines show the region used for the analysis. The pixels are 200 keV wide.

fp-shell and medium-mass nuclei (e.g., Refs. [15−19]), with $^{138−140}$La [20,21] and ^{151,153}Sm [22] being the heaviest so far. The multipolarity of this low-energy enhancement, referred to as the upbend in the following, has been experimentally verified to be of dipole type [16,22,23]. However, theoretical attempts to describe the upbend differ on the underlying mechanism and electromagnetic character. The authors of Ref. [24] find an enhancement in the theoretical $E1$ strength, while shell-model approaches [25–27] demonstrate a large low-energy $M1$ enhancement at high excitation energies. Shell-model calculations including both $E1$ and $M1$ components confirm the $M1$ upbend, but also predict the $E1$ γSF to be constant for low energies [28]. A recent experiment on ^{56}Fe, although hampered by limited statistics, indicates that the low-energy enhancement could be a mix of both components, with a small magnetic bias between 1.5 and 2 MeV [29].

Turning to the r-process, the presence of an upbend could increase the astrophysical (n,γ) reaction rates up to $\sim$2 orders of magnitude for very neutron-rich nuclei [30]. Prompt neutron-star merger ejecta correspond to a cold and neutron-rich r-process where an (n,γ)-(γ,n) equilibrium will never be established [9,31]. Hence, (n,γ) rates will have a significant impact on the r-process reaction flow and final abundance distribution. It is therefore crucial to understand the nature of this upbend and search for its presence in nuclei far from stability.

In this paper, we present NLD and γSF measurements of the neutron-rich nucleus ^{70}Ni, using the newly developed β-Oslo method [32,33]. Furthermore, we have calculated the $E1$ strength within the quasiparticle time-blocking approximation (QTBA), and performed large-scale shell-model (SM) calculations for a wide range of effective interactions and model spaces, exploring the $M1$ strength within this framework. We find that the upbend is indeed explained by the shell-model calculations, and we predict its presence in the whole isotopic chain, in particular the neutron-rich ^{72,74,76}Ni.

II. EXPERIMENTAL DETAILS AND DATA ANALYSIS

The experiment has already been described in Refs. [33–35]; a brief summary is given in the following. The

experiment was conducted at the National Superconducting Cyclotron Laboratory, Michigan State University, where ^{70}Co fragments were produced from a primary beam of ^{86}Kr with energy 140 MeV/A impinging on a $\approx$400 mg/cm^2 Be target and selected with the A1900 fragment separator [36]. The fragments were implanted in a double-sided silicon strip detector (DSSD) of 1-mm thickness mounted in the center of the Summing NaI (SuN) total absorption spectrometer [37]. SuN is a large-volume barrel consisting of eight optically isolated segments, providing information on the individual γ rays, while the sum of all detected γ rays gives the initial excitation energy of the daughter nucleus. Coincidences between β^- particles and the fragment were determined by the DSSD using the implantation and β-decay pixel positions in the DSSD and absolute times of the signals. The γ rays measured with SuN were gated on the implantation-β-decay events to obtain the γ-ray spectra of the daughter nucleus. The summing efficiency of SuN varies with γ multiplicity and initial excitation energy, and is, on average, $\approx$25–30 %.

The individual γ-ray spectra versus the summed γ-ray energies (i.e., initial excitation energy E_x) of ^{70}Ni are shown in Fig. 1(a); the total number of counts are about 72000. The γ spectra were unfolded along the E_γ axis with the technique described in Ref. [38] using SuN response functions generated with GEANT4 [39,40] simulations of the full setup. Furthermore, due to the possibility of incomplete summing and a high-energy tail induced by electrons from the β decay (Q_β = 12.3 MeV), we have also developed an unfolding technique for the summed γ rays. This technique is based on the one in Ref. [38] and will be presented thoroughly in a forthcoming article [41]. The resulting unfolded matrix is shown in Fig. 1(b).

After unfolding, the distribution of primary γ rays for each 200-keV E_x bin was extracted by an iterative subtraction technique described in detail in Refs. [42,43]. The basic principle behind this technique is that, for a given excitation-energy bin E_j, the distribution of the first-emitted γ rays (i.e., branchings) is determined by subtracting the γ-ray spectra from the lower excitation-energy bins $E_{i<j}$. This is true if, for a given E_x bin, approximately the same spin distribution is populated directly from the β decay and by the γ decay into this bin from above.
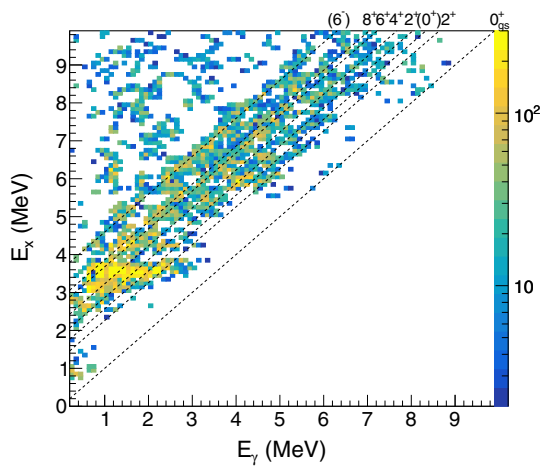
FIG. 2. Matrix of primary γ rays as a function of excitation energy. The dashed lines show the direct decay to the low-energy levels marked with their spin/parity assignment (see text). The bin width is 100 keV both on the γ-ray and E_x axis.

Previous experiments have shown that the ground-state spin/parity of ^{70}Co is $(6^-, 7^-)$ [44,45]. Assuming a spin/parity of 6^-, the β decay will mainly populate levels with spin/parity $5^-, 6^-, 7^-$ in the initial E_x bins through Gamow-Teller transitions. With one dipole γ transition either of electric or magnetic type, the spins populated in the underlying bins are $J = 4$–8 (both parities). On the other hand, if the ^{70}Co ground state has spin/parity 7^-, the initial levels of ^{70}Ni will have spin/parity $6^-, 7^-, 8^-$, and the final levels following one dipole transition will be $J = 5 - 9$. Further, although the timing requirements in the data analysis strongly favors population in ^{70}Ni from the short-lived ≈ 100-ms $(6^-, 7^-)$ level in ^{70}Co, a small contribution from the longer-lived ≈ 500-ms (3^+) level could be present. We also note that in a recent study of the decay chain ^{70}Fe $\rightarrow$ ^{70}Co $\rightarrow$ ^{70}Ni by Morales *et al.* [46], it is suggested that the spin/parity of the longer-lived level could be $(1^+, 2^+)$.

In Fig. 2, we display the matrix of primary γ rays for each excitation-energy bin, where the decay to some of the low-energy levels is indicated with the dashed lines. It is obvious that there is no direct decay to the ground state or to the (0^+) state at 1567 keV [50], as can be expected from an initial spin population of $J > 1$. Thus, it is doubtful that the long-lived level in ^{70}Co is (1^+) as indicated as a possibility in Ref. [46]. However, our data are fully consistent with both the suggested (2^+) [46] and the (3^+) [44,50] assignments. We will in the following use $(2^+, 3^+)$ for the spin/parity assignment of this level. Further, we observe some direct γ decay to the second 2^+ level at 1866 keV, as well as a much weaker direct γ decay to the first 2^+ level at 1259 keV. This indicates that even though the β decay from the ^{70}Co $(6^-, 7^-)$ level is the dominant component, there is also a weaker contribution from the $(2^+, 3^+)$ long-lived state in our data. By inspection of the decay curve, we find that the $(2^+, 3^+)$ contribution is indeed small, of the order of 5–10 %.
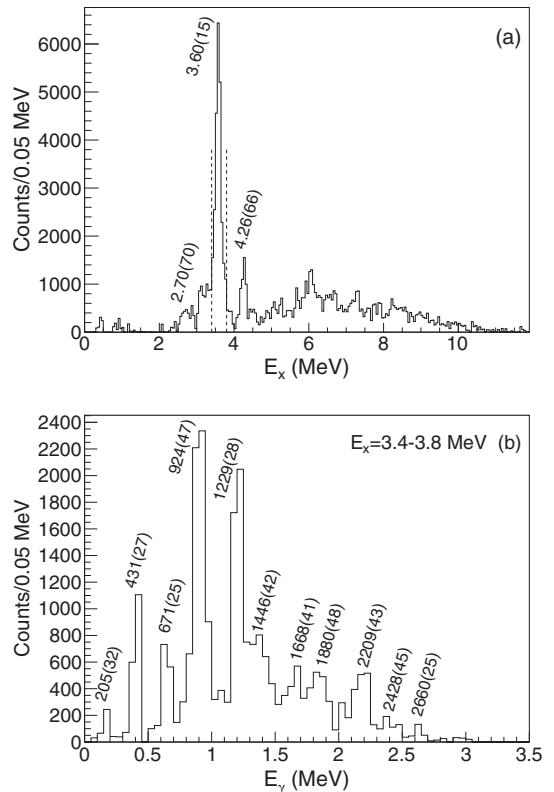
FIG. 3. Projections of the unfolded E_x-E_γ matrix onto (a) the E_x axis, and (b) the E_γ axis for a gate on $E_x = 3.4$–3.8 MeV (dashed lines in the top panel). Transitions are labeled with their γ-ray energies in keV.

Moreover, we observe direct γ decay to the 4^+ level at $E_x = 2229$ keV, which could be reached through $E1$ transitions from 5^- levels, or by $M1$ transitions from 3^+ and 4^+ levels populated from the long-lived $(2^+, 3^+)$ state in ^{70}Co. As the strongest decay to the 4^+ level is seen at $E_x \approx 5.4$ and 6.0 MeV, one would expect $E1$ dominance at such high excitation energies, which is further supported by our calculations presented in Sec. IV. Hence, we find that ^{70}Co most likely has spin/parity 6^- in its ground state, although the 7^- assignment cannot be completely ruled out.

In Fig. 3(a) we show the projection of the unfolded γ-ray matrix onto the excitation-energy axis. This spectrum represents the distribution of level population in ^{70}Ni through β decay of ^{70}Co, and effectively demonstrates that there is no direct population of levels below $E_x \approx 2.5$ MeV. This proves that there is no direct feeding from the $(2^+, 3^+)$ level to the low-lying levels. Further, in Fig. 3(b), we have projected the unfolded γ-ray matrix onto the γ-energy axis, showing all transitions in the γ-decay cascades for an excitation-energy gate of $E_x = 3.4$–3.8 MeV. This gate includes the cascades from the strongly populated (6^-) level at 3592 keV stemming
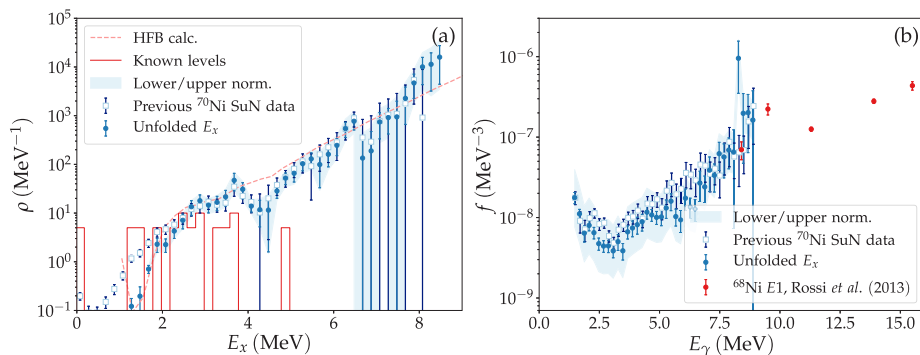
FIG. 4. (a) Extracted NLD for ^{70}Ni from the analysis in Ref. [33] (open squares) and the present E_x-unfolded SuN data (blue points) with upper/lower limits (blue shaded area) and the HFB+c calculations used for normalization (dashed line). (b) Extracted γSF for ^{70}Ni. The data of Rossi *et al.* [52] on ^{68}Ni (red points) are used for normalization.

from the $(6^-, 7^-)$ ^{70}Co ground state, as well as a contribution from the 3510-keV level populated via the $(2^+, 3^+)$ long-lived state. We clearly see strong lines that can be identified (within their uncertainties) to known decay cascades of the $(6^-)$ level [50], but in addition we see weaker transitions of higher γ-ray energies, which are likely originating from the level at 3510 keV populated from the $(2^+, 3^+)$ level.

For the following analysis and comparison with the theoretical calculations, we would like to stress that there is no major change in the conclusions drawn if the (7^-) spin/parity assignment turns out to be the correct one. Further, the contribution from the $(2^+, 3^+)$ level in ^{70}Co is quite small compared to the $(6^-, 7^-)$ one, as demonstrated by the dominance of decay to higher-spin levels in Figs. 2 and 3(b). However, the very strong direct population of the (6^-) level at 3592 keV and the nonpopulation of lower-lying levels could cause problems in the subtraction technique to obtain the primary γ-ray spectra. Further, considering that the initial levels are dominantly populated from the $(6^-, 7^-)$ level we will expect, on average, to subtract somewhat too much of γ rays below ≈ 3 MeV, as the underlying E_x bins will contain γ rays from a broader spin range than what is populated directly through the β decay. Indeed, this is also what we observe in Figs. 1(c) and 2: the higher-energy primary γ rays are not much affected as they are dominantly primary transitions, but we clearly see that there is a region for $E_x \approx 7$–9 MeV where there are few low-energy γ rays. This will lead to a poor estimate of the NLD at high excitation energies, but will not hamper the extraction of the γSF.

III. RESULTS

Having the distributions of primary γ spectra on hand for each excitation-energy bin, we extracted the NLD and γ-transmission coefficient for ^{70}Ni using the least χ^2 method described in Ref. [47]. The main principle of this method is to fit all data points in the selected region of the two-dimensional landscape of primary γ rays with two functions; i.e., the matrix of primary γ rays $P(E_\gamma, E_x)$, normalized for each E_x so that $\sum_{E_\gamma = 0}^{E_x} P(E_\gamma, E_x) = 1$, can be described with the

product $\rho(E_f) \cdot \mathcal{T}(E_\gamma)$ for the final excitation energy $E_f = E_x - E_\gamma$. Here, $\rho(E_f)$ is the NLD and $\mathcal{T}$ is the γ transmission coefficient; the γSF for dipole strength, $f(E_\gamma)$, is derived from $\mathcal{T}$ through $f(E_\gamma) = \mathcal{T}(E_\gamma)/2\pi E_\gamma^3$. Note that there are many more data points in the selected region than fit parameters; the simultaneous fit is thus providing a unique solution of the functional form of the NLD and γSF.

The extracted NLD and γSF functions are normalized as described in Ref. [33]; for the NLD, we make use of known, discrete levels of ^{70}Ni taken from Refs. [48–50]. and Hartree-Fock-Bogoliubov plus combinatorial (HFB-c) calculations taken from Ref. [51] using an E_x shift $\delta = -0.6, -0.8, -1.0$ MeV. With these shifts we reproduce the appearance of the first negative-parity level within ≈ 300 keV. The normalized NLD is displayed in the left panel of Fig. 4. The γSF is normalized to the recently measured $E1$ strength above the neutron threshold of ^{68}Ni by Rossi *et al.* [52] and shown in the right panel of Fig. 4.

We observe that the present NLD displays a steeper slope at $E_x \approx 1.5$–2 MeV than previously due to the unfolding of the E_x axis, thus achieving an excellent agreement with the discrete levels for $E_x \approx 2$–3 MeV. Also, the γSF clearly displays an upbend consistent with the findings in iron isotopes [15,16] and ^{60,64,65,69}Ni [35,53–55]. This gives support to the hypothesis that the upbend is a general feature, and is not restricted to (near-)stable nuclei. Moreover, although rather scarce statistics at the very highest γ energies, our data indicate an increase in strength in the $E_\gamma \approx 8$–9 MeV region. This feature is consistent with the pygmy dipole strength found in ^{68}Ni [52,56]. Hence, our data prove the existence of the upbend in ^{70}Ni, and give a hint to the presence of a pygmy dipole resonance.

IV. THEORETICAL CALCULATIONS AND COMPARISON WITH DATA

The high-energy part of the γSF ($E_\gamma > 4$ MeV) is expected to be dominated by the $E1$ tail of the GDR. To describe the GDR part, we have performed $E1$-strength calculations based on the self-consistent extended version of the theory of finite Fermi systems (ETFFS) within the quasiparticle time-

blocking approximation (QTBA) [57–60] using the BSk17 Skyrme force [61]. The advantage of this approach is that it includes self-consistently the quasiparticle random phase approximation (one-particle-one-hole excitations on the ground state), phonon-coupling effects, and a discretized form of the single-particle continuum spectrum. The Skyrme force is used to calculate the mean-field, effective nucleon-nucleon interaction and phonon properties [59]. We emphasize that phonon-coupling effects are crucial to obtain good agreement with data.[59,60]

The resulting $E1$ strength is shown in Fig. 7. The agreement with the present data for $E_\gamma \approx 5$–9 MeV is excellent, within the experimental error bars. As the QTBA calculation is built on the ground state, this indicates that the average $E1$ strength between excited levels of $J_{\text{initial}} = 5^-, 6^-, 7^-$ and $J_{\text{final}} = 4^+ - 8^+$ is very similar to that of the 1^- levels decaying to the 0^+ ground state, in accordance with the Brink-Axel hypothesis [62–64].

To investigate the $M1$ radiation of ^{70}Ni theoretically, we employ shell-model calculations using the codes KSHELL [65] and NUSHELLX@MSU [66]. To probe the robustness of the results, we use several different effective interactions. For the KSHELL calculations we use JUN45 [67], which contains the orbitals $\pi(p_{3/2}p_{1/2}f_{5/2}g_{9/2})$, $\nu(p_{3/2}p_{1/2}f_{5/2}g_{9/2})$; and two interactions called CA48MH1 and CA48MH2, which include the $\pi f_{7/2}$ but exclude $\pi g_{9/2}$. The CA48MH1 interaction is solely based on many-body perturbation theory (MBPT), i.e., the two-body matrix elements (TBMEs) are not tuned to experimental data [68]. This is the same interaction that was used in a recent study of Fe isotopes [27]. Further, CA48MH2 is derived from CA48MH1 by replacing the neutron-neutron TBMEs with those of JJ44PNA [69], and modifying the diagonal $\pi f_{7/2}$ matrix elements based on the experimental spectrum of ^{54}Fe.

For the NUSHELLX@MSU calculations we use an interaction based on the GXPF1A pf shell interaction [70], extended by

TABLE I. Comparisons of yrast $B(E2)$ strengths (in units of e^2 fm^4) between experiment [72] and SM calculations.

	Exp.	CA48MH1G	CA48MH2	JUN45	CA40FPG
$B(E2; 2_1^+ \to 0_1^+)$	172(28)	154.8	161.4	15.6	35.2
$B(E2; 6_1^+ \to 4_1^+)$	43(1)	120.0	230.7	5.7	24.5
$B(E2; 8_1^+ \to 6_1^+)$	19(4)	21.7	139.7	2.2	9.5

MBPT-generated TBMEs to encompass the full fpg model space for both protons and neutrons. This interaction was also used to predict ^{70}Co β-decay intensities for the present experiment [34]. In the following we will refer to this interaction as CA40FPG.

With the CA48MH model space, the full M-scheme basis size of ^{70}Ni is 1.2×10^9 for each parity, and for CA40FPG it is even larger. For calculations in the CA48MH model space, we therefore restrict the maximum number of excited protons from the $f_{7/2}$ orbital to 2, as has been done in previous studies [25–27], but with no truncations on neutrons. This reduces the basis size to 2×10^7. In the CA40FPG calculations we restrict the model space to the configurations $\pi(f_{7/2}^{8-t_p}(f_{5/2}pg)^{t_p})$, $\nu((fp)^{20-t_n}g_{9/2}^{2+t_n}g_{7/2}^0)$ for $t_p, t_n = 0, 1$. For JUN45, no truncation is applied.

^{70}Ni exhibits a complex low-energy structure. The second excited state is $J^\pi = 0^+$ at $E(0_2^+) = 1567$ keV [50], and calculations indicate it has a very different structure from the ground state [49]. For the CA48MH1 interaction we find good agreement with experiment by increasing the single-particle energy of the $\nu g_{9/2}$ orbital to 1.7 MeV. We will refer to the interaction with this modification as CA48MH1G. This interaction reproduces the low-lying spectrum to within a few hundred keV, including features such as the excited 0_2^+ state and the onset of negative-parity states at $E_x \sim 3$ MeV. As shown in Table I, $B(E2)$ transitions strengths of the yrast
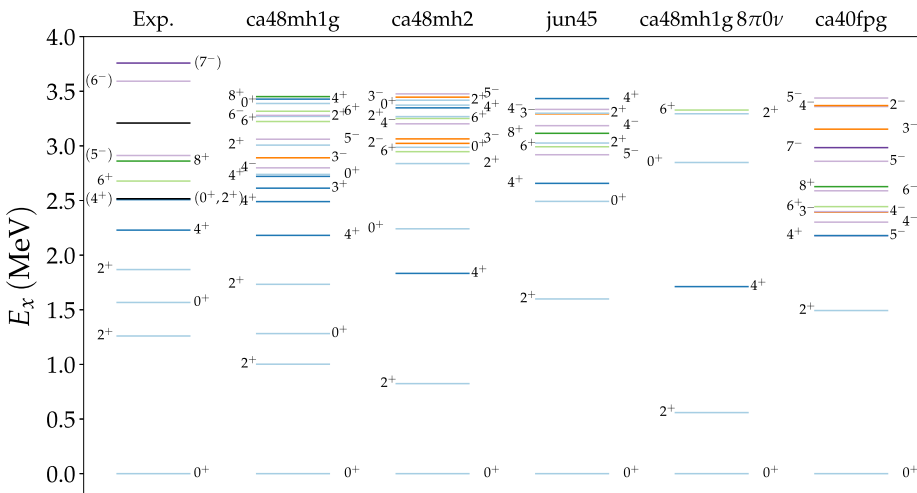

FIG. 5. Comparison of the experimental low-energy structure of ^{70}Ni to calculations with CA48MH1G and JUN45. The experimental data is from [49] except the 0_2^+ state, which is revised according to [50].
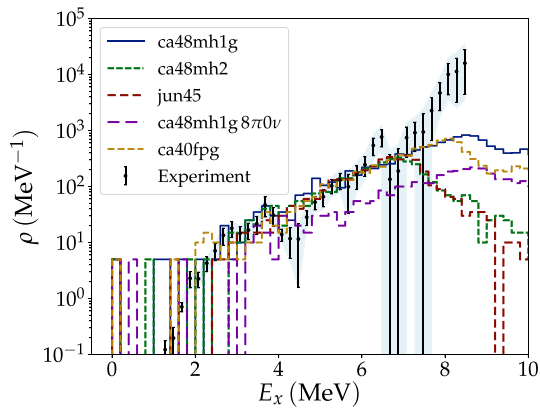
FIG. 6. Calculated shell-model level densities compared to the ^{70}Ni data. The gray band indicates the total experimental uncertainty, systematic, and statistical.

band are also excellently reproduced, with the exception of the $B(E2; 6_1^+ \to 4_1^+)$, which is a factor of 3 too high. The drastic reduction in the experimental $B(E2)$ strength of the yrast band from $(2^+ \to 0^+)$ to $(8^+ \to 6^+)$ is discussed in Ref. [72], and is attributed there to core polarization by the tensor interaction that come into play for the lowest-lying states. The fact that we reproduce this transitional behavior of the $B(E2)$ value supports the applicability of the CA48MH1G interaction to this nucleus, at least for the low-lying levels. Predicted level schemes of the various interactions are shown in Fig. 5.

The CA48MH2 interaction is complementary to CA48MH1G in that it overestimates the 0_2^+ energy. It correctly predicts the $B(E2; 2_1^+ \to 0_1^+)$ value, but fails to catch the transitional behavior along the yrast line. The JUN45 calculation systematically overestimates level energies, and underestimates the $B(E2)$ strengths by an order of magnitude. Both calculations correctly reproduce the onset of negative parity states. The CA40FPG calculation does not reproduce the 0_2^+ band, but this is to be expected due to the significant truncations applied to the model space.
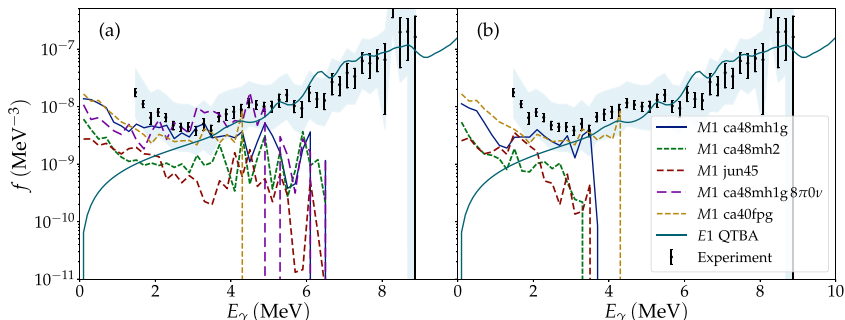
The fact that we have such a diverse ensemble of interactions that capture different features of ^{70}Ni enables us to study the robustness of shell-model calculations up to the quasicontinuum. We also probe the effects of model space truncations, using 0, 1, and 2 proton excitations from $f_{7/2}$ as well as varying neutron truncations.

For each of the interactions, we calculate all states with $J \in [0, 8]$ ($J \in [0, 14]$, in the case of NUSHELLX (KSHELL) for both parities up to $S_n = 7.3$ MeV or above, and $B(M1)$ strengths of all allowed transitions between states. For the calculation of $B(M1)$ values, effective g_s factors of $g_s = 0.9 g_s^{\text{free}}$ have been used. We note that the recommended quenching factor for JUN45 is $g_s = 0.9 g_s^{\text{free}}$, because the core closure goes between spin-orbit partners ($f_{7/2}$–$f_{5/2}$). One could therefore argue that a somewhat larger quenching should be applied also for the ^{48}Ca core interactions. This would serve to reduce the $M1$ strength function somewhat.

We extract the γSF using the relation

$$f_{M1}(E_\gamma, E_i, J_i, \pi_i) = a\langle B(M1)\rangle(E_\gamma, E_i, J_i, \pi_i)\rho(E_i, J_i, \pi_i),$$

where $a = 11.5473 \times 10^{-9}\,\mu_N^{-2}$ MeV^{-2}, and $\rho(E_i, J_i, \pi_i)$ and $\langle B(M1)\rangle$ is the partial level density and the average reduced transition strength, respectively, of states with the given excitation energy, spin, and parity [71]. By the generalized Brink-Axel hypothesis, $f_{XL}(E_\gamma, E_i, J_i, \pi_i) \approx f_{XL}(E_\gamma)$. Hence we obtain $f_{M1}(E_\gamma)$ by averaging over E_i, J, and π. Only E_i, J, π pixels where f_{M1} is nonzero are included in the average. We find that all SM calculations excellently match the experimental NLD up to $E_x \sim 6$ MeV, where they start to fall off because of the limited number of calculated states; see Fig. 6.

Considering transitions from initial states in the region $4.0 \leqslant E_x \leqslant 6.5$ MeV, we obtain the results shown in Fig. 7(a). In Fig. 7(b) we show the $M1$ γSF for transitions originating from 5^-, 6^-, or 7^- levels only, corresponding to the ^{70}Co β decay. The trend of the data for $1.5 \leqslant E_\gamma \leqslant 4.0$ MeV is well reproduced by all calculations, which all display an upbend peaking at $E_\gamma = 0$ MeV. The absolute value of the $M1$ strength is lower than the experimental total strength, although for CA40FPG and CA48MH1G it is within the error band. The QTBA calculations predict a drop of $E1$ strength towards $E_\gamma = 0$. However, the QTBA is not a realistic model for the low-energy

FIG. 7. Calculated γSFs within the shell model (for $4.0 \leqslant E_x \leqslant 6.5$ MeV) and the QTBA (for all E_x) compared with data. The blue shaded band indicates the total experimental uncertainty. In panel (a) all SM $M1$ transitions in the extraction region are included, while in (b) only transitions originating from levels with $J^\pi = 5^-, 6^-$, or 7^- are shown (see text).
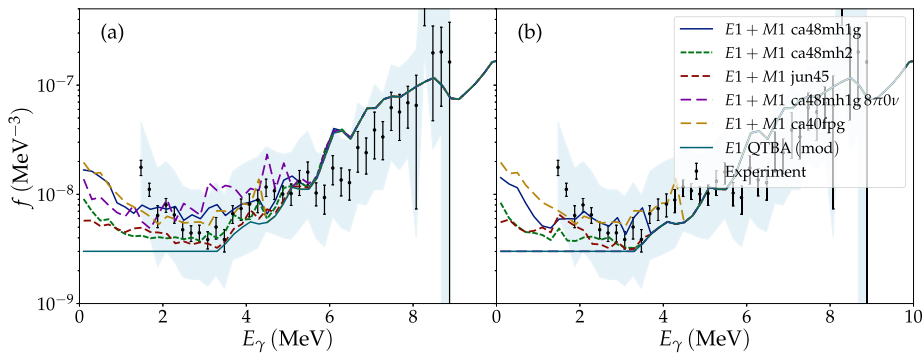
FIG. 8. Sketch of a summed γSF, $f_{tot}(E_\gamma) = f_{E1}^{QTBA(mod)}(E_\gamma) + f_{M1}^{SM}(E_\gamma)$ for the different shell-model calculations. The QTBA calculation has been replaced by a flat $E1$ strength for $E_\gamma < 3.5$ MeV, as suggested by recent shell-model $E1$ calculations [28].

$E1$ strength because it is built on the ground state, so there are no low-E_γ transitions available. A recent $E1$ shell-model study for ^{44}Sc predicts a flat behavior of the γSF for low E_γ [28]. If we assume a similar behavior for ^{70}Ni, this brings the total strength into agreement with experiment, as sketched in Fig. 8.

There is also a discrepancy in the absolute strength between the different calculations, with CA40FPG and CA48MH1G having higher strength than CA48MH2 and JUN45. The highest strength functions seem to be in best agreement with the experimental total strength. The slope is however remarkably similar between all interactions, and consistent with an exponential function $Ae^{-E_\gamma/T}$. For CA48MH1G and CA40FPG we find $T \sim 1$ MeV, while T is somewhat lower (higher) for CA48MH2 (JUN45), respectively.

Considering the β-decay selected $M1$ strength functions, the shape of the γSFs do not change much, indicating that the selectivity of the β decay does not introduce any significant bias in the experimental results. The reason for the abrupt drop in strength at $\sim$4 MeV is the absence of direct transitions to low-lying states because of the $M1$ selection rules.

We do see an upbend of equal slope even with the JUN45 interaction, i.e., without any excited protons, in contrast to previous findings [25]. To investigate this further, we ran the CA48MH1G calculations with a different truncation, locking all neutrons and allowing all protons to excite (labeled $8\pi0\nu$ in Fig. 7). The upbend is present here as well, with approximately

the same slope, but disappears when applying the β-decay spin selection, because the protons-only truncation does not allow for any negative-parity states below S_n. We find that the upbend is a remarkably robust feature for ^{70}Ni within the shell model. During this work, we have explored a large parameter space of shell-model interactions, of which only a subset is shown here. Try as we might, we did not find a single case where the upbend was not present.

Finally, we expanded our theoretical scope and applied the CA48MH1G interaction, with the same proton truncation, to the whole isotopic chain, calculating γ-strength functions for $^{56-69,72,74,76}$Ni. We find an almost identical low-energy behavior of the γ strength across all isotopes, as shown in Fig. 9. The calculations agree with the low-energy behavior of the experimental γ strength for ^{64,65}Ni [54,55], as well as ^{69}Ni [35], the other neutron-rich isotope measured so far with the β-Oslo method. This is an intriguing indication that high intensities for low-energy $M1$ transitions could be a general feature of nuclei at high excitation energy, and could be expected all over the nuclear chart.

V. SUMMARY AND OUTLOOK

In this paper, we have presented level-density and γSF data on ^{70}Ni extracted with the β-Oslo method. The experimental level density is found to be fully compatible with shell-
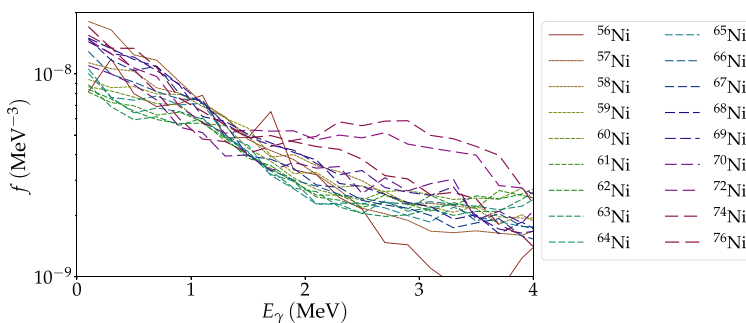

FIG. 9. Calculated $M1$ γ strengths for a wide range of Ni isotopes with the shell model, using the CA48MH1G interaction.

model calculations including both positive and negative parity levels.

Our γSF data are well reproduced by QTBA calculations for transition energies above ≈ 5 MeV. On the other hand, at low transition energies, we find that the γSF displays an upbend; thus ^{70}Ni is the most neutron-rich isotope measured so far showing this feature. The upbend is described within the SM framework as an $M1$ component in the γSF. SM calculations of the $M1$ γSF are also performed for $^{56-69,70,72,74,76}$Ni. The results indicate that the upbend is a general trend for nucleon excitations in the quasicontinuum. Theoretical calculations for an even broader range of model spaces and heavier nuclei are ongoing and new computational methods are in development to investigate this further. The experimental data will be available at http://www.ocl.uio.no/compilation.

[1] R. Oerter, *The Theory of Almost Everything: The Standard Model, the Unsung Triumph of Modern Physics* (Pi Press, New York, 2006).

[2] P. Ring and P. Schuck, *The Nuclear Many-Body Problem*, 3rd ed. (Springer-Verlag, Berlin, 2004).

[3] E. Melby, L. Bergholt, M. Guttormsen, M. Hjorth-Jensen, F. Ingebretsen, J. Messelt, J. Rekstad, A. Schiller, S. Siem, and S. W. Ødegård, Phys. Rev. Lett. **83**, 3150 (1999).

[4] K. Heyde *et al.*, Rev. Mod. Phys. **82**, 2365 (2010).

[5] A. Schiller *et al.*, Phys. Lett. B **633**, 225 (2006).

[6] M. Krtička *et al.*, Phys. Rev. Lett. **92**, 172501 (2004).

[7] D. Savran, T. Aumann, and A. Zilges, Prog. Part. Nuc. Phys. **70**, 210 (2013).

[8] S. Goriely, Phys. Lett. B **436**, 10 (1998).

[9] M. Arnould, S. Goriely, and K. Takahashi, Phys. Rep. **450**, 97 (2007).

[10] *Connecting Quarks with the Cosmos: Eleven Science Questions for the New Century*, Board on Physics and Astronomy (The National Academies Press, Washington, D.C., 2003).

[11] B. P. Abbott *et al.*, Phys. Rev. Lett. **119**, 161101 (2017).

[12] M. R. Drout *et al.*, Science **358**, 1570 (2017).

[13] S. S. Dietrich and B. L. Berman, At. Data Nucl. Data Tables **38**, 199 (1988).

[14] M. N. Harakeh and A. van der Woude, *Giant Resonances* (Oxford University Press, Oxford, 2001).

[15] A. Voinov *et al.*, Phys. Rev. Lett. **93**, 142504 (2004).

[16] A. C. Larsen *et al.*, Phys. Rev. Lett. **111**, 242504 (2013).

[17] M. Guttormsen *et al.*, Phys. Rev. C **71**, 044307 (2005).

[18] M. Wiedeking *et al.*, Phys. Rev. Lett. **108**, 162503 (2012).

[19] T. Renstrøm *et al.*, Phys. Rev. C **93**, 064302 (2016).

[20] B. V. Kheswa *et al.*, Phys. Lett. B **744**, 268 (2015).

[21] B. V. Kheswa *et al.*, Phys. Rev. C **95**, 045805 (2017).

[22] A. Simon *et al.*, Phys. Rev. C **93**, 034303 (2016).

[23] A. C. Larsen *et al.*, J. Phys. G: Nucl. Part. Phys. **44**, 064005 (2017).

[24] E. Litvinova *et al.*, Phys. Rev. C **88**, 031302(R) (2013).

[25] R. Schwengner, S. Frauendorf, and A. C. Larsen, Phys. Rev. Lett. **111**, 232504 (2013).

[26] B. A. Brown and A. C. Larsen, Phys. Rev. Lett. **113**, 252502 (2014).

[27] R. Schwengner, S. Frauendorf, and B. A. Brown, Phys. Rev. Lett. **118**, 092502 (2017).

[28] K. Sieja, Phys. Rev. Lett. **119**, 052502 (2017).

[29] M. D. Jones *et al.*, Phys. Rev. C **97**, 024327 (2018).

[30] A. C. Larsen and S. Goriely, Phys. Rev. C **82**, 014318 (2010).

[31] O. Just, A. Bauswein, R. Ardevol Pulpillo, S. Goriely, H.-T. Janka, Month. Not. Roy. Astron. Soc. **448**, 541 (2015).

[32] A. Spyrou, S. N. Liddick, A. C. Larsen, M. Guttormsen, K. Cooper, A. C. Dombos, D. J. Morrissey, F. Naqvi, G. Perdikakis, S. J. Quinn, T. Renstrøm, J. A. Rodriguez, A. Simon, C. S. Sumithrarachchi, and R. G. T. Zegers, Phys. Rev. Lett. **113**, 232502 (2014).

[33] S. N. Liddick *et al.*, Phys. Rev. Lett. **116**, 242502 (2016).

[34] A. Spyrou *et al.*, Phys. Rev. Lett. **117**, 142701 (2016).

[35] A. Spyrou, A. C. Larsen, S. N. Liddick, F. Naqvi, B. P. Crider, A. C. Dombos, M. Guttormsen, D. L. Bleuel, A. Couture, L. Crespo Campo, R. Lewis, S. Mosby, M. R. Mumpower, G. Perdikakis, C. J. Prokop, S. J. Quinn, T. Renstrøm, S. Siem, and R. Surman, J. Phys. G: Nucl. Part. Phys. **44**, 044002 (2017).

[36] D. J. Morrissey, B. M. Sherrill, M. Steiner, A. Stolz, and I. Wiedenhoever, Nucl. Instrum. Methods Phys. Res. B **204**, 90 (2003).

[37] A. Simon *et al.*, Nucl. Instrum. Methods Phys. Res. A **703**, 16 (2013).

[38] M. Guttormsen, T. S. Tveter, L. Bergholt, F. Ingebretsen, and J. Rekstad, Nucl. Instrum. Methods Phys. Res. A **374**, 371 (1996).

[39] S. Agostinelli *et al.*, Nucl. Instrum. Methods Phys. Res. A **506**, 250 (2003).

[40] J. Allison *et al.*, IEEE Trans. Nucl. Sci. **53**, 270 (2006).

[41] M. Guttormsen, A. C. Larsen, A. Spyrou, and S. N. Liddick (unpublished).

[42] M. Guttormsen, T. Ramsøy, and J. Rekstad, Nucl. Instrum. Methods Phys. Res. A **255**, 518 (1987).

[43] A. C. Larsen *et al.*, Phys. Rev. C **83**, 034315 (2011).

[44] W. F. Mueller *et al.*, Phys. Rev. C **61**, 054308 (2000).

[45] M. Sawicka *et al.*, Phys. Rev. C **68**, 044304 (2003).

[46] A. I. Morales *et al.*, Phys. Lett. B **765**, 328 (2017).

[47] A. Schiller *et al.*, Nucl. Instrum. Methods Phys. Res. A **447**, 498 (2000).

[48] Data extracted using the NNDC On-Line Data Service from the ENSDF database, August 2013; http://www.nndc.bnl.gov/ensdf/

[49] C. J. Chiara *et al.*, Phys. Rev. C **91**, 044309 (2015).

[50] C. J. Prokop *et al.*, Phys. Rev. C **92**, 061302(R) (2015).

[51] S. Goriely, S. Hilaire, and A. J. Koning, Phys. Rev. C **78**, 064307 (2008).

[52] D. M. Rossi *et al.*, Phys. Rev. Lett. **111**, 242503 (2013).

[53] A. V. Voinov *et al.*, Phys. Rev. C **81**, 024319 (2010).

[54] L. Crespo Campo *et al.*, Phys. Rev. C **94**, 044321 (2016).

[55] L. Crespo Campo *et al.*, Phys. Rev. C **96**, 014312 (2017).

[56] O. Wieland *et al.*, Phys. Rev. Lett. **102**, 092502 (2009).

[57] S. Kamerdzhiev, J. Speth, and G. Tertychny, Phys. Rep. **393**, 1 (2004).

[58] V. I. Tselyaev, Phys. Rev. C **75**, 024306 (2007).

[59] O. I. Achakovskiy, S. P. Kamerdzhiev, and V. I. Tselyaev, JETP Letters **104**, 374 (2016).

[60] O. I. Achakovskiy, A. Avdeenkov, S. Goriely, S. P. Kamerdzhiev, and S. Krewald, Phys. Rev. C **91**, 034620 (2015).

[61] S. Goriely, E. Khan, and M. Samyn, Nucl. Phys. A **739**, 331 (2004).

[62] D. M. Brink, doctoral thesis, Oxford University, 1955.

[63] P. Axel, Phys. Rev. **126**, 671 (1962).

[64] M. Guttormsen, A. C. Larsen, A. Görgen, T. Renstrøm, S. Siem, T. G. Tornyi, and G. M. Tveten, Phys. Rev. Lett. **116**, 012502 (2016).

[65] N. Shimizu, arXiv:1310.5431.

[66] B. A. Brown and W. D. M. Rae, Nuclear Data Sheets **120**, 115 (2014).

[67] M. Honma *et al.*, Phys. Rev. C **80**, 064323 (2009).

[68] M. Hjorth-Jensen, T. T. S. Kuo, and E. Osnes, Phys. Rep. **261**, 125 (1995); https://github.com/ManyBodyPhysics/ManybodyCodes/.

[69] A. F. Lisetskiy, B. A. Brown, M. Horoi, and H. Grawe, Phys. Rev. C **70**, 044314 (2004).

[70] M. Honma, B. A. Brown, T. Mizusaki, and T Otsuka, Nucl. Phys. A **704**, 134c (2002).

[71] G. A. Bartholomew, E. D. Earle, A. J. Ferguson, J. W. Knowles, and M. A. Lone, *Advances in Nuclear Physics* (Plenum Press, New York, 1973), Chap. 4, Vol. 7, pp. 229–317.

[72] O. Perru *et al.*, Phys. Rev. Lett. **96**, 232501 (2006).

[73] S. Karampagia, B. A. Brown, and V. Zelevinsky, Phys. Rev. C **95**, 024322 (2017).

[74] S. van der Walt, S. C. Colbert, and G. Varoquaux, Comput. Sci. Eng. **13**, 22 (2011).

[75] J. D. Hunter, Comput. Sci. Eng. **9**, 90 (2007).

Paper II: Consolidating the concept of low-energy magnetic dipole decay radiation

Consolidating the concept of low-energy magnetic dipole decay radiation

J. E. Midtbø,[*] A. C. Larsen, T. Renstrøm, F. L. Bello Garrote, and E. Lima

Department of Physics, University of Oslo, N-0316 Oslo, Norway

We have made a thorough study of the low-energy behavior of the γ-ray strength function within the framework of the shell model. We have performed large-scale calculations spanning isotopic and isotonic chains over several mass regions, considering 283 nuclei in total, with the purpose of studying the systematic behavior of the low-energy enhancement (LEE) for $M1$ transitions. There are clear trends in the calculations: From being nearly absent in the lowest mass region, the LEE becomes steeper and more pronounced as the mass number increases, and for a given mass region it further increases toward shell closures. Moreover, the LEE is found to be steeper in regions near doubly magic nuclei where proton particles couple to neutron holes. These trends enable us to consolidate several previous works on the LEE into a single, consistent concept. We compare the inferred trends to the available experimental data from the Oslo method and find support for the systematic behavior. Lastly, we have compared the calculations to strength functions compiled from discrete, experimental lifetimes and find excellent agreement; the discrete data are consistent with an LEE and indicate that the slope varies as function of mass number.

I. INTRODUCTION

The atomic nucleus is an extremely complicated many-body quantum system [1]. Despite intense scrutiny over many decades, many of its facets are still poorly understood. This is especially true when a significant amount of energy is put into the nuclear system, placing it in a highly excited state. Since the number of accessible quantum levels grows approximately exponentially with energy [2,3], a region of high excitation energy is one where many quantum levels are packed closely together. Questions of fundamental scientific interest include how the quantum-mechanical wave function of such levels is composed and what degree of correlations exist between the levels [4].

Two basic experimental quantities revealing information on the structure of the nuclear wave functions are excitation-energy levels and their corresponding transition strengths. However, when the excitation energy becomes large, it is experimentally difficult to separate individual levels and transitions, and one instead works with average quantities, such as the energy *level density* and γ-ray *strength function*. Our focus in this article is on the strength function, more specifically on the $M1$ component. Evidence for an increasing number of nuclei shows that the γ-ray strength function exhibits an enhancement toward zero γ-ray energy (e.g., Refs. [5,6]). This low-energy enhancement (LEE) has been shown to be of dipole order [7–10]. However, its electromagnetic character is, so far, experimentally undetermined, although recent measurements indicate a small bias toward $M1$ transitions [10].

The level density and γ-ray strength function have an important application in calculations of (n, γ) capture cross

sections (e.g., Ref. [11]). Radiative neutron capture is responsible for the synthesis of most elements heavier than iron, mainly through the slow (s) and rapid (r) neutron-capture processes. The latter process involves neutron-rich nuclei far from stability, close to the neutron drip line. While we are still far from a complete understanding of the r process, which has been singled out as one of the eleven most important science questions for the 21st century [12], huge strides were made recently with the discovery of a neutron-star merger event which seemingly produced r-process elements [13–15]. In such a neutron-rich, low-entropy environment, an (n, γ)-(γ, n) equilibrium cannot be maintained at all times [11,16,17]. Thus, (n, γ) reaction rates become important not only at freeze-out but also for the nucleosynthesis at earlier stages. It has also been shown that the presence of an LEE in the γ-ray strength function can impact the (n, γ) cross sections by orders of magnitude, especially for neutron-rich nuclei [18]. Hence, it is important to obtain an understanding of the prevalence and properties of the LEE.

II. THE HISTORY OF THE LOW-ENERGY ENHANCEMENT

In Fig. 1, we have charted the nuclei that have been studied using the Oslo or β-Oslo methods and indicated whether the experiment saw a low-energy enhancement. It must be stressed that experimental limitations make it difficult to extract the very low-E_γ strength function using the $(\beta$-)Oslo method. This is mainly due to the uncertainties introduced by unfolding of the Compton-scattering events, which induce large uncertainties the low-γ energy spectrum at high excitation energies. Typically, the lower limit on E_γ is set at about 1.5 MeV. An exception is ^{151,153}Sm [8], where Compton suppression allowed extraction all the way down to $E_\gamma =$

---

*[*]j.e.midtbø@fys.uio.no
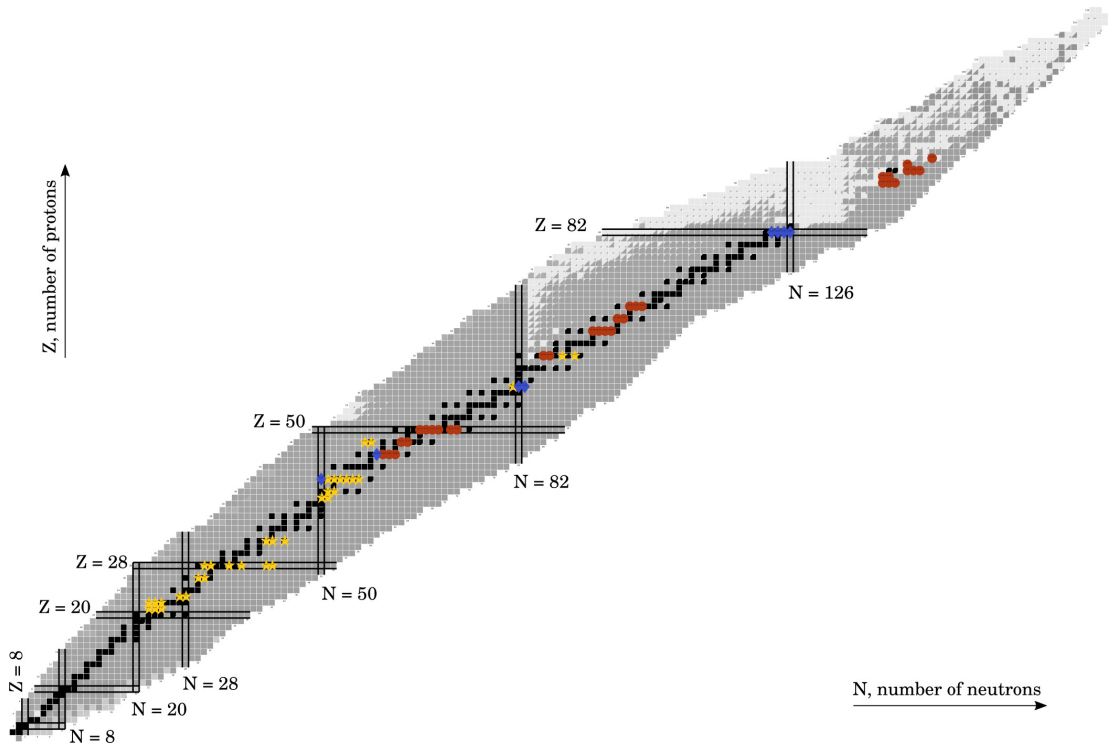
FIG. 1. Map detailing where an LEE has been seen using the Oslo method. Yellow stars indicate yes; red circles no. Blue diamonds denote cases where it is difficult to say whether there is an LEE or not. Note that a negative result cannot rule out the presence of an LEE at lower E_γ energies than was experimentally accessible (see text for more details). The nuclear chart is made using Ref. [19], while the experimental data used are from Refs. [5–9,20–55].

700 keV. In these experiments, they did see a sizable LEE. It could thus be that the LEE is present in some or all of the nuclei marked off with circles and diamonds in the figure.

Over the past several years, different theoretical interpretations have been put forward to explain the LEE. In fact, the terminology varies, and the phenomenon has been variously referred to as LEE, *upbend* [6], low-energy magnetic dipole radiation (LEMAR) [56], and *zero limit* [57]. If a phenomenon with more than three names can be considered a hot topic, then this clearly qualifies. In the following, we make an attempt to summarize the theoretical work that has been done to explain the LEE.

Perhaps the first line of demarcation should be drawn between those works explaining the LEE as $M1$ or $E1$ radiation. Litvinova *et al.* used the thermal-continuum quasiparticle random-phase approximation to demonstrate a low-energy enhancement in the $E1$ strength function [58], introducing a (free) temperature parameter to reproduce the data of ^{94,96,98}Mo and ^{116,122}Sn at low transition energies. On the other hand, a number of authors have explained the LEE as $M1$ radiation by means of shell-model calculations but with varying interpretations of the underlying mechanism.

It is difficult to calculate $E1$ strength functions in the shell model, because it requires transitions between wave-function components from different major shells, so-called $1\hbar\omega$ transitions, due to the parity change in the $E1$ selection rule. Inclusion of $1\hbar\omega$ excitations requires a large model space; hence, the dimensions of the calculation quickly blow up. It can, however, be done in some cases, for example by Schwengner *et al.* [59] and Sieja [60]. Still, most shell-model work related to the quasicontinuum strength function to date has been done for $M1$ within $0\hbar\omega$.

The first shell-model study was done by Schwengner *et al.* [61], who studied Zr and Mo isotopes and compared calculations to strength function data from the Oslo group. They obtained good agreement with the low-energy ($E_\gamma \leqslant$ 2 MeV) γ-ray strength, and were able to explain almost the complete strength for $E_\gamma < 2$ MeV as being of $M1$ type. They showed that both the distribution of $B(M1)$ values as a function of E_γ and the strength function $f_{M1}(E_\gamma)$ can be well fitted by an exponential function, $B_0 \exp(-E_\gamma/T_B)$, with $T_B \sim 0.3 - 0.5$ MeV and $T_B \sim 0.5$ MeV for $B(M1)$ and f_{M1}, respectively. Further, the mechanism behind the LEE was explained as being due to a recoupling of the spins of

FIG. 2. Calculated $M1$ γ-ray strength functions of Ga isotopes using the JUN45 interaction.

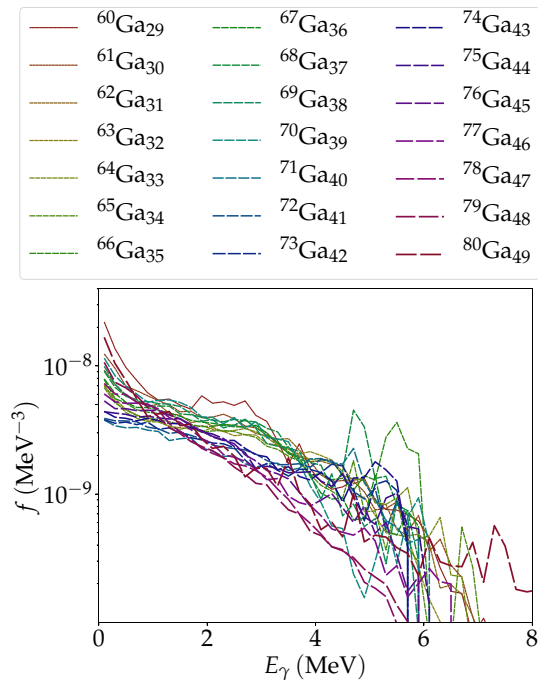FIG. 3. The amount of strength between 0 and 2 MeV relative to the strength between 2 and 6 MeV, plotted as function of neutron number for isotopic chains calculated with the JUN45 and CA48MH1G interactions. See text for details.

high-j protons and neutrons, analogous to the shears-band phenomenon.

Brown and Larsen [62] investigated the strength function of ^{56,57}Fe and were also able to explain it as an $M1$ feature. They further showed that the main contribution to the enhancement is from transition components within orbitals of high j, in this case from the $f_{7/2}$ orbital.

In a subsequent work, Schwengner *et al.* studied the LEE in a series of Fe isotopes extending into the middle of the neutron shell [56]. They found evidence for a *bimodality* in the $M1$ strength function, where the total strength is approximately preserved, but the LEE is diminished in the midshell isotopes to allow for the emergence of a scissors resonance at $E_\gamma \sim$ 3 MeV. As in the previous work in Ref. [61], they stated that the mechanism generating the enhancement is analogous to that of shears bands, i.e., $M1$ transitions generated by a large magnetic dipole moment vector rotating orthogonally to the nuclear spin [63].

Karampagia *et al.* [64] presented an interesting study using a "toy model" where only the $f_{7/2}$ orbital was included, for both protons and neutrons. With this model space, they studied ^{49,50}Cr and ^{48}V. They again found evidence for a low-energy enhancement, and they showed that its slope is dependent upon the strength of the (in isospin formalism) $T = 1$ matrix elements of the nucleon-nucleon interaction. Like Schwengner [61], they also fitted the $B(M1)$ distribution

to an exponential function, but found a much larger T_B of 1.33 MeV, i.e., a significantly gentler incline.

Sieja [60] considered the nuclei ^{43,44}Sc and ^{44,45}Ti and obtained both $E1$ and $M1$ strengths by considering a model space comprising three major shells. She found a nonzero low-energy limit of the $E1$ strength function, albeit no enhancement, as the LEE is still explained by the $M1$ component. The $E1$ strength function, although flat, was found to be an order of magnitude weaker than the $M1$ in the low-energy region, thus making no difference to the total strength.

III. SYSTEMATIC SHELL-MODEL CALCULATIONS

The present work follows the tradition of using the shell model. We employ KSHELL [65], a very efficient M-scheme shell-model code able to calculate levels and transition strengths within very large model spaces. All the calculations presented here have been made publicly available through Zenodo [66]. As interaction and model space is taken JUN45 [67], which comprises the orbitals $(f_{5/2} pg_{9/2})$ atop a ^{56}Ni core. The valence space allows up to 22 protons and neutrons. To facilitate computation, the model space is truncated by turning off proton excitations to the $g_{9/2}$ orbital. We have checked that this does not have an effect on Cu isotopes but cannot rule out that it could impact nuclei with higher Z. Calculations are performed for the entire isotopic chains of Ni, Cu, Zn, Ga, Ge, and As that are within the model space, as well as some neutron-rich Se isotopes. For each nucleus, we calculate 100 levels of each parity and each spin between $J = 0$ ($J = 1/2$) and $J = 14$ ($J = 29/2$) for even (odd) A, respectively. We then calculate $B(M1)$ transition strengths for all allowed transitions and compile the γ-ray strength
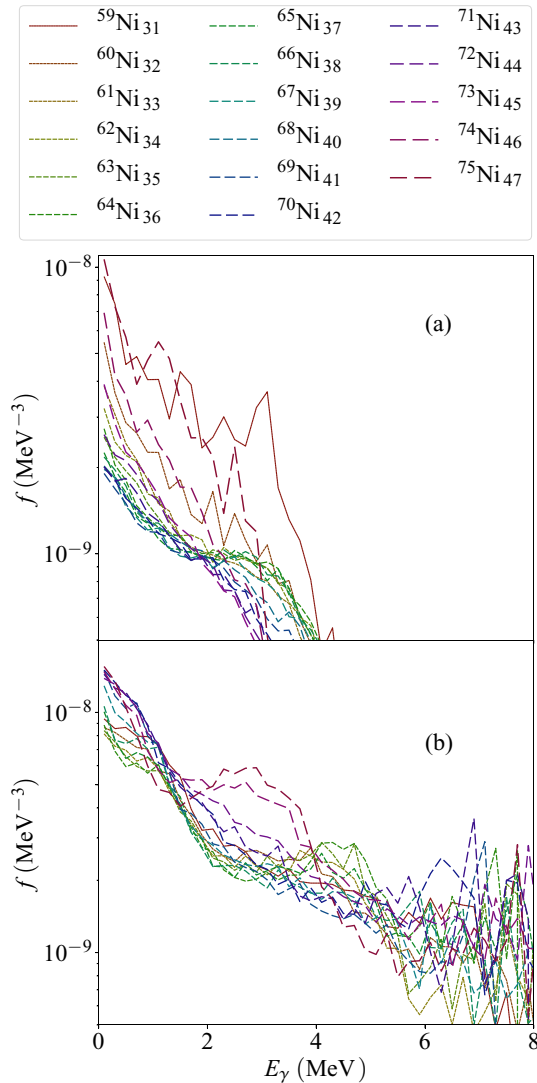
FIG. 4. γ-ray strength functions of isotopic chains of Ni calculated with ^{56}Ni (a) and ^{48}Ca (b) closed cores, respectively. See text for details.

FIG. 5. Calculated $M1$ γ-ray strength functions of Al isotopes using the USDA interaction.

function using Eq. (A1). A bin size of $\Delta E = 0.2$ MeV is used throughout the article unless otherwise stated. For the transition strength calculations in JUN45, we use the recommended effective g_s values of $g_{s,\text{eff}} = 0.7 g_{s,\text{free}}$ [67]. The dependence of the strength function on E_x, J, and π is removed by averaging. The average includes all calculated states and transitions. We observe that the strength function is remarkably similar for different choices of these parameters, except for statistical fluctuations—hence, averaging them out is justified, in accordance with the Brink hypothesis [68]. As

an example, we show the calculated $M1$ strength function of the chain of Ga isotopes in Fig. 2.

It is evident from Fig. 2 that the slope changes as function of neutron number. It starts off near $N = 28$, being very steep, flattening out toward mid-shell, and increasing back again when approaching the $N = 50$ closure. The same effect is present in the other isotopic chains that we have studied. To see this clearly, we have taken the ratio of the integrated strength in the intervals $E_\gamma \in [0, 2]$ MeV to $E_\gamma \in [2, 6]$ MeV, respectively. This is shown in Fig. 3 for all the isotopic chains. The overall trend of increasing low-energy strength toward the shell closures is present for all isotopes.

One could worry that some or all of these effects are due to the particulars of the model space, such as the choice of ^{56}Ni as closed core. In Fig. 4, we show the chain of Ni isotopes calculated both in the ^{56}Ni model space and in a different model space, namely using a ^{48}Ca core with the CA48MH1G interaction [6,69], truncated so that two protons can excite from the $f_{7/2}$ orbital. Details of the ^{48}Ca calculations are given in Ref. [6]. The trend of the strength functions is clearly the same, with more low-energy strength and steeper slope at the shell edges. The inclusion of the proton $f_{7/2}$ orbital does, however, change the strength function, notably by inducing what could be a spin-flip resonance at higher E_γ for some of the isotopes. The absolute values are also affected, becoming less variable and generally larger than with the ^{56}Ni core. It is not so surprising that the calculation with only neutrons in the model space gives lower $B(M1)$ values when we consider the structure of the $M1$ operator, $\widehat{M1} \propto g_l \vec{l} + g_s \vec{s}$. Since $g_l^p = 1$, $g_l^n = 0$, the absence of transitions between proton components
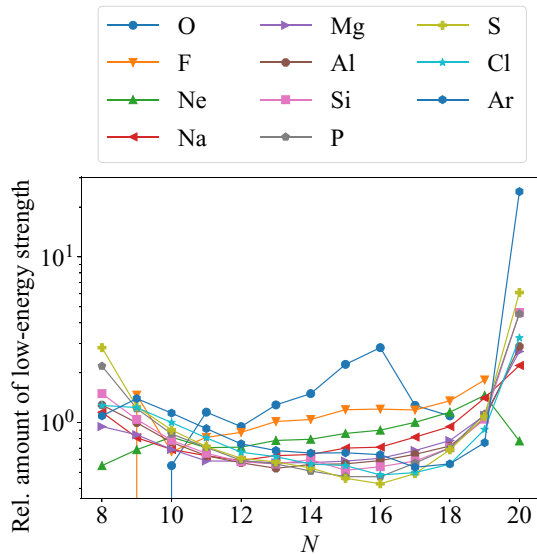
FIG. 6. Correlation between relative sum of low-energy strength and neutron number in the sd region. Note the logarithmic scale.

can lower the strengths. In Fig. 3, we have also included the ratio of LEE for the CA48MH1G-calculated Ni isotopes. In this case, the increases at low and high neutron numbers are complemented by an additional, large bump in the middle, peaking at ^{67}Ni. The Ni isotopes in the middle of the neutron shell are known to exhibit shape coexistence including spherical components [70]. This shape coexistence would involve proton excitations from the $f_{7/2}$ orbital, which means that it should not appear when using the ^{56}Ni closed core. The CA48MH1G interaction reproduces features attributed to shape coexistence in ^{70}Ni [6]. Hence, this midshell LEE bump can be interpreted to be consistent with the systematic trends.

Among the JUN45-calculated isotopic chains plotted in Fig. 3, Cu stands out, being linear rather than parabolic as function of N. Since Cu has only one proton on top of the ^{56}Ni core, it is possible that the linear trend is an artifact of the restricted model space. To check this, we again used the CA48MH1G interaction and calculated ^{60,62,64,66,72,74}Cu, allowing up to two proton excitations from the $f_{7/2}$ as was done for the Ni isotopes. Interestingly, the linearity remains, as shown by the dashed line in Fig. 3. This seems to indicate that the LEE variation with neutron number is hindered in nuclei with one proton atop magicity. We also note that the same linear trend is present in the fluorine isotopes shown below.

We have made similar calculations as the ones described above in a different mass region, namely the sd shell on top of a ^{16}O closed core, using the USDA interaction [71]. For this model space, we are able to calculate all isotopes without any truncation. With this interaction, $B(M1)$ strengths are calculated using $g_{s,\text{eff}} = 0.9 g_{s,\text{free}}$ [71]. In Fig. 5, we show the results for the isotopic chain of Al. These strength functions are generally much more flat but reveal the same
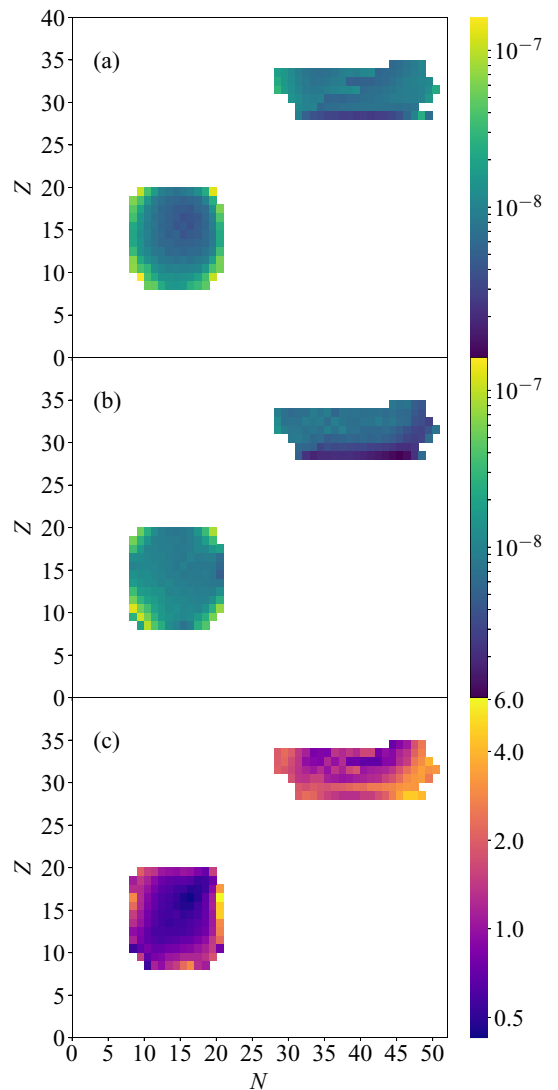
FIG. 7. Integrated γ-ray strength from (a) 0 to 2 MeV and (b) 2 to 6 MeV, respectively, and (c) the fraction of the integrated γ-ray strength from 0 to 2 MeV relative to the 2 to 6 MeV range, i.e., panel (a) divided by panel (b).

trend of increase toward magicity. Figure 6 displays the relative amount of low-energy strength for all isotopic chains. There is less change in the LEE as function of N in the middle of the neutron shell compared to the JUN45 calculations, but a larger jump at the edges. To make the midshell variations more visible, we have used a logarithmic scale.

In Fig. 7, we have plotted the integrated strength as a nuclear chart. Figures 7(a) and 7(b) show the strength integrated from 0 to 2 MeV and from 2 to 6 MeV, respectively,

FIG. 8. Calculated total dipole strength functions for ^{29}Si (a) and ^{44}Sc (b).

FIG. 9. Low-energy $M1$ strength function of ^{56}Fe compiled from discrete experimental data. The bin width is $\Delta E = 0.5$ MeV. See text for details.

and Fig. 7(c) shows the ratio between the previous two. This presentation reveals several interesting features. First of all, the calculations indicate that the low-energy enhancement is more pronounced near shell closures. Furthermore, the overall steepness of the strength is much higher in the $f_{5/2}pg_{9/2}$ region than the sd region. Lastly, in both model spaces, the southeastern corner is enhanced relative to the southwestern one. This is interesting, because it is consistent with the shears band picture advocated in Ref. [56], as discussed in Sec. II. We note that the same feature is apparent also in the northern corners of the sd shell, where the north*western* corner has the constructive alignment of proton holes with neutron particles. Looking at Fig. 1, this is consistent with the experimental evidence for nuclei with $A \leqslant 100$, where an enhancement has been seen in all cases. It is also consistent with the absence of an LEE in the midshell regions above ^{132}Sn and ^{208}Pb. However, it is seemingly at odds with the data for $^{105-108}$Pd, ^{111,112}Cd, and $^{116-119,121,122}$Sn, where no LEE is seen, despite their proximity to the $Z = 50$ shell closure. There could be several explanations for this. It could be that the LEE is very steep, and thus pushed to lower E_γ than experimentally accessible. It could also be that the proton shell closure is not a major driving factor for the LEE by itself, or there could be some other mechanism suppressing LEE in this region.

Turning away from the question of relative steepness, it seems from the present calculations like the $M1$ LEE turns flat rather than disappearing completely, even for the midshell sd nuclei. This is important, because it implies that an $M1$ correction term to the $E1$ Lorentzian-like shape typically used in phenomenological models is needed for all nuclei—but with variable slope. To investigate this point, we have calculated $E1$ strengths for ^{29}Si. In addition, we have considered ^{44}Sc, located in the fp shell. The calculations are shown in Figs. 8(a) and 8(b), respectively. The nickel mass region is unfortunately not accessible to $E1$ calculations. We use the SDPF-MU interaction [72], which comprises the sd and fp shells, allowing the cross-shell excitations essential for $E1$ transitions. We have applied a $1\hbar\omega$ truncation, meaning that the single-particle basis configurations are limited to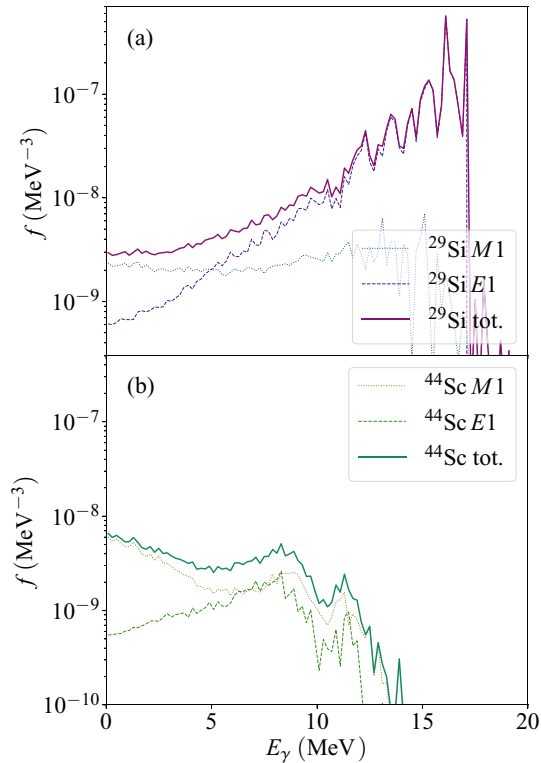 ones where at most one particle is excited across the sd-fp shell gap. The Lawson method [73–75] with $\beta = 100$ MeV is used to push the spurious center-of-mass states up to energies outside the considered range. For the $E1$ transition calculations, we used effective charges of $e_{\mathrm{eff}}^p = (1 + \chi)e$, $e_{\mathrm{eff}}^n = \chi e$, with $\chi = -Z/A$ [76]. In both cases, we obtain an $E1$ strength consistent with a generalized Lorentzian (GLO) tail from the giant dipole resonance (GDR) [77]. The need for an $M1$ correction is evident in both cases. For ^{29}Si it only serves to change the slope of the GLO, while for ^{44}Sc it completely dominates the low-energy part of the strength function, demonstrating an LEE.

Incidentally, we can compare our results with Sieja's calculations for the $E1$ strength in ^{44}Sc. We find a steeper slope on the low-energy tail of the strength function compared to Fig. 6 in Ref. [60]. This has a large influence on the summed dipole strength function at $E_\gamma \approx 5$ MeV, where we observe a minimum reminiscent of that usually present in the strength function of LEE nuclei. The absolute values of both the $E1$ and $M1$ strength functions are found in the present work to be an order of magnitude lower than in Ref. [60]. This is due to differences in how the strength function is extracted from the
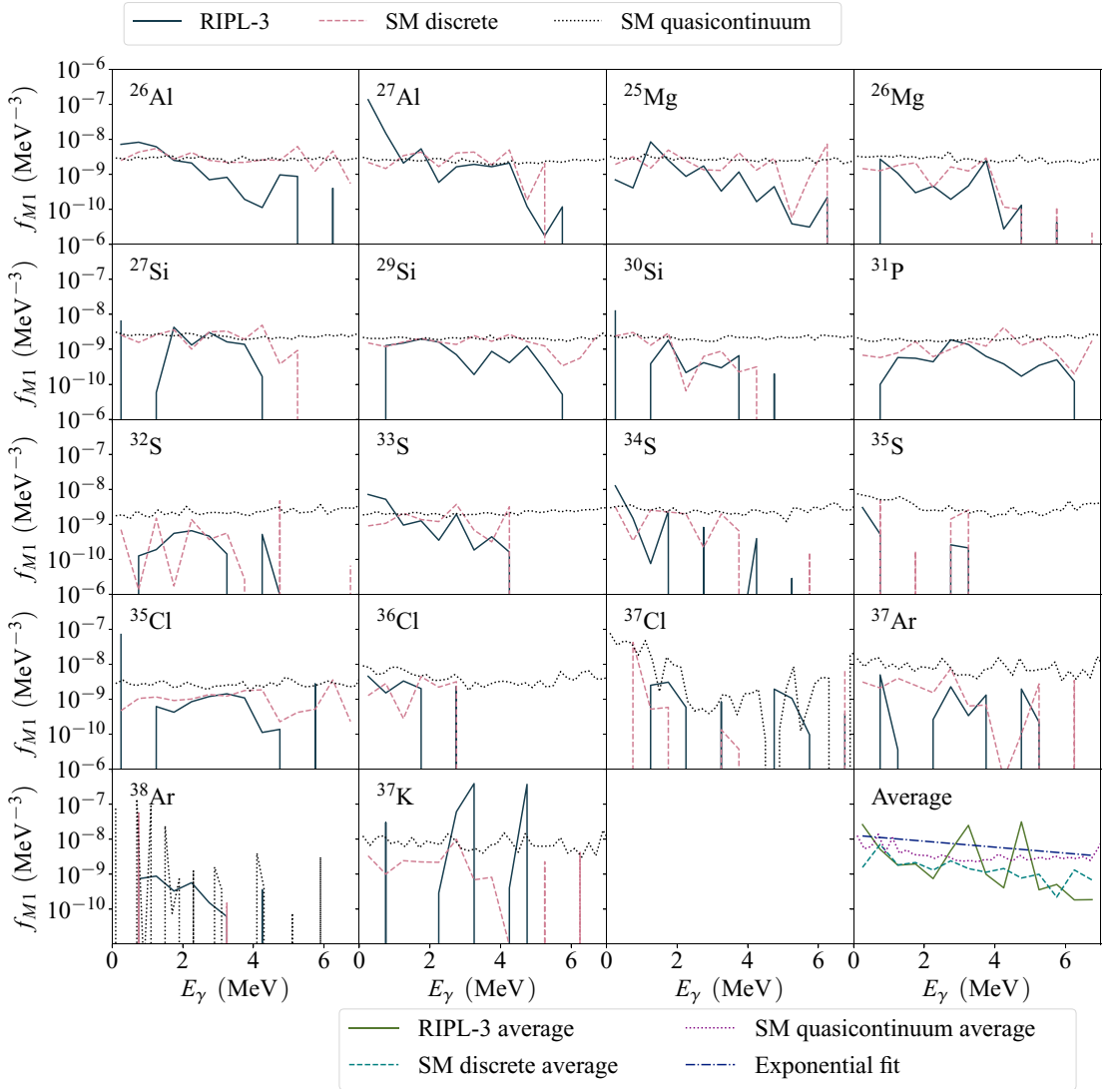
FIG. 10. $M1$ strength function of different sd shell nuclei. The bin width is $\Delta E = 0.5$ MeV.

$B(E1/M1)$ values (see the Appendix). Both calculations are consistent with the shape of the experimental γ-ray strength function of ^{44}Sc from Ref. [27], but Sieja's provide the best match for the absolute value.

IV. COMPARISONS WITH DISCRETE EXPERIMENTAL DATA

Many nuclei are so well studied that we have access to experimental information about levels, lifetimes and branching ratios up to quite high excitation energy. It is interesting to see if this information can be used to compile a strength function, and how it compares to shell model calculations. To this end, we extract experimental information from the Reference Input Parameter Library (RIPL-3) library [78]. We choose it over other databases due to the ease with which it allows data parsing, despite its lacking transition multipolarity information. We thus extract a strength function of *presumed* $M1$ transitions by selecting transitions between levels where $|J_i - J_f| \leqslant 1$, $\pi_i \pi_f = +1$. This does not rule out $E2$ mixing, but based on the power suppression in the multipole expansion, $M1$ is *a priori* expected to dominate. As such, this gives
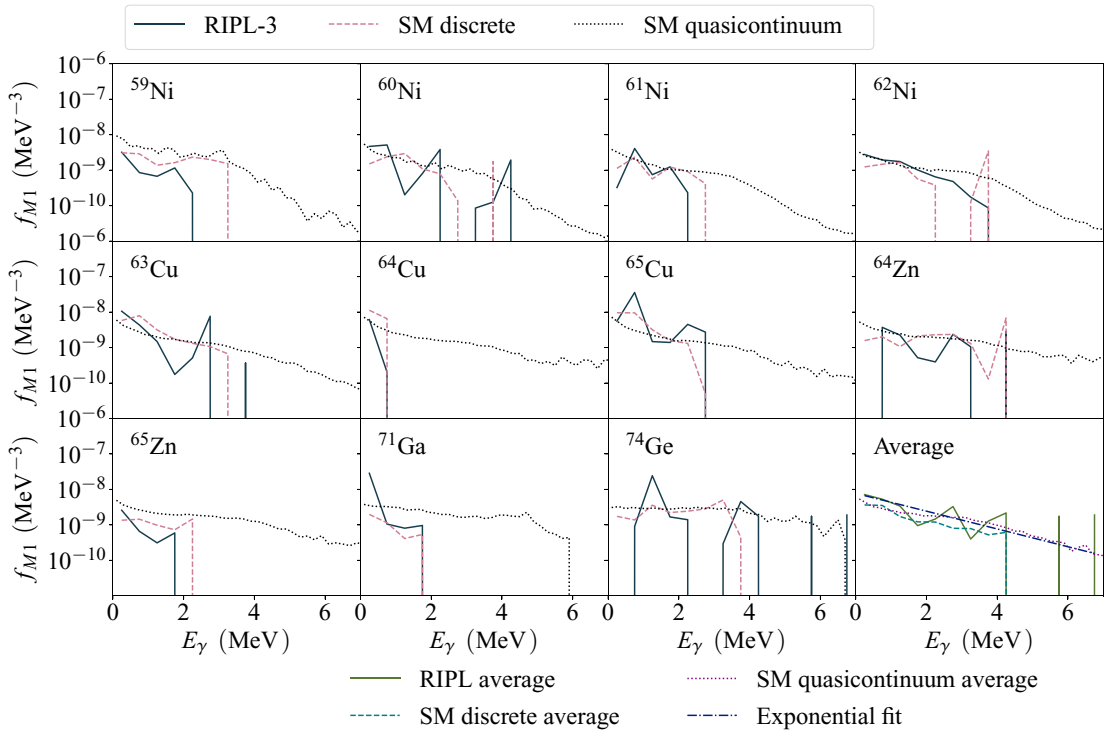
FIG. 11. $M1$ strength function of different $f_{5/2}pg_{9/2}$ shell nuclei. The bin width is $\Delta E = 0.5$ MeV.

an impression of how the low-excitation $M1$ energy strength function behaves.

For each nucleus considered, we parse the entry in the RIPL-3 library and look for all levels with $E_x \in [0, 7]$ MeV that pass the aforementioned requirement and that have a known lifetime and measured γ-ray branching ratios. From this information, we obtain partial decay widths, which we average over (E_x, E_γ, J, π) bins. The strength function is then obtained by multiplying by the level density at the corresponding (E_x, J, π), which we obtain considering *all* known levels, not just the ones with known lifetimes. This is important to get the correct absolute value of the strength function (otherwise it would be too low; see the Appendix). By comparing the level density from the discrete levels to that from shell-model calculations, we verify that the experimental level scheme seems to be complete up to the excitation energies we consider,[1] as shown in Fig. 12. Finally, we average over (E_x, J, π) to obtain the average strength function depending only on E_γ.

We demonstrate this for the case of ^{56}Fe in Fig. 9. The wealth of available experimental information enables us to construct a strength function based on 90 transitions selected according to the criteria described above. We compare this to shell-model calculations done using the GXPF1A [79] interaction, as was used in Ref. [62]. The agreement between experiment and calculations is excellent, both in terms of slope and absolute value. The results for a variety of nuclei in the sd shell and $f_{5/2}pg_{9/2}$ shell regions are shown in Figs. 10 and 11, respectively. For these regions, we compare results to the previously discussed shell-model calculations. The dotted line in each strength function panel shows the "quasicontinuum" strength function for that nucleus, by which we mean the strength function compiled using all calculated levels, in the same way as was done for the systematics above. We have also extracted a strength function from the shell-model data by selecting discrete transitions similar to the RIPL-3 ones. Specifically, for each RIPL-3 level used in the construction of the strength function, we have taken the lowest energy shell-model level with the same spin and parity, and included all transitions from this level in the discrete shell-model strength function. (We also tried an alternative method selecting the closest-in-energy shell model level, but this gives much poorer results.)

---

[1]If the total level density from RIPL-3 falls below the shell model level density before the "RIPL-3 used" density dies off, this would indicate that we are compiling a strength function using too low level density. This does not seem to be the case here.

TABLE I. Fit parameters for experimental RIPL-3 strength functions. See text for details.

	B (10^{-8} MeV^{-3})	T (MeV)
sd	1.30	5.09
$f_{5/2}pg_{9/2}$	0.77	1.73
^{56}Fe	0.94	2.07

In an attempt to quantify the differences between the mass regions considered, we make a fit to an exponential function $f(E_\gamma) = B \exp(E_\gamma/T)$. To maximize statistics, we fit the average strength function in each of the regions (the green line shown in the last panel of each of the figures). We have also fitted ^{56}Fe separately. The results for the fit are listed in Table I. With all the assumptions that go into this fit, we should refrain from drawing strong conclusions, but it is striking that the sd fit displays almost factor 3 gentler slope than $f_{5/2}pg_{9/2}$. This is compatible with the trend from the systematic calculations.

V. SUMMARY AND OUTLOOK

In this work, we have performed large-scale shell model calculations of $M1$ γ-ray strength functions for many isotopic chains in different major shells, focusing on the low-energy behavior. We observe systematic trends in the calculations. The slope of the strength functions is generally steeper in the $f_{5/2}pg_{9/2}$ than in the sd shell. This correlates with the availability of high-j orbitals. Furthermore, the slope is steeper near the shell closures and gentler in the midshell region for both model spaces. This is especially pronounced in the region northwest and southeast of a doubly magic nucleus, where, in the shears-bands picture, proton and neutron magnetic moments align to generate strong magnetic transitions.

The present findings consolidate several insights from previous studies—such as the dependence on high-j orbitals, the coupling of protons and neutrons, and the relation to shears bands—and shows that rather than being separate, incompatible explanations of the low-energy enhancement, they may be complementary pieces of the same puzzle. Based on this and previous studies, we propose that large low-energy magnetic decay strength is a feature inherent to nuclei when they are excited to high energies. The slope of the LEE seems to correlate with the availability of high-j orbitals, which also correlates with nuclear mass. While the slope of the $M1$ strength varies between nuclei and mass regions, it never seems to disappear completely even for the lightest nuclei but merely turns flat. Hence, in phenomenological terms, an $M1$ correction to the strength function at the tail of the $E1$ GDR is probably required for all nuclei, modifying its low-energy shape. Indeed, for a large number of them, the low-energy $M1$ strength displays an enhancement. If, as these calculations indicate, the LEE is especially strong for very neutron-rich nuclei, it could significantly impact (n, γ) reaction rates relevant to the r process.

While there are experimental difficulties preventing definitive exclusions of the LEE with the Oslo method, the data that
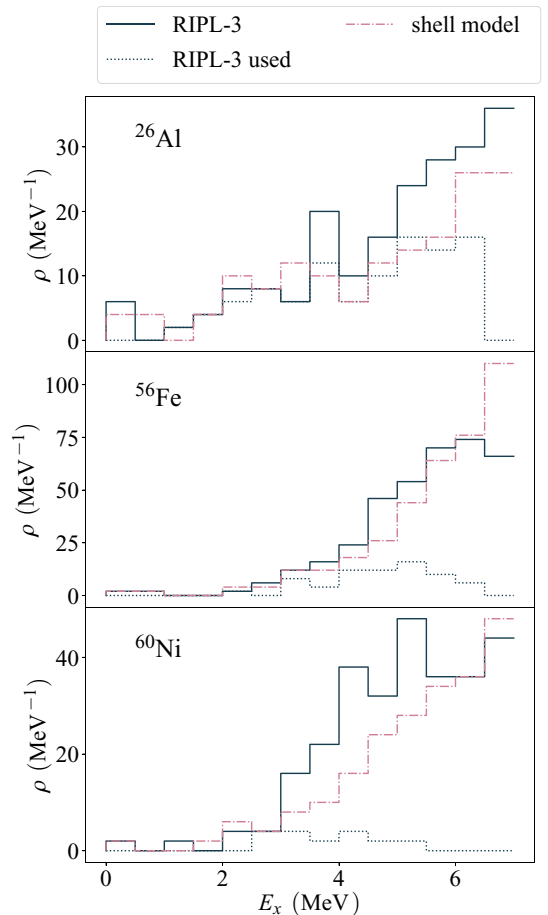
FIG. 12. Level densities from discrete data for different nuclei, compared with shell-model calculations. The lines labeled "RIPL-3 used" indicate the level density counting only the levels whose lifetimes and branching ratios were used to compile the strength function. The bin width is $\Delta E = 0.5$ MeV.

exist support our present findings. It would be very interesting to study other nuclei in midshell regions, and preferably employing experimental techniques enabling the extraction of the strength function to low γ-ray energy. It is equally interesting to consider nuclei in the "shears regions," where we expect the LEE to be most significant. Neutron-rich Xe isotopes are a promising case in this regard, located as they are just northwest of the doubly magic ^{132}Sn. An experiment has recently been carried out on ^{133}Xe at iThemba LABS and analysis using the Oslo method in inverse kinematics is under way [80]. We eagerly await these experimental results.

All calculations have been made publicly available on Zenodo [66].
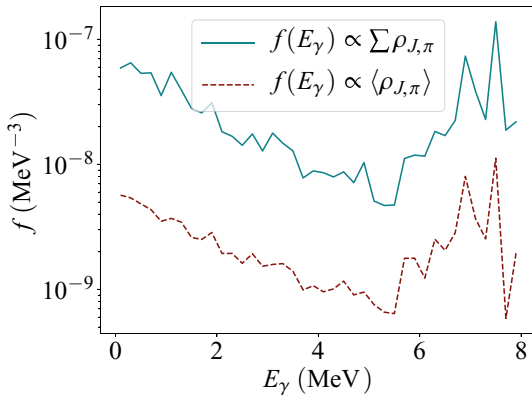
FIG. 13. Comparison of γ-ray strength functions for ^{56}Fe from shell-model calculations extracted using two different methods. See text for details.

APPENDIX: ISSUES WITH CONVERSION OF B(M1) VALUES TO STRENGTH FUNCTION

We recently became aware of an issue with how shell-model calculations are converted to γ-ray strength functions [81]. The conventional definition of the strength function, as found in Ref. [82], is

$$
\begin{aligned}
&f_{M1}(E_\gamma, E_i, J_i, \pi_i) \\
&= \frac{16\pi}{9\hbar^3 c^3} \langle B(M1) \rangle (E_\gamma, E_i, J_i, \pi_i) \rho(E_i, J_i, \pi_i),
\end{aligned} \quad \text{(A1)}
$$

where $\rho(E_i, J_i, \pi_i)$ is the partial level density and $\langle B(M1) \rangle$ is the average transition strength of states at excitation energy E_i, spin J_i, and parity π_i. Using that $\mu_N = (e\hbar)/(2m_p c)$, the constant in front works out to

$$
\frac{16\pi}{9\hbar^3 c^3} = 11.58 \times 10^{-9} \, \mu_N^{-2} \, \text{MeV}^{-2}. \quad \text{(A2)}
$$

However, in some works, the *total* level density has been used in place of the partial. Since the total level density is $\rho_{\text{tot}}(E_x) = \sum_{J,\pi} \rho(E_x, J, \pi)$, this introduces (i) an artificial overall enhancement of the strength function and (ii) an arbitrary scaling depending on how many J, π combinations were included in the calculations. In order to demonstrate the difference, we have repeated the calculation of Ref. [62] and extracted the strength function using both the total and the partial level density. In each case, we average over E_x and J ($\pi = +$ only). It results in a difference of about a factor 10, as expected since the calculation includes 11 different spins. The effect is demonstrated in Fig. 13. In this work, we keep to the original definition from Ref. [82].

[1] J. S. Al-Khalili, Nucl. Phys. A **751**, 469 (2005).

[2] H. A. Bethe, Phys. Rev. **50**, 332 (1936).

[3] T. Ericson, Nucl. Phys. **11**, 481 (1959).

[4] H. A. Weidenmüller and G. E. Mitchell, Rev. Mod. Phys. **81**, 539 (2009).

[5] A. Voinov, E. Algin, U. Agvaanluvsan, T. Belgya, R. Chankova, M. Guttormsen, G. E. Mitchell, J. Rekstad, A. Schiller, and S. Siem, Phys. Rev. Lett. **93**, 142504 (2004).

[6] A. C. Larsen, J. E. Midtbø, M. Guttormsen, T. Renstrøm, S. N. Liddick, A. Spyrou, S. Karampagia, B. A. Brown, O. Achakovskiy, S. Kamerdzhiev *et al.*, Phys. Rev. C **97**, 054329 (2018).

[7] A. C. Larsen, N. Blasi, A. Bracco, F. Camera, T. K. Eriksen, A. Görgen, M. Guttormsen, T. W. Hagen, S. Leoni, B. Million *et al.*, Phys. Rev. Lett. **111**, 242504 (2013).

[8] A. Simon, M. Guttormsen, A. C. Larsen, C. W. Beausang, P. Humby, J. T. Burke, R. J. Casperson, R. O. Hughes, T. J. Ross, J. M. Allmond *et al.*, Phys. Rev. C **93**, 034303 (2016).

[9] A. C. Larsen, M. Guttormsen, N. Blasi, A. Bracco, F. Camera, L. C. Campo, T. K. Eriksen, A. Görgen, T. W. Hagen, V. W. Ingeberg *et al.*, J. Phys. G: Nucl. Part. Phys. **44**, 064005 (2017).

[10] M. D. Jones, A. O. Macchiavelli, M. Wiedeking, L. A. Bernstein, H. L. Crawford, C. M. Campbell, R. M. Clark,

M. Cromaz, P. Fallon, I. Y. Lee *et al.*, Phys. Rev. C **97**, 024327 (2018).

[11] M. Arnould, S. Goriely, and K. Takahashi, Phys. Rep. **450**, 97 (2007).

[12] National Research Council, *Connecting Quarks with the Cosmos: Eleven Science Questions for the New Century* (The National Academic Press, Washington, DC, 2001).

[13] B.P. Abbott *et al.* (LIGO Scientific Collaboration and Virgo Collaboration), Phys. Rev. Lett. **119**, 161101 (2017).

[14] M. R. Drout, A. L. Piro, B. J. Shappee, C. D. Kilpatrick, J. D. Simon, C. Contreras, D. A. Coulter, R. J. Foley, M. R. Siebert, N. Morrell *et al.*, Science **358**, 1570 (2017).

[15] E. Pian, P. D'Avanzo, S. Benetti, M. Branchesi, E. Brocato, S. Campana, E. Cappellaro, S. Covino, V. D'Elia, J. P. U. Fynbo *et al.*, Nature (London) **551**, 67 (2017).

[16] M. Eichler, A. Arcones, A. Kelic, O. Korobkin, K. Langanke, T. Marketin, G. Martinez-Pinedo, I. Panov, T. Rauscher, S. Rosswog *et al.*, Astrophys. J. **808**, 30 (2015).

[17] J. de Jesús Mendoza-Temis, M.-R. Wu, K. Langanke, G. Martínez-Pinedo, A. Bauswein, and H.-T. Janka, Phys. Rev. C **92**, 055805 (2015).

[18] A. C. Larsen and S. Goriely, Phys. Rev. C **82**, 014318 (2010).

[19] K. Miernik [https://github.com/kmiernik/Chart-of-nuclides-drawer].

[20] A. Voinov, M. Guttormsen, E. Melby, J. Rekstad, A. Schiller, and S. Siem, Phys. Rev. C **63**, 044313 (2001).

[21] E. Melby, M. Guttormsen, J. Rekstad, A. Schiller, S. Siem, and A. Voinov, Phys. Rev. C **63**, 044309 (2001).

[22] S. Siem, M. Guttormsen, K. Ingeberg, E. Melby, J. Rekstad, A. Schiller, and A. Voinov, Phys. Rev. C **65**, 044318 (2002).

[23] M. Guttormsen, A. Bagheri, R. Chankova, J. Rekstad, S. Siem, A. Schiller, and A. Voinov, Phys. Rev. C **68**, 064306 (2003).

[24] U. Agvaanluvsan, A. Schiller, J. A. Becker, L. A. Bernstein, P. E. Garrett, M. Guttormsen, G. E. Mitchell, J. Rekstad, S. Siem, A. Voinov, and W. Younes, Phys. Rev. C **70**, 054611 (2004).

[25] M. Guttormsen, R. Chankova, U. Agvaanluvsan, E. Algin, L. A. Bernstein, F. Ingebretsen, T. Lönnroth, S. Messelt, G. E. Mitchell, J. Rekstad et al., Phys. Rev. C **71**, 044307 (2005).

[26] A. C. Larsen, R. Chankova, M. Guttormsen, F. Ingebretsen, S. Messelt, J. Rekstad, S. Siem, N. U. H. Syed, S. W. Ødegård, T. Lönnroth, A. Schiller, and A. Voinov, Phys. Rev. C **73**, 064301 (2006).

[27] A. C. Larsen, M. Guttormsen, R. Chankova, F. Ingebretsen, T. Lönnroth, S. Messelt, J. Rekstad, A. Schiller, S. Siem, N. U. H. Syed, and A. Voinov, Phys. Rev. C **76**, 044303 (2007).

[28] E. Algin, U. Agvaanluvsan, M. Guttormsen, A. C. Larsen, G. E. Mitchell, J. Rekstad, A. Schiller, S. Siem, and A. Voinov, Phys. Rev. C **78**, 054321 (2008).

[29] N. U. H. Syed, M. Guttormsen, F. Ingebretsen, A. C. Larsen, T. Lönnroth, J. Rekstad, A. Schiller, S. Siem, and A. Voinov, Phys. Rev. C **79**, 024316 (2009).

[30] N. U. H. Syed, A. C. Larsen, A. Bürger, M. Guttormsen, S. Harissopulos, M. Kmiecik, T. Konstantinopoulos, M. Krtička, A. Lagoyannis, T. Lönnroth et al., Phys. Rev. C **80**, 044309 (2009).

[31] H. T. Nyhus, S. Siem, M. Guttormsen, A. C. Larsen, A. Bürger, N. U. H. Syed, G. M. Tveten, and A. Voinov, Phys. Rev. C **81**, 024325 (2010).

[32] H. K. Toft, A. C. Larsen, U. Agvaanluvsan, A. Bürger, M. Guttormsen, G. E. Mitchell, H. T. Nyhus, A. Schiller, S. Siem, N. U. H. Syed, and A. Voinov, Phys. Rev. C **81**, 064311 (2010).

[33] M. Guttormsen, A. C. Larsen, A. Bürger, A. Görgen, S. Harissopulos, M. Kmiecik, T. Konstantinopoulos, M. Krtička, A. Lagoyannis, T. Lönnroth et al., Phys. Rev. C **83**, 014312 (2011).

[34] H. K. Toft, A. C. Larsen, A. Bürger, M. Guttormsen, A. Görgen, H. T. Nyhus, T. Renstrøm, S. Siem, G. M. Tveten, and A. Voinov, Phys. Rev. C **83**, 044320 (2011).

[35] A. Bürger, A. C. Larsen, S. Hilaire, M. Guttormsen, S. Harissopulos, M. Kmiecik, T. Konstantinopoulos, M. Krtička, A. Lagoyannis, T. Lönnroth et al., Phys. Rev. C **85**, 064328 (2012).

[36] A. C. Larsen, I. E. Ruud, A. Bürger, S. Goriely, M. Guttormsen, A. Görgen, T. W. Hagen, S. Harissopulos, H. T. Nyhus, T. Renstrøm et al., Phys. Rev. C **87**, 014319 (2013).

[37] M. Guttormsen, L. A. Bernstein, A. Görgen, B. Jurado, S. Siem, M. Aiche, Q. Ducasse, F. Giacoppo, F. Gunsing, T. W. Hagen et al., Phys. Rev. C **89**, 014302 (2014).

[38] H. Utsunomiya, S. Goriely, T. Kondo, C. Iwamoto, H. Akimune, T. Yamagata, H. Toyokawa, H. Harada, F. Kitatani, Y.-W. Lui et al., Phys. Rev. C **88**, 015805 (2013).

[39] T. K. Eriksen, H. T. Nyhus, M. Guttormsen, A. Görgen, A. C. Larsen, T. Renstrøm, I. E. Ruud, S. Siem, H. K. Toft, G. M. Tveten, and J. N. Wilson, Phys. Rev. C **90**, 044311 (2014).

[40] B. V. Kheswa, M. Wiedeking, F. Giacoppo, S. Goriely, M. Guttormsen, A. C. Larsen, F. L. Bello Garrote, T. K. Eriksen, A. Görgen et al., Phys. Lett. B **744**, 268 (2015).

[41] A. Spyrou, S. N. Liddick, A. C. Larsen, M. Guttormsen, K. Cooper, A. C. Dombos, D. J. Morrissey, F. Naqvi, G. Perdikakis, S. J. Quinn et al., Phys. Rev. Lett. **113**, 232502 (2014).

[42] T. G. Tornyi, M. Guttormsen, T. K. Eriksen, A. Görgen, F. Giacoppo, T. W. Hagen, A. Krasznahorkay, A. C. Larsen, T. Renstrøm, S. J. Rose et al., Phys. Rev. C **89**, 044323 (2014).

[43] A. C. Larsen, M. Guttormsen, R. Schwengner, D. L. Bleuel, S. Goriely, S. Harissopulos, F. L. Bello Garrote, Y. Byun, T. K. Eriksen, F. Giacoppo et al., Phys. Rev. C **93**, 045810 (2016).

[44] G. M. Tveten, A. Spyrou, R. Schwengner, F. Naqvi, A. C. Larsen, T. K. Eriksen, F. L. Bello Garrote, L. A. Bernstein, D. L. Bleuel, L. Crespo Campo et al., Phys. Rev. C **94**, 025804 (2016).

[45] D. Davesne, J. W. Holt, A. Pastore, and J. Navarro, Phys. Rev. C **91**, 014323 (2016).

[46] M. Guttormsen, S. Goriely, A. C. Larsen, A. Görgen, T. W. Hagen, T. Renstrøm, S. Siem, N. U. H. Syed, G. Tagliente, H. K. Toft et al., Phys. Rev. C **96**, 024313 (2017).

[47] T. Renstrøm, H.-T. Nyhus, H. Utsunomiya, R. Schwengner, S. Goriely, A. C. Larsen, D. M. Filipescu, I. Gheorghe, L. A. Bernstein, D. L. Bleuel et al., Phys. Rev. C **93**, 064302 (2016).

[48] L. Crespo Campo, F. L. Bello Garrote, T. K. Eriksen, A. Görgen, M. Guttormsen, K. Hadynska-Klek, M. Klintefjord, A. C. Larsen, T. Renstrøm et al., Phys. Rev. C **94**, 044321 (2016).

[49] L. Crespo Campo, A. Larsen, F. Bello Garrote, T. Eriksen, F. Giacoppo, A. Görgen, M. Guttormsen, M. Klintefjord, T. Renstrøm, E. Sahin et al., Phys. Rev. C **96**, 014312 (2017).

[50] B. V. Kheswa, M. Wiedeking, J. A. Brown, A. C. Larsen, S. Goriely, M. Guttormsen, F. L. Bello Garrote, L. A. Bernstein, D. L. Bleuel, T. K. Eriksen et al., Phys. Rev. C **95**, 045805 (2017).

[51] A. Spyrou, A. C. Larsen, S. N. Liddick, F. Naqvi, B. P. Crider, A. C. Dombos, M. Guttormsen, D. L. Bleuel, A. Couture, L. C. Campo et al., J. Phys. G: Nucl. Part. Phys. **44**, 044002 (2017).

[52] T. Renstrøm, H. Utsunomiya, H. T. Nyhus, A. C. Larsen, M. Guttormsen, G. M. Tveten, D. M. Filipescu, I. Gheorghe, S. Goriely, S. Hilaire et al., Phys. Rev. C **98**, 054310 (2018).

[53] T. Renstrøm, G. M. Tveten, J. E. Midtbø, H. Utsunomiya, O. Achakovskiy, S. Kamerdzhiev, B. A. Brown, A. Avdeenkov, T. Ari-izumi, A. Görgen et al., arXiv:1804.08086.

[54] G. M. Tveten, T. Renstrøm, A. C. Larsen, H. Utsunomiya, K. Stopani, S. Belyshev, M. Guttormsen, T. Ari-izumi, F. L. B. Garrote, D. L. Bleuel et al., arXiv:1804.08109.

[55] M. Wiedeking, L. A. Bernstein, M. Krtička, D. L. Bleuel, J. M. Allmond, M. S. Basunia, J. T. Burke, P. Fallon, R. B. Firestone, B. L. Goldblum et al., Phys. Rev. Lett. **108**, 162503 (2012).

[56] R. Schwengner, S. Frauendorf, and B. A. Brown, Phys. Rev. Lett. **118**, 092502 (2017).

[57] H. Utsunomiya, T. Renstrøm, G. M. Tveten, S. Goriely, S. Katayama, T. Ari-izumi, D. Takenaka, D. Symochko, B. V. Kheswa, V. W. Ingeberg, T. Glodariu et al., Phys. Rev. C **98**, 054619 (2018).

[58] E. Litvinova and N. Belov, Phys. Rev. C **88**, 031302(R) (2013).

[59] R. Schwengner, R. Massarczyk, B. A. Brown, R. Beyer, F. Dönau, M. Erhard, E. Grosse, A. R. Junghans, K. Kosev, C. Nair et al., Phys. Rev. C **81**, 054315 (2010).

[60] K. Sieja, Phys. Rev. Lett. **119**, 052502 (2017).

[61] R. Schwengner, S. Frauendorf, and A. C. Larsen, Phys. Rev. Lett. **111**, 232504 (2013).

[62] B. A. Brown and A. C. Larsen, Phys. Rev. Lett. **113**, 252502 (2014).

[63] S. Frauendorf, Rev. Mod. Phys. **73**, 463 (2001)

[64] S. Karampagia, B. A. Brown, and V. Zelevinsky, Phys. Rev. C **95**, 024322 (2017).

[65] N. Shimizu, arXiv:1310.5431.

[66] J. E. Midtbø, A. C. Larsen, T. Renstrøm, F. L. Bello Garrote, and E. Lima, Supplemental Material: Consolidating the concept of low-energy magnetic dipole decay radiation, Zenodo, http://doi.org/10.5281/zenodo.1493221 (2018).

[67] M. Honma, T. Otsuka, T. Mizusaki, and M. Hjorth-Jensen, Phys. Rev. C **80**, 064323 (2009).

[68] D. M. Brink, doctoral thesis, Oxford University, Oxford, UK, 1955 (unpublished).

[69] B. A. Brown (private communication).

[70] S. Suchyta, S. N. Liddick, Y. Tsunoda, T. Otsuka, M. B. Bennett, A. Chemey, M. Honma, N. Larson, C. J. Prokop, S. J. Quinn *et al.*, Phys. Rev. C **89**, 021301(R) (2014).

[71] B. A. Brown and W. A. Richter, Phys. Rev. C **74**, 034315 (2006).

[72] Y. Utsuno *et al.*, Prog. Thor. Phys. Suppl. **196**, 304 (2012).

[73] C. W. Johnson, W. E. Ormand, K. S. McElvain, and H. Shan, BIGSTICK: A flexible configuration-interaction shell model code, LLNL-SM-739926, arXiv:1801.08432.

[74] D. Gloeckner and R. Lawson, Phys. Lett. B **53**, 313 (1974).

[75] R. Lawson, *Theory of the Nuclear Shell Model* (Clarendon Press, Oxford, UK, 1980).

[76] J. Suhonen, *From Nucleons to Nucleus: Concepts of Microscopic Nuclear Theory* (Springer-Verlag, Berlin, 2007), p. 124.

[77] J. Kopecky and M. Uhl, Phys. Rev. C **41**, 1941 (1990).

[78] R. Capote *et al.*, Nuclear Data Sheets **110**, 3107 (2009).

[79] M. Honma, T. Otsuka, B. A. Brown, and T. Mizusaki, Phys. Rev. C **65**, 061301(R) (2002).

[80] H. C. Berg, V. W. Ingeberg *et al.* (unpublished).

[81] B. A. Brown, S. Frauendorf, M. Guttormsen, S. Karampagia, A. C. Larsen, J. E. Midtbø, T. Renstrøm, R. Schwengner, and K. Sieja (private communication).

[82] G. A. Bartholomew, E. D. Earle, A. J. Ferguson, J. W. Knowles, and M. A. Lone, Adv. Nucl. Phys. **7**, 229 (1972).

Appendix A

Derivation of the γ-ray strength function

In this appendix, I give a derivation of the strength function f for $M1$ radiation. The aim is to obtain an expression for f that makes clear and explicit how it depends on the basic quantities, *i.e.* the individual levels and their partial decay widths, that are available from a shell model calculation or experimental tabulations. To avoid confusion, I will throughout this appendix denote the total radiative decay width for a level i by Γ_i and a partial decay width from i to f by $\gamma_{i \to f}$. The integral formula for the total radiative width, as it is stated in Ref. [73] but adapted to my notation, is taken as the defining equation for the strength function:

$$\langle \Gamma(E_i, J, \pi) \rangle = \sum_{XL} \int_0^{E_i} \langle \gamma^{XL}(E_i, E_\gamma, J, \pi) \rangle \sum_{J_f=J-L}^{J+L} \rho(E_i - E_\gamma, J_f, \pi_f) \, \mathrm{d}E_\gamma \tag{A.1}$$

$$= \sum_{XL} \int_0^{E_i} \frac{E_\gamma^{2L+1} f_{XL}(E_i, E_\gamma, J, \pi)}{\rho(E_i, J, \pi)} \sum_{J_f=J-L}^{J+L} \rho(E_i - E_\gamma, J_f, \pi_f) \, \mathrm{d}E_\gamma, \tag{A.2}$$

where the sum runs over all possible multipolarities XL. Let us begin by considering a single level i that has a number of possible final states $f = 1, 2, ..., N$ to which it can decay. For simplicity I consider only a single multipolarity, namely $M1$ radiation. We have that

$$\Gamma_i = \sum_{f=1}^{N} \gamma_{i \to f}. \tag{A.3}$$

Let us divide the final states into bins of width ΔE_f, and label the bins $b = 1, 2, ...N_b$. The sum can then be rewritten as

$$\Gamma_i = \sum_{b=1}^{N_b} \sum_{f \in b} \gamma_{i \to f}. \tag{A.4}$$

Because the aim is to get this over to an integral, let us define a helper function $\alpha_i(E_f)$ as

$$\alpha_i(E_f) = \frac{1}{\Delta E_f} \sum_{f \in b(Ef)} \gamma_{i \to f}, \tag{A.5}$$

where $b(E_f)$ is the bin covering the region $(E_f - \Delta E_f/2, E_f + \Delta E_f/2)$. (So E_f only takes on discrete values at this point.) We then have the (exact) relation

$$\Gamma_i = \sum_{E_f} \alpha_i(E_f) \Delta E_f. \tag{A.6}$$

Now, if ΔE_f is sufficiently small, this expression approximates the integral

$$\Gamma_i = \sum_{E_f} \alpha_i(E_f) \Delta E_f \approx \int_0^{E_i} \alpha_i(E_f) \, dE_f. \tag{A.7}$$

We would like to have this integral as a function of E_γ. Considering $\alpha(E_f)$, we see that for a given E_i, the E_f bin is equivalently described by $E_\gamma = E_i - E_f$, with corresponding bins $b'(E_\gamma) = b(E_f)$ and bin width $\Delta E_\gamma = \Delta E_f$. This gives

$$\alpha_i(E_f) = \tilde{\alpha}_i(E_\gamma) \equiv \frac{1}{\Delta E_\gamma} \sum_{f \in b'(E_\gamma)} \gamma_{i \to f}. \tag{A.8}$$

By using that $dE_\gamma = -dE_f$ and $E_\gamma(E_f = 0) = E_i$, $E_\gamma(E_f = E_i) = 0$, we can then rewrite the integral as

$$\Gamma_i = \int_0^{E_i} \alpha_i(E_f) \, dE_f = - \int_{E_i}^0 \alpha_i(E_f) \, dE_\gamma = \int_0^{E_i} \tilde{\alpha}_i(E_\gamma) \, dE_\gamma. \tag{A.9}$$

Let us now consider an ensemble I of initial states within some energy bin ΔE_I around E_I. We assume that all $i \in I$ have the same quantum numbers J^π so that they reach the same final states f (ignoring any structural effects that might hinder or enhance some specific transitions, *i.e.*, assuming statistical decay). The arithmetic mean of the total widths in I is

$$\langle \Gamma_i \rangle_I = \frac{1}{N_I} \sum_{i=1}^{N_I} \Gamma_i. \tag{A.10}$$

Substituting the integral gives

$$\frac{1}{N_I} \sum_{i=1}^{N_I} \Gamma_i \approx \frac{1}{N_I} \sum_{i=1}^{N_I} \int_0^{E_i} \tilde{\alpha}_i(E_\gamma) \, dE_\gamma. \tag{A.11}$$

By taking the arithmetic average of $\tilde{\alpha}_i(E_\gamma)$ over I,

$$\langle \tilde{\alpha}_i \rangle_I (E_\gamma) = \frac{1}{N_I} \sum_{i=1}^{N_I} \tilde{\alpha}_i(E_\gamma), \tag{A.12}$$

The average of the integrals can be rewritten as an integral of averages:

$$\frac{1}{N_I} \sum_{i=1}^{N_I} \int_0^{E_i} \tilde{\alpha}_i(E_\gamma) \, dE_\gamma = \int_0^{E_i} \frac{1}{N_I} \sum_{i=1}^{N_I} \tilde{\alpha}_i(E_\gamma) \, dE_\gamma \tag{A.13}$$

$$= \int_0^{E_i} \langle \tilde{\alpha}_i \rangle_I (E_\gamma) \, dE_\gamma. \tag{A.14}$$

The whole reason for doing this exercise is to get an integral expression for $\langle\Gamma_i\rangle_I$ in which we know the exact contents. Now, let us compare this with Eq. A.2:

$$\langle\Gamma_i\rangle_I = \int_0^{E_I} \frac{E_\gamma^3 f_{M1}(E_\gamma)}{\rho(E_I, J_I, \pi_i)} \sum_{J_f=J_I-1}^{J_I+1} \rho(E_i - E_\gamma, J_f, \pi_f)\, \mathrm{d}E_\gamma \qquad (A.15)$$

$$= \int_0^{E_I} \frac{E_\gamma^3 f_{M1}(E_\gamma)}{\rho(E_I, J_I, \pi_I)} \rho_f(E_i - E_\gamma)\, \mathrm{d}E_\gamma, \qquad (A.16)$$

where for brevity we have written $\sum_{I=J-1}^{J+1} \rho(E_i - E_\gamma, J_f, \pi_f) \equiv \rho_f(E_i - E_\gamma)$, the total level density of *accessible final states* for the decay. The two integrands must be equal, giving

$$\langle\tilde{\alpha}_i\rangle_I(E_\gamma) = \frac{E_\gamma^3 f_{M1}(E_\gamma)}{\rho(E_i, J_i, \pi_i)} \rho_f(E_i - E_\gamma). \qquad (A.17)$$

Solving for $f(E_\gamma)$ gives

$$f_{M1}(E_\gamma) = \frac{\langle\tilde{\alpha}_i\rangle_I(E_\gamma)\rho(E_i, J_i, \pi_i)}{E_\gamma^3 \rho_f(E_i - E_\gamma)}. \qquad (A.18)$$

Unwrapping the contents of $\langle\tilde{\alpha}_i\rangle_I(E_\gamma)$, this gives

$$f_{M1}(E_\gamma) = \frac{\rho(E_i, J_i, \pi_i)}{E_\gamma^3 \rho_f(E_i - E_\gamma)} \frac{1}{N_I} \sum_{i=1}^{N_I} \tilde{\alpha}_i(E_\gamma) \qquad (A.19)$$

$$= \frac{\rho(E_i, J_i, \pi_i)}{E_\gamma^3 \rho_f(E_i - E_\gamma)} \frac{1}{N_I} \sum_{i=1}^{N_I} \alpha_i(E_f = E_i - E_\gamma) \qquad (A.20)$$

$$= \frac{\rho(E_i, J_i, \pi_i)}{E_\gamma^3 \rho_f(E_i - E_\gamma)} \frac{1}{N_I} \sum_{i=1}^{N_I} \frac{1}{\Delta E_f} \sum_{f\in b(E_f)} \gamma_{i\to f}. \qquad (A.21)$$

The level density of final states, $\rho_f(E_f)$, is given by

$$\rho_f(E_f) = \frac{N_b}{\Delta E_f}, \qquad (A.22)$$

where N_b is the number of final states accessible to the decay, *i.e.* the number of states in the bin $b(E_f)$. This means that we can rewrite

$$\frac{1}{\Delta E_f} \sum_{f\in b(E_f)} \gamma_{i\to f} = \frac{\rho_f(E_f)}{N_b} \sum_{f\in b(E_f)} \gamma_{i\to f} = \rho_f(E_f)\langle\gamma_{i\to f}\rangle_{b(E_f)}, \qquad (A.23)$$

where $\langle\gamma_{i\to f}\rangle_{b(E_f)}$ is the arithmetic average of $\gamma_{i\to f}$ within the final state bin $b(E_f)$. Finally, this gives

$$f_{M1}(E_\gamma) = \frac{\rho(E_i, J_i, \pi_i)}{E_\gamma^3 \rho_f(E_i - E_\gamma)} \frac{1}{N_I} \sum_{i=1}^{N_I} \rho_f(E_f)\langle\gamma_{i\to f}\rangle_{b(E_f)} \qquad (A.24)$$

$$= \frac{\rho(E_i, J_i, \pi_i)}{E_\gamma^3} \left\langle\langle\gamma_{i\to f}\rangle_{b(E_f)}\right\rangle_I, \qquad (A.25)$$

where the average goes over both the initial and the final excitation energy bins,

$$\left\langle \langle \gamma_{i \to f} \rangle_{b(E_f)} \right\rangle_I = \frac{1}{N_I} \sum_{i=1}^{N_I} \frac{1}{N_b} \sum_{f \in b(E_f)} \gamma_{i \to f}. \tag{A.26}$$

Appendix B

Statistics

In this Appendix, I discuss some concepts in probability and statistical modelling relevant to the thesis.

B.1 Probability distributions and data

The *probability distribution* is fundamental to statistical modelling. For a (possibly vector-valued) stochastic variable X and a set of parameters θ, the probability distribution

$$p(x = X|\theta) \tag{B.1}$$

encodes the probability that a measurement (or draw, if you like) of X gives the value x, given the parameters θ. The distinction between x and X is usually suppressed by writing simply

$$p(x|\theta). \tag{B.2}$$

The probabilities for all different outcomes of x must by definition sum to unity, giving the normalisation requirement

$$\int p(x)\,\mathrm{d}x = 1 \tag{B.3}$$

The *expectation value* of a stochastic variable is defined as

$$\langle x \rangle = \int x p(x)\,\mathrm{d}x, \tag{B.4}$$

and it represents the average value of a large number of repeated trials. The *standard deviation*, a measure of how much the values spread out from the mean, is given by

$$\sigma = \sqrt{\langle (x - \langle x \rangle)^2 \rangle}. \tag{B.5}$$

The square of the standard deviation is known as the *variance*, $\mathrm{Var}[x] = \sigma^2$.

An example of a probability distribution that is relevant to this thesis is the Poisson distribution. It applies to 'counting experiments', where the number of measurements, n, that have an energy E falling in some given interval $[E_k, E_k + \Delta E]$ can be modelled as

$$p(n|\lambda) = \frac{\lambda^n e^{-\lambda}}{n!}. \tag{B.6}$$

The expected number of occurrences n given the Poisson distribution is $\langle n \rangle = \lambda$, and the standard deviation is $\sigma = \sqrt{\lambda}$.

B.2   Fitting a model to data

A situation that often arises is when we have a set of measurements $\{y_i\}$ that we want to model using some probability distribution $p(x|\theta)$. This means treating the y_i as independent outcomes that have already been drawn from $p(x|\theta)$. The reasons for doing this can be *e.g.* to estimate uncertainties in the data set or to use the resulting distribution to draw new values in a Monte Carlo scheme. The question is which set of parameter values θ_0 that best describe the data set $\{y_i\}$. Determining the best values, θ_0, is known as *fitting* the model.

When the measured values y_i are inserted into $p(x|\theta)$, the result $p(y_i|\theta)$ is no longer a probability distribution. It can however be treated as a function of θ, known as the *likelihood* function,

$$\mathcal{L}(\theta, y_i) \equiv p(y_i|\theta). \tag{B.7}$$

The likelihood function gives the probability of observing the data y_i given the parameter value θ. To estimate the value of θ_0 in a model fitting procedure, one often applies the principle of *maximum likelihood*, which says that the best parameter choice θ_0 is the one for which $\mathcal{L}(\theta, y_i)$ is maximised. In the case of the Poisson distribution, the likelihood function for the expected number of occurrences λ given a measured number of occurrences y is

$$\mathcal{L}(\theta, y) = \frac{\lambda^y e^{-\lambda}}{y!}, \tag{B.8}$$

and the maximum likelihood estimator (MLE) for λ is $\hat{\lambda} = y$. This is also an *unbiased* estimator for λ, since $\langle n \rangle = \lambda$.

Multiple measurements $\{y_i\}_{i=1}^{N}$ can be combined. If we assume them to be independently drawn from the same underlying distribution, then their joint distribution is the product of the probability distribution evaluated at each i,

$$p(\{x_i\}|\theta) = \prod_{i=1}^{N} p(x_i|\theta), \tag{B.9}$$

and the joint likelihood similarly is

$$\mathcal{L}(\theta, \{y_i\}) = \prod_{i=1}^{N} \mathcal{L}(\theta, y). \tag{B.10}$$

It is often convenient to work with the log-likelihood, $\ln \mathcal{L}$, instead. Since the logarithm is monotonic, most of the mathematical features, such as maxima and minima, are preserved under the logarithmic transformation. It also eases the construction of joint likelihoods, since

$$\ln \mathcal{L}(\theta, \{y_i\}) = \ln \prod_{i=1}^{N} \mathcal{L}(\theta, y_i) = \sum_{i=1}^{N} \ln \mathcal{L}(\theta, y_i). \tag{B.11}$$

B.2.1 χ^2 fitting

The method of χ^2 minimisation, also known as weighted least squares, is perhaps the most widely used method for fitting functions. In the Oslo method, as discussed in Chapter 4, a minimal-χ^2 fit is used to determine the functional form of the level density and γ-ray strength function by fitting them to the matrix $P(E_x, E_\gamma)$ of primary γ rays. To use a χ^2 fit, the data being fit should have Gaussian uncertainties. The Gaussian, or normal, distribution is often encountered in statistics, because it applies to a great number of common cases. It has a probability distribution function given by

$$p(x|\mu,\sigma) = \frac{1}{\sqrt{2\pi\sigma^2}} e^{-\frac{(x-\mu)^2}{2\sigma^2}}, \tag{B.12}$$

where μ is the expectation value and σ the standard deviation. In the case of the Oslo method, which comes from a counting experiment, the underlying distribution is the Poisson distribution. However, for sufficiently large λ, *i.e.*, sufficiently many events in each energy bin, the Poisson distribution closely resembles the normal distribution, enabling us to employ a χ^2 fit. Assuming that each E_x, E_γ bin of $P(E_x, E_\gamma)$ is a measurement from a normal distribution with known standard deviation $\sigma(E_x, E_\gamma)$, the likelihood on that bin for the fitting parameter $\mu = P_{\text{fit}}(E_x, E_\gamma)$ is

$$\mathcal{L} = \frac{1}{\sqrt{2\pi\sigma^2(E_x, E_\gamma)}} \exp\left(-\frac{(P_{\text{exp}}(E_x, E_\gamma) - P_{\text{fit}}(E_x, E_\gamma))^2}{2\sigma^2_{E_x,E_\gamma}}\right), \tag{B.13}$$

and the joint likelihood for the fit across all E_x, E_γ bins is found by taking the product. Taking the log-likelihood, this gives

$$\log \mathcal{L} = K - \sum_{E_x, E_\gamma} \left(-\frac{(P_{\text{exp}}(E_x, E_\gamma) - P_{\text{fit}}(E_x, E_\gamma))^2}{2\sigma^2_{E_x,E_\gamma}}\right) = K - \frac{1}{2}\chi^2, \tag{B.14}$$

where K is some constant, and where the joint χ^2 distribution of all the E_x, E_γ bins has been identified. This shows that the parameters that minimise the χ^2 are the maximum-likelihood estimates for the joint normal distribution [171].

B.3 Bayesian statistics

The discussion about maximum likelihood estimation in the previous sections falls within the category of *frequentist* statistics. A different statistical genre is that of Bayesianism, where one attempts to take prior knowledge about the problem into account [166]. Bayesian statistics springs from Bayes' theorem, which tells how to invert conditional probabilities:

$$p(a|b) = \frac{p(b|a)p(a)}{p(b)}. \tag{B.15}$$

Applying this to the case of fitting a set of parameters θ given data $\{y_i\}$, and renaming the functions, gives

$$p(\theta|\{y_i\}) = \frac{\mathcal{L}(\theta, \{y_i\})\pi(\theta)}{\mathcal{Z}(\{y_i\})}. \tag{B.16}$$

Here, $\mathcal{L}(\theta, \{y_i\})$ is again the likelihood function for θ given the data $\{y_i\}$, and $\pi(\theta)$ is the *prior* probability on θ before the data are considered. $\mathcal{Z}(\{y_i\})$ is the marginal probability distribution of the data independent of the parameters, and for our purposes here it serves simply as a normalisation constant that can be inferred from the other variables. The left-hand side $p(\theta|\{y_i\})$ is known as the *posterior* probability distribution of θ given the data $\{y_i\}$. The thing that sets Bayesian statistics apart is the need for a prior probability, which constitutes an assumption about the behaviour of the parameters θ before the data have been considered. This leads some critics to consider Bayesian statistics to involve too much subjectivity. And indeed, if one is not careful, it is possible to have the prior overshadow the likelihood, leading to a posterior distribution that is affected more by the prior assumptions than by data. However, the influence of the prior can be controlled by making sound choices for its distribution and monitoring the outcome of the fit.

Bayesian statistics has a number of appealing features. Fundamentally, it boils down to the fact that it supplies a full-fledged probability distribution for the parameter being estimated. This opens up for greater flexibility than what the point estimate of maximum-likelihood estimation offers. Bayesian statistics has gained popularity with the advent of modern computers, because it naturally lends itself to Monte Carlo methods: With an explicit expression for the posterior probability distribution $p(\theta|\{y_i\})$, it is possible to explore the parameter space of θ in an efficient way by emphasising regions of high posterior probability. This is especially important for problems with a large number of parameters, because the volume of the parameter space grows exponentially with the number of parameters, prohibiting more straight-forward methods such as sampling values on a grid.

Figure 4.9 in Chapter 4 demonstrates a Bayesian approach to the problem of normalisation in the Oslo method. The three transformation parameters A, α and B were fitted simultaneously to constraints from auxiliary data using the Python package PyMC3 [172]. The constraints were taken as the level density based on known individual levels below 900 keV and the γ-ray strength function measured in a (γ, n) experiment [167], extrapolated below the neutron separation energy by an exponential function. The Oslo-method γ-ray strength function was constrained by comparing with the extrapolation for E_γ between 5 and 7 MeV. The priors on A, α and B were taken to be uniform, to avoid biasing the posterior distribution. Figure B.1 shows the result of the fit. The left panels show the level density and γ-ray strength function before fitting, together with the regions used to constrain the fit. The slope and absolute values have been tuned by eye to match the data qualitatively. The panels on the right show the same data after the Bayesian fit. The points labeled best-fit correspond to the maximum a posteriori values of the parameters, *i.e.*,
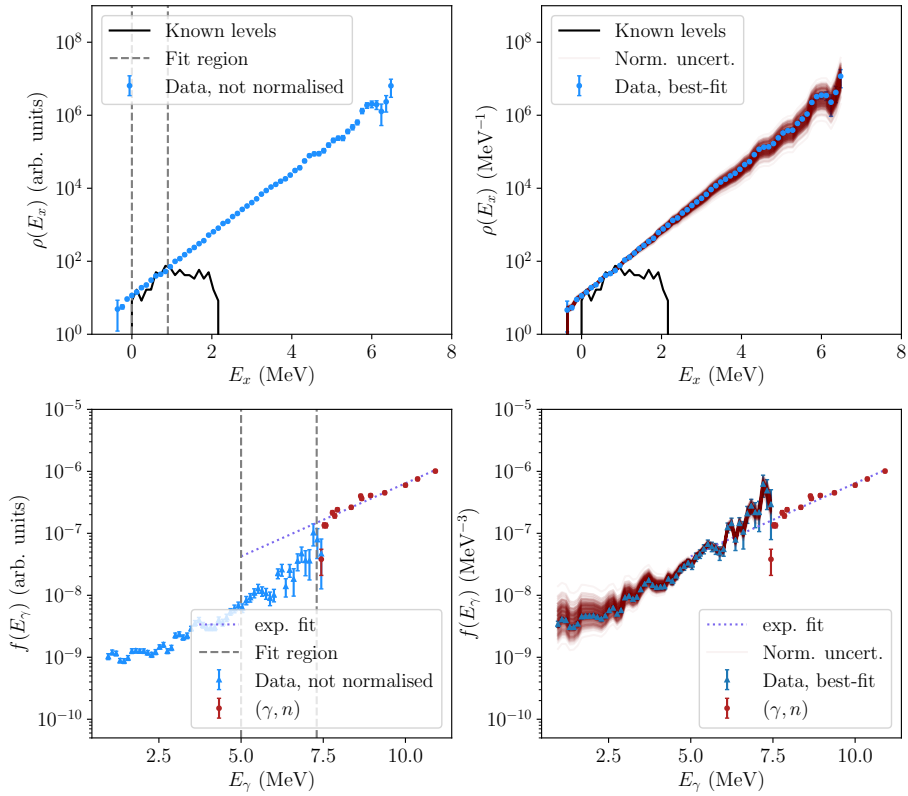
Figure B.1: Level density and γ-ray strength function normalised by a global Bayesian fit of the transformation parameters A, α and B to auxiliary data. The left panels show the unnormalised data, and the right panels show the results of the Bayesian fit. The data set used is from an OCL experiment on the reaction ^{184}W$(\alpha, p)^{187}$Re. See the text for details.

the parameter values that maximise the posterior probability. Note that in the case of uniform priors, the maximum a posteriori estimate is equal to the maximum likelihood estimate. The green bands show a representative sample from the posterior probability distribution of the parameters, and thus represent the uncertainty in the normalisation. The distribution nicely visualises how the data are most uncertain furthest away from the regions used in the fit.

The Bayesian approach to normalisation is flexible with regards to what auxiliary constraints are included in the likelihood. This versatility makes it attractive as a normalisation approach when the Oslo method is applied to more and more exotic nuclei, where normalisation data is scarce. It is also conceivable to combine the fit of ρ and $\mathcal{T}$ to the primary matrix and the normalisation into a single, global fit. This would be a rigorous statistical procedure to provide normalised functions with uncertainties, while avoiding the problems of χ^2 degeneracy with respect to the normalisation parameters A, B and α, as discussed in Paper V [145]. Performing such a global fit may however turn out to be a computational challenge.

Bibliography

[1]   E. M. Burbidge, G. R. Burbidge, W. A. Fowler and F. Hoyle, 'Synthesis of the Elements in Stars', *Reviews of Modern Physics*, vol. 29, no. 4, pp. 547–650, Oct. 1957. DOI: 10.1103/RevModPhys.29.547.

[2]   M. R. Drout, A. L. Piro, B. J. Shappee *et al.*, 'Light curves of the neutron star merger GW170817/SSS17a: Implications for r-process nucleosynthesis', *Science*, vol. 358, no. 6370, pp. 1570–1574, Dec. 2017. DOI: 10.1126/science.aaq0049.

[3]   M. Arnould, S. Goriely and K. Takahashi, 'The r-process of stellar nucleosynthesis: Astrophysics and nuclear physics achievements and mysteries', *Physics Reports*, vol. 450, no. 4, pp. 97–213, Sep. 2007. DOI: 10.1016/j.physrep.2007.06.002.

[4]   M. E. Peskin and D. V. Schroeder, *An Introduction to quantum field theory*, en. Reading, USA: Addison-Wesley, 1995.

[5]   T. A. Collaboration, G. Aad, E. Abat *et al.*, 'The ATLAS Experiment at the CERN Large Hadron Collider', *Journal of Instrumentation*, vol. 3, no. 08, S08003–S08003, Aug. 2008. DOI: 10.1088/1748-0221/3/08/S08003.

[6]   K. Miernik, *Chart of nuclides drawer*, Dec. 2018. [Online]. Available: https://github.com/kmiernik/Chart-of-nuclides-drawer (visited on 04/12/2018).

[7]   G. Audi, F. G. Kondev, M. Wang, W. Huang and S. Naimi, 'The NUBASE2016 evaluation of nuclear properties', *Chinese Physics C*, vol. 41, no. 3, p. 030 001, Mar. 2017. DOI: 10.1088/1674-1137/41/3/030001.

[8]   W. Nazarewicz, 'The limits of nuclear mass and charge', *Nature Physics*, vol. 14, no. 6, p. 537, Jun. 2018. DOI: 10.1038/s41567-018-0163-3.

[9]   Gamow G. and Rutherford Ernest, 'Mass defect curve and nuclear constitution', *Proceedings of the Royal Society of London. Series A, Containing Papers of a Mathematical and Physical Character*, vol. 126, no. 803, pp. 632–644, Mar. 1930. DOI: 10.1098/rspa.1930.0032.

[10] C. F. v. Weizsäcker, 'Zur Theorie der Kernmassen', *Zeitschrift für Physik*, vol. 96, no. 7, pp. 431–458, Jul. 1935. DOI: 10.1007/BF01337700.

[11] A. Bohr and B. R. Mottelson, *Nuclear Structure*, en. Singapore: World Scientific, 1998.

[12] N. Bohr and J. A. Wheeler, 'The Mechanism of Nuclear Fission', *Physical Review*, vol. 56, no. 5, pp. 426–450, Sep. 1939. DOI: 10.1103/PhysRev.56.426.

[13]   V. Somà, 'From the liquid drop model to lattice QCD', *The European Physical Journal Plus*, vol. 133, no. 10, p. 434, Oct. 2018. DOI: `10.1140/epjp/i2018-12244-2`.

[14]   M. G. Mayer, 'On Closed Shells in Nuclei', *Physical Review*, vol. 74, no. 3, pp. 235–239, Aug. 1948. DOI: `10.1103/PhysRev.74.235`.

[15]   M. G. Mayer, 'On Closed Shells in Nuclei. II', *Physical Review*, vol. 75, no. 12, pp. 1969–1970, Jun. 1949. DOI: `10.1103/PhysRev.75.1969`.

[16]   O. Haxel, J. H. D. Jensen and H. E. Suess, 'On the "Magic Numbers" in Nuclear Structure', *Physical Review*, vol. 75, no. 11, pp. 1766–1766, Jun. 1949. DOI: `10.1103/PhysRev.75.1766.2`.

[17]   *The Nobel Prize in Physics 1963*, en-US. [Online]. Available: `https://www.nobelprize.org/prizes/physics/1963/summary/` (visited on 01/02/2019).

[18]   Bakken, *Wikipedia: Nuclear shells and magic numbers in a harmonic oscillator with orbit–orbit and spin–orbit terms*, Feb. 2008. [Online]. Available: `https://commons.wikimedia.org/wiki/File:Shells.png` (visited on 18/03/2019).

[19]   D. J. Rowe and J. L. Wood, *Fundamentals of Nuclear Models: Foundational Models*, en. Singapore: World Scientific, 2010.

[20]   H. Grawe, K. Langanke and G. Martínez-Pinedo, 'Nuclear structure and astrophysics', *Reports on Progress in Physics*, vol. 70, no. 9, pp. 1525–1582, Sep. 2007. DOI: `10.1088/0034-4885/70/9/R02`.

[21]   K. S. Krane, *Introductory Nuclear Physics, 3rd Edition*, en. Hoboken, New Jersey, United States: John Wiley & Sons, Inc., 1987.

[22]   J. M. Blatt and V. F. Weisskopf, *Theoretical Nuclear Physics*, en. New York, NY: Springer New York, 1979. DOI: `10.1007/978-1-4612-9959-2`.

[23]   M. Hjorth-Jensen, *Lecture notes for PHY 981 Nuclear Structure at Michigan State University*, en, East Lansing, Michigan, USA, 2016. [Online]. Available: `https://github.com/NuclearStructure/PHY981` (visited on 06/05/2019).

[24]   J. Suhonen, *From Nucleons to Nucleus: Concepts of Microscopic Nuclear Theory*, en, ser. Theoretical and Mathematical Physics. Berlin Heidelberg: Springer-Verlag, 2007.

[25]   I. Shavitt, 'The history and evolution of configuration interaction', *Molecular Physics*, vol. 94, no. 1, pp. 3–17, May 1998. DOI: `10.1080/002689798168303`.

[26]   E. Caurier, G. Martínez-Pinedo, F. Nowacki, A. Poves and A. P. Zuker, 'The shell model as a unified view of nuclear structure', *Reviews of Modern Physics*, vol. 77, no. 2, pp. 427–488, Jun. 2005. DOI: `10.1103/RevModPhys.77.427`.

[27] J. E. Midtbø, A. C. Larsen, T. Renstrøm, F. L. Bello Garrote and E. Lima, 'Consolidating the concept of low-energy magnetic dipole decay radiation', *Physical Review C*, vol. 98, no. 6, p. 064 321, Dec. 2018. DOI: `10.1103/PhysRevC.98.064321`.

[28] B. A. Brown, 'The nuclear shell model towards the drip lines', *Progress in Particle and Nuclear Physics*, vol. 47, no. 2, pp. 517–599, Jan. 2001. DOI: `10.1016/S0146-6410(01)00159-4`.

[29] T. Otsuka, M. Honma, T. Mizusaki, N. Shimizu and Y. Utsuno, 'Monte Carlo shell model for atomic nuclei', *Progress in Particle and Nuclear Physics*, vol. 47, no. 1, pp. 319–400, Jan. 2001. DOI: `10.1016/S0146-6410(01)00157-0`.

[30] D. C. Zheng, B. R. Barrett, L. Jaqua, J. P. Vary and R. J. McCarthy, 'Microscopic calculations of the spectra of light nuclei', *Physical Review C*, vol. 48, no. 3, pp. 1083–1091, Sep. 1993. DOI: `10.1103/PhysRevC.48.1083`.

[31] S. E. Koonin, D. J. Dean and K. Langanke, 'Shell model Monte Carlo methods', *Physics Reports*, vol. 278, no. 1, pp. 1–77, Jan. 1997. DOI: `10.1016/S0370-1573(96)00017-8`.

[32] C. Stumpf, J. Braun and R. Roth, 'Importance-truncated large-scale shell model', *Physical Review C*, vol. 93, no. 2, p. 021 301, Feb. 2016. DOI: `10.1103/PhysRevC.93.021301`.

[33] C. Bahri and D. J. Rowe, 'SU 3 quasi-dynamical symmetry as an organizational mechanism for generating nuclear rotational motions', *Nuclear Physics A*, vol. 66260, no. 21, pp. 125–14 760, 2000. DOI: `10.1016/S0375-9474(99)00394-2`.

[34] T. Dytrych, K. D. Launey, J. P. Draayer, D. Rowe, J. Wood, G. Rosensteel, C. Bahri, D. Langr and R. B. Baker, 'Physics of nuclei: Key role of an emergent symmetry', *arXiv:1810.05757 [nucl-th]*, Oct. 2018. arXiv: `1810.05757`.

[35] N. Shimizu, Y. Utsuno, Y. Futamura, T. Sakurai, T. Mizusaki and T. Otsuka, 'Stochastic estimation of nuclear level density in the nuclear shell model: An application to parity-dependent level density in 58ni', *Physics Letters, Section B: Nuclear, Elementary Particle and High-Energy Physics*, vol. 753, pp. 13–17, 2016. DOI: `10.1016/j.physletb.2015.12.005`.

[36] M. Horoi and V. Zelevinsky, 'Random interactions explore the nuclear landscape: Predominance of prolate nuclear deformations', *Physical Review C*, vol. 81, no. 3, p. 034 306, 2010. DOI: `10.1103/PhysRevC.81.034306`.

[37] G. P. Lepage, 'Lattice QCD for Novices', *arXiv:hep-lat/0506036*, Jun. 2005. arXiv: `hep-lat/0506036`.

[38] E. Epelbaum, H.-W. Hammer and U.-G. Meißner, 'Modern theory of nuclear forces', *Reviews of Modern Physics*, vol. 81, no. 4, pp. 1773–1825, Dec. 2009. DOI: `10.1103/RevModPhys.81.1773`.

167

[39] M. Hjorth-Jensen, T. T. Kuo and E. Osnes, 'Realistic effective interactions for nuclear systems', *Physics Reports*, vol. 261, no. 3-4, pp. 125–270, Oct. 1995. DOI: `10.1016/0370-1573(95)00012-6`.

[40] N. Tsunoda, T. Otsuka, N. Shimizu, M. Hjorth-Jensen, K. Takayanagi and T. Suzuki, 'Exotic neutron-rich medium-mass nuclei with realistic nuclear forces', *Phys. Rev. C*, vol. 95, p. 021 304, 2 Feb. 2017. DOI: `10.1103/PhysRevC.95.021304`.

[41] B. A. Brown and W. A. Richter, 'New "USD" Hamiltonians for the sd shell', *Physical Review C*, vol. 74, no. 3, p. 034 315, 2006. DOI: `10.1103/PhysRevC.74.034315`.

[42] M. Honma, B. A. Brown, T. Mizusaki and T. Otsuka, 'Full pf-shell calculations with a new effective interaction', *Nuclear Physics A*, vol. 704, no. 1-4, pp. 134C–143C, Jun. 2002. DOI: `10.1016/S0375-9474(02)00774-1`.

[43] A. F. Lisetskiy, B. A. Brown, M. Horoi and H. Grawe, 'New $T = 1$ effective interactions for the $f_{5/2}p_{3/2}p_{1/2}g_{9/2}$ model space: Implications for valence-mirror symmetry and seniority isomers', *Physical Review C*, vol. 70, no. 4, p. 044 314, Oct. 2004. DOI: `10.1103/PhysRevC.70.044314`.

[44] D. J. Griffiths and D. F. Schroeter, *Introduction to Quantum Mechanics*, en. Cambridge: Cambridge University Press, 2018.

[45] N. Shimizu, 'Nuclear shell-model code for massive parallel computation, "KSHELL"', *arXiv:1310.5431 [nucl-th]*, Oct. 2013. arXiv: `1310.5431`.

[46] S. Barr, *Fram - polarskute, Store norske leksikon*, 2017. [Online]. Available: `https://snl.no/Fram_-_polarskute` (visited on 10/04/2019).

[47] *Fram | Sigma2*. [Online]. Available: `https://www.sigma2.no/Fram` (visited on 22/03/2019).

[48] C. W. Johnson, W. E. Ormand and P. G. Krastev, 'Factorization in large-scale many-body calculations', *Computer Physics Communications*, vol. 184, no. 12, pp. 2761–2774, 2013. DOI: `https://doi.org/10.1016/j.cpc.2013.07.022`.

[49] C. Lanczos, 'An iteration method for the solution of the eigenvalue problem of linear differential and integral operators', *Journal of Research of the National Bureau of Standards*, vol. 45, no. 4, p. 255, Oct. 1950. DOI: `10.6028/jres.045.026`.

[50] K. Wu and H. Simon, 'Thick-Restart Lanczos Method for Large Symmetric Eigenvalue Problems', *SIAM Journal on Matrix Analysis and Applications*, vol. 22, no. 2, pp. 602–616, 2000. DOI: `10.1137/S0895479898334605`.

[51] B. Wildenthal, 'Empirical strengths of spin operators in nuclei', *Progress in Particle and Nuclear Physics*, vol. 11, pp. 5–51, 1984. DOI: `10.1016/0146-6410(84)90011-5`.

[52]   T. Hastie, R. Tibshirani and J. Friedman, *The Elements of Statistical Learning*, en, 2nd edition, ser. Springer Series in Statistics. Springer Berlin Heidelberg, 2009.

[53]   M. Honma, T. Otsuka, B. A. Brown and T. Mizusaki, 'Shell-model description of neutron-rich pf-shell nuclei with a new effective interaction GXPF 1', *The European Physical Journal A - Hadrons and Nuclei*, vol. 25, no. 1, pp. 499–502, Sep. 2005. DOI: `10.1140/epjad/i2005-06-032-2`.

[54]   T. Renstrøm, G. M. Tveten, J. E. Midtbø *et al.*, 'Experimental γ-decay strength in ^{59,60}Ni compared with microscopic calculations', *arXiv:1804.08086 [nucl-ex]*, Apr. 2018. arXiv: `1804.08086`.

[55]   Y. Utsuno, T. Otsuka, B. A. Brown, M. Honma, T. Mizusaki and N. Shimizu, 'Shape transitions in exotic Si and S isotopes and tensor-force-driven Jahn-Teller effect', *Physical Review C*, vol. 86, no. 5, p. 051 301, Nov. 2012. DOI: `10.1103/PhysRevC.86.051301`.

[56]   T. Otsuka, T. Suzuki, M. Honma, Y. Utsuno, N. Tsunoda, K. Tsukiyama and M. Hjorth-Jensen, 'Novel Features of Nuclear Forces and Shell Evolution in Exotic Nuclei', *Physical Review Letters*, vol. 104, no. 1, p. 012 501, Jan. 2010. DOI: `10.1103/PhysRevLett.104.012501`.

[57]   M. Honma, T. Otsuka, T. Mizusaki and M. Hjorth-Jensen, 'New effective interaction for f_5pg_9-shell nuclei', *Physical Review C*, vol. 80, no. 6, p. 064 323, Dec. 2009. DOI: `10.1103/PhysRevC.80.064323`.

[58]   B. A. Brown and W. D. M. Rae, 'The Shell-Model Code NuShellX@MSU', *Nuclear Data Sheets*, vol. 120, pp. 115–118, 2014. DOI: `https://doi.org/10.1016/j.nds.2014.07.022`.

[59]   A. C. Larsen, J. E. Midtbø, M. Guttormsen *et al.*, 'Enhanced low-energy γ-decay strength of 70Ni and its robustness within the shell model', *Phys. Rev. C*, vol. 97, p. 054 329, 5 May 2018. DOI: `10.1103/PhysRevC.97.054329`.

[60]   R. Shankar, *Principles of Quantum Mechanics*, en, 2nd ed. Springer US, 1994.

[61]   H. A. Weidenmuller and G. E. Mitchell, 'Random Matrices and Chaos in Nuclear Physics', *Nature*, vol. 6021, p. 54, 2008. DOI: `10.1103/RevModPhys.81.539`.

[62]   T. Ericson, 'A statistical analysis of excited nuclear states', *Nuclear Physics*, vol. 11, pp. 481–491, May 1959. DOI: `10.1016/0029-5582(59)90291-3`.

[63]   T. Ericson, 'Fluctuations of Nuclear Cross Sections in the "Continuum" Region', *Physical Review Letters*, vol. 5, no. 9, pp. 430–431, Nov. 1960. DOI: `10.1103/PhysRevLett.5.430`.

[64]   A. Gilbert and A. G. W. Cameron, 'A composite nuclear-level density formula with shell corrections', *Canadian Journal of Physics*, vol. 43, no. 8, pp. 1446–1496, Aug. 1965. DOI: `10.1139/p65-139`.

[65]   H. A. Bethe, 'An Attempt to Calculate the Number of Energy Levels of a Heavy Nucleus', *Physical Review*, vol. 50, no. 4, pp. 332–341, Aug. 1936. DOI: `10.1103/PhysRev.50.332`.

[66]   T. von Egidy and D. Bucurescu, 'Statistical nuclear properties (level densities, spin distributions)', *J. Phys.: Conf. Ser*, vol. 338, p. 012 028, 2012.

[67]   T. v. Egidy and D. Bucurescu, 'Systematics of nuclear level density parameters', *Physical Review C*, vol. 72, no. 4, p. 044 311, Oct. 2005. DOI: `10.1103/PhysRevC.72.044311`.

[68]   ——, 'Erratum: Systematics of nuclear level density parameters [Phys. Rev. C 72, 044311 (2005)]', *Physical Review C*, vol. 73, no. 4, p. 049 901, Apr. 2006. DOI: `10.1103/PhysRevC.73.049901`.

[69]   M. Guttormsen, S. Goriely, A. C. Larsen, A. Görgen, T. W. Hagen, T. Renstrøm, S. Siem, N. U. H. Syed, G. Tagliente, H. K. Toft, H. Utsunomiya, A. V. Voinov and K. Wikan, 'Quasicontinuum γ decay of $91, 92\mathbf{Zr}$: Benchmarking indirect (n, γ) cross section measurements for the s process', *Physical Review C*, vol. 96, no. 2, p. 024 313, Aug. 2017. DOI: `10.1103/PhysRevC.96.024313`.

[70]   T. von Egidy and D. Bucurescu, 'Experimental energy-dependent nuclear spin distributions', *Physical Review C*, vol. 80, no. 5, p. 054 310, Nov. 2009. DOI: `10.1103/PhysRevC.80.054310`.

[71]   S. M. Grimes, J. D. Anderson, J. W. McClure, B. A. Pohl and C. Wong, 'Level density and spin cutoff parameters from continuum (p, n) and (α, n) spectra', *Physical Review C*, vol. 10, no. 6, pp. 2373–2386, Dec. 1974. DOI: `10.1103/PhysRevC.10.2373`.

[72]   S. Goriely, S. Hilaire and A. J. Koning, 'Improved microscopic nuclear level densities within the Hartree-Fock-Bogoliubov plus combinatorial method', *Physical Review C*, vol. 78, no. 6, p. 064 307, Dec. 2008. DOI: `10.1103/PhysRevC.78.064307`.

[73]   G. A. Bartholomew, E. D. Earle, A. J. Ferguson, J. W. Knowles and M. A. Lone, 'Gamma-Ray Strength Functions', en, in *Advances in Nuclear Physics: Volume 7*, M. Baranger and E. Vogt, Eds., Boston, MA: Springer US, 1973, pp. 229–324. DOI: `10.1007/978-1-4615-9044-6_4`.

[74]   C. E. Porter and R. G. Thomas, 'Fluctuations of nuclear reaction widths', *Phys. Rev.*, vol. 104, pp. 483–491, 2 Oct. 1956. DOI: `10.1103/PhysRev.104.483`.

[75]   L. E. Kirsch and L. A. Bernstein, 'RAINIER: A simulation tool for distributions of excited nuclear states and cascade fluctuations', *Nuclear Instruments and Methods in Physics Research Section A: Accelerators, Spectrometers, Detectors and Associated Equipment*, vol. 892, pp. 30–40, Jun. 2018. DOI: `10.1016/j.nima.2018.02.096`.

[76]   E. P. Wigner, 'Characteristic Vectors of Bordered Matrices With Infinite Dimensions', *Annals of Mathematics*, vol. 62, no. 3, pp. 548–564, 1955. DOI: `10.2307/1970079`.

[77]   A. Hamoudi, R. G. Nazmitdinov, E. Shahaliev and Y. Alhassid, 'Statistical fluctuations of electromagnetic transition intensities and electromagnetic moments in pf-shell nuclei', *Physical Review C*, vol. 65, no. 6, p. 064 311, Jun. 2002. DOI: `10.1103/PhysRevC.65.064311`.

[78]   V. Zelevinsky, B. A. Brown, N. Frazier and M. Horoi, 'The nuclear shell model as a testing ground for many-body quantum chaos', *Physics Reports*, vol. 276, no. 2, pp. 85–176, Nov. 1996. DOI: `10.1016/S0370-1573(96)00007-5`.

[79]   D. M. Brink, (unpublished), Doctoral thesis, Oxford, 1955.

[80]   P. Axel, 'Electric Dipole Ground-State Transition Width Strength Function and 7-Mev Photon Interactions', *Physical Review*, vol. 126, no. 2, pp. 671–683, Apr. 1962. DOI: `10.1103/PhysRev.126.671`.

[81]   F. Bečvář, P. Cejnar, R. E. Chrien and J. Kopecký, 'Test of photon strength functions by a method of two-step cascades', *Physical Review C*, vol. 46, no. 4, pp. 1276–1287, Oct. 1992. DOI: `10.1103/PhysRevC.46.1276`.

[82]   M. Krtička, F. Bečvář, J. Honzátko, I. Tomandl, M. Heil, F. Käppeler, R. Reifarth, F. Voss and K. Wisshak, 'Evidence for $M1$ Scissors Resonances Built on the Levels in the Quasicontinuum of ^{163}Dy', *Physical Review Letters*, vol. 92, no. 17, p. 172 501, Apr. 2004. DOI: `10.1103/PhysRevLett.92.172501`.

[83]   J. Kopecky and R. E. Chrien, 'Observation of the M1 giant resonance by resonance averaging in ^{106}Pd', *Nuclear Physics A*, vol. 468, no. 2, pp. 285–300, Jun. 1987. DOI: `10.1016/0375-9474(87)90518-5`.

[84]   C. W. Johnson, 'Systematics of strength function sum rules', *Physics Letters B*, vol. 750, pp. 72–75, Nov. 2015. DOI: `10.1016/j.physletb.2015.08.054`.

[85]   M. Guttormsen, A. C. Larsen, A. Görgen, T. Renstrøm, S. Siem, T. G. Tornyi and G. M. Tveten, 'Validity of the Generalized Brink-Axel Hypothesis in Np 238', *Physical Review Letters*, vol. 116, no. 1, p. 012 502, 2016. DOI: `10.1103/PhysRevLett.116.012502`.

[86]   L. Crespo Campo, M. Guttormsen, F. L. Bello Garrote, T. K. Eriksen, F. Giacoppo, A. Görgen, K. Hadynska-Klek, M. Klintefjord, A. C. Larsen, T. Renstrøm, E. Sahin, S. Siem, A. Springer, T. G. Tornyi and G. M. Tveten, 'Test of the generalized Brink-Axel hypothesis in ^{64,65}Ni', *Phys. Rev. C*, vol. 98, p. 054 303, 5 Nov. 2018. DOI: `10.1103/PhysRevC.98.054303`.

[87]   A. C. Larsen, M. Guttormsen, N. Blasi *et al.*, 'Low-energy enhance-ment and fluctuations of γ-ray strength functions in ^{56,57}Fe: test of the Brink–Axel hypothesis', *Journal of Physics G: Nuclear and Particle Physics*, vol. 44, no. 6, p. 064 005, 2017. DOI: `10.1088/1361-6471/aa644a`.

[88]   S. S. Dietrich and B. L. Berman, 'Atlas of photoneutron cross sections obtained with monoenergetic photons', *Atomic Data and Nuclear Data Tables*, vol. 38, no. 2, pp. 199–338, Mar. 1988. DOI: `10.1016/0092-640X(88)90033-2`.

[89]   G. E. Brown, *Unified Theory of Nuclear Models and Forces*, en. Amster-dam: North Holland Publishing Company, 1967.

[90]   R. Capote, M. Herman, P. Obložinský *et al.*, 'RIPL – Reference Input Parameter Library for Calculation of Nuclear Reactions and Nuclear Data Evaluations', *Nuclear Data Sheets*, Special Issue on Nuclear Re-action Data, vol. 110, no. 12, pp. 3107–3214, Dec. 2009. DOI: `10.1016/j.nds.2009.10.004`.

[91]   D. Savran, T. Aumann and A. Zilges, 'Experimental studies of the Pygmy Dipole Resonance', *Progress in Particle and Nuclear Physics*, vol. 70, pp. 210–245, 2013. DOI: `10.1016/j.ppnp.2013.02.003`.

[92]   K. Heyde, P. Von Neumann-Cosel and A. Richter, 'Magnetic dipole ex-citations in nuclei: Elementary modes of nucleonic motion', *Reviews of Modern Physics*, vol. 82, no. 3, pp. 2365–2419, 2010. DOI: `10.1103/RevModPhys.82.2365`.

[93]   A. Schiller, A. Voinov, E. Algin, J. A. Becker, L. A. Bernstein, P. E. Garrett, M. Guttormsen, R. O. Nelson, J. Rekstad and S. Siem, 'Low-energy M1 excitation mode in ^{172}Yb', *Physics Letters B*, vol. 633, no. 2, pp. 225–230, Feb. 2006. DOI: `10.1016/j.physletb.2005.12.043`.

[94]   A. Voinov, E. Algin, U. Agvaanluvsan, T. Belgya, R. Chankova, M. Gut-tormsen, G. E. Mitchell, J. Rekstad, A. Schiller and S. Siem, 'Large Enhancement of Radiative Strength for Soft Transitions in the Quasicon-tinuum', *Physical Review Letters*, vol. 93, no. 14, p. 142 504, Sep. 2004. DOI: `10.1103/PhysRevLett.93.142504`.

[95]   M. Krtička, F. Bečvář, I. Tomandl, G. Rusev, U. Agvaanluvsan and G. E. Mitchell, 'Two-step γ cascades following thermal neutron capture in ^{95}Mo', *Physical Review C*, vol. 77, no. 5, p. 054 319, May 2008. DOI: `10.1103/PhysRevC.77.054319`.

[96]   M. Wiedeking, L. A. Bernstein, M. Krtička, D. L. Bleuel, J. M. Allmond, M. S. Basunia, J. T. Burke, P. Fallon, R. B. Firestone, B. L. Goldblum, R. Hatarik, P. T. Lake, I.-Y. Lee, S. R. Lesher, S. Paschalis, M. Petri, L. Phair and N. D. Scielzo, 'Low-Energy Enhancement in the Photon Strength of ^{95}Mo', *Physical Review Letters*, vol. 108, no. 16, p. 162 503, Apr. 2012. DOI: `10.1103/PhysRevLett.108.162503`.

[97]   M. D. Jones, A. O. Macchiavelli, M. Wiedeking *et al.*, 'Examination of the low-energy enhancement of the γ-ray strength function of ^{56}Fe', *Physical Review C*, vol. 97, no. 2, p. 024 327, Feb. 2018. DOI: `10.1103/PhysRevC.97.024327`.

[98]   M. Guttormsen, R. Chankova, U. Agvaanluvsan, E. Algin, L. A. Bernstein, F. Ingebretsen, T. Lönnroth, S. Messelt, G. E. Mitchell, J. Rekstad, A. Schiller, S. Siem, A. C. Sunde, A. Voinov and S. Ødegård, 'Radiative strength functions in $^{93-98}$Mo', *Physical Review C*, vol. 71, no. 4, p. 044 307, Apr. 2005. DOI: `10.1103/PhysRevC.71.044307`.

[99]   A. Simon, M. Guttormsen, A. C. Larsen, C. W. Beausang, P. Humby, J. T. Burke, R. J. Casperson, R. O. Hughes, T. J. Ross, J. M. Allmond, R. Chyzh, M. Dag, J. Koglin, E. McCleskey, M. McCleskey, S. Ota and A. Saastamoinen, 'First observation of low-energy γ-ray enhancement in the rare-earth region', *Physical Review C*, vol. 93, no. 3, p. 034 303, Mar. 2016. DOI: `10.1103/PhysRevC.93.034303`.

[100]   H. Utsunomiya, T. Renstrøm, G. M. Tveten *et al.*, 'Photoneutron cross sections for Ni isotopes: Toward understanding (n, γ) cross sections relevant to weak *s*-process nucleosynthesis', *Physical Review C*, vol. 98, no. 5, p. 054 619, Nov. 2018. DOI: `10.1103/PhysRevC.98.054619`.

[101]   R. Schwengner, S. Frauendorf and B. A. Brown, 'Low-Energy Magnetic Dipole Radiation in Open-Shell Nuclei', *Physical Review Letters*, vol. 118, no. 9, p. 092 502, Mar. 2017. DOI: `10.1103/PhysRevLett.118.092502`.

[102]   A. C. Larsen, N. Blasi, A. Bracco, F. Camera, T. K. Eriksen, A. Görgen, M. Guttormsen, T. W. Hagen, S. Leoni, B. Million, H. T. Nyhus, T. Renstrøm, S. J. Rose, I. E. Ruud, S. Siem, T. Tornyi, G. M. Tveten, A. V. Voinov and M. Wiedeking, 'Evidence for the Dipole Nature of the Low-Energy γ Enhancement in ^{56}Fe', *Physical Review Letters*, vol. 111, no. 24, p. 242 504, Dec. 2013. DOI: `10.1103/PhysRevLett.111.242504`.

[103]   A. Voinov, M. Guttormsen, E. Melby, J. Rekstad, A. Schiller and S. Siem, 'γ-ray strength function and pygmy resonance in rare earth nuclei', *Physical Review C*, vol. 63, no. 4, p. 044 313, Mar. 2001. DOI: `10.1103/PhysRevC.63.044313`.

[104]   E. Melby, M. Guttormsen, J. Rekstad, A. Schiller, S. Siem and A. Voinov, 'Thermal and electromagnetic properties of ^{166}Er and ^{167}Er', *Physical Review C*, vol. 63, no. 4, p. 044 309, Mar. 2001. DOI: `10.1103/PhysRevC.63.044309`.

[105]   S. Siem, M. Guttormsen, K. Ingeberg, E. Melby, J. Rekstad, A. Schiller and A. Voinov, 'Level densities and γ-strength functions in ^{148,149}Sm', *Physical Review C*, vol. 65, no. 4, p. 044 318, Mar. 2002. DOI: `10.1103/PhysRevC.65.044318`.

[106]   M. Guttormsen, A. Bagheri, R. Chankova, J. Rekstad, S. Siem, A. Schiller and A. Voinov, 'Thermal properties and radiative strengths in ^{160,161,162}Dy', *Physical Review C*, vol. 68, no. 6, p. 064 306, Dec. 2003. DOI: `10.1103/PhysRevC.68.064306`.

[107]   U. Agvaanluvsan, A. Schiller, J. A. Becker, L. A. Bernstein, P. E. Garrett, M. Guttormsen, G. E. Mitchell, J. Rekstad, S. Siem, A. Voinov and W. Younes, 'Level densities and γ-ray strength functions in ^{170,171,172}Yb', *Physical Review C*, vol. 70, no. 5, p. 054 611, Nov. 2004. DOI: `10.1103/PhysRevC.70.054611`.

[108]   A. C. Larsen, R. Chankova, M. Guttormsen, F. Ingebretsen, S. Messelt, J. Rekstad, S. Siem, N. U. H. Syed, S. W. Ødegård, T. Lönnroth, A. Schiller and A. Voinov, 'Microcanonical entropies and radiative strength functions of ^{50,51}V', *Physical Review C*, vol. 73, no. 6, p. 064 301, Jun. 2006. DOI: `10.1103/PhysRevC.73.064301`.

[109]   A. C. Larsen, M. Guttormsen, R. Chankova, F. Ingebretsen, T. Lönnroth, S. Messelt, J. Rekstad, A. Schiller, S. Siem, N. U. H. Syed and A. Voinov, 'Nuclear level densities and γ-ray strength functions in ^{44,45}Sc', *Physical Review C*, vol. 76, no. 4, p. 044 303, Oct. 2007. DOI: `10.1103/PhysRevC.76.044303`.

[110]   E. Algin, U. Agvaanluvsan, M. Guttormsen, A. C. Larsen, G. E. Mitchell, J. Rekstad, A. Schiller, S. Siem and A. Voinov, 'Thermodynamic properties of ^{56,57}Fe', *Physical Review C*, vol. 78, no. 5, p. 054 321, Nov. 2008. DOI: `10.1103/PhysRevC.78.054321`.

[111]   N. U. H. Syed, M. Guttormsen, F. Ingebretsen, A. C. Larsen, T. Lönnroth, J. Rekstad, A. Schiller, S. Siem and A. Voinov, 'Level density and γ-decay properties of closed shell Pb nuclei', *Physical Review C*, vol. 79, no. 2, p. 024 316, Feb. 2009. DOI: `10.1103/PhysRevC.79.024316`.

[112]   N. U. H. Syed, A. C. Larsen, A. Bürger, M. Guttormsen, S. Harissopulos, M. Kmiecik, T. Konstantinopoulos, M. Krtička, A. Lagoyannis, T. Lönnroth, K. Mazurek, M. Norby, H. T. Nyhus, G. Perdikakis, S. Siem and A. Spyrou, 'Extraction of thermal and electromagnetic properties in ^{45}Ti', *Physical Review C*, vol. 80, no. 4, p. 044 309, Oct. 2009. DOI: `10.1103/PhysRevC.80.044309`.

[113]   H. T. Nyhus, S. Siem, M. Guttormsen, A. C. Larsen, A. Bürger, N. U. H. Syed, G. M. Tveten and A. Voinov, 'Radiative strength functions in 163, 164Dy', *Physical Review C*, vol. 81, no. 2, p. 024 325, Feb. 2010. DOI: `10.1103/PhysRevC.81.024325`.

[114]   H. K. Toft, A. C. Larsen, U. Agvaanluvsan, A. Bürger, M. Guttormsen, G. E. Mitchell, H. T. Nyhus, A. Schiller, S. Siem, N. U. H. Syed and A. Voinov, 'Level densities and γ-ray strength functions in Sn isotopes', *Physical Review C*, vol. 81, no. 6, p. 064 311, Jun. 2010. DOI: `10.1103/PhysRevC.81.064311`.

[115] M. Guttormsen, A. C. Larsen, A. Bürger *et al.*, 'Fermi's golden rule applied to the γ decay in the quasicontinuum of ^{46}Ti', *Physical Review C*, vol. 83, no. 1, p. 014 312, Jan. 2011. DOI: `10.1103/PhysRevC.83.014312`.

[116] H. K. Toft, A. C. Larsen, A. Bürger, M. Guttormsen, A. Görgen, H. T. Nyhus, T. Renstrøm, S. Siem, G. M. Tveten and A. Voinov, 'Evolution of the pygmy dipole resonance in Sn isotopes', *Physical Review C*, vol. 83, no. 4, p. 044 320, Apr. 2011. DOI: `10.1103/PhysRevC.83.044320`.

[117] A. Bürger, A. C. Larsen, S. Hilaire, M. Guttormsen, S. Harissopulos, M. Kmiecik, T. Konstantinopoulos, M. Krtička, A. Lagoyannis, T. Lönnroth, K. Mazurek, M. Norrby, H. T. Nyhus, G. Perdikakis, S. Siem, A. Spyrou and N. U. H. Syed, 'Nuclear level density and γ-ray strength function of ^{43}Sc', *Physical Review C*, vol. 85, no. 6, p. 064 328, Jun. 2012. DOI: `10.1103/PhysRevC.85.064328`.

[118] A. C. Larsen, I. E. Ruud, A. Bürger, S. Goriely, M. Guttormsen, A. Görgen, T. W. Hagen, S. Harissopulos, H. T. Nyhus, T. Renstrøm, A. Schiller, S. Siem, G. M. Tveten, A. Voinov and M. Wiedeking, 'Transitional γ strength in Cd isotopes', *Physical Review C*, vol. 87, no. 1, p. 014 319, Jan. 2013. DOI: `10.1103/PhysRevC.87.014319`.

[119] M. Guttormsen, L. A. Bernstein, A. Görgen, B. Jurado, S. Siem, M. Aiche, Q. Ducasse, F. Giacoppo, F. Gunsing, T. W. Hagen, A. C. Larsen, M. Lebois, B. Leniau, T. Renstrøm, S. J. Rose, T. G. Tornyi, G. M. Tveten, M. Wiedeking and J. N. Wilson, 'Scissors resonance in the quasicontinuum of Th, Pa, and U isotopes', *Physical Review C*, vol. 89, no. 1, p. 014 302, Jan. 2014. DOI: `10.1103/PhysRevC.89.014302`.

[120] H. Utsunomiya, S. Goriely, T. Kondo, C. Iwamoto, H. Akimune, T. Yamagata, H. Toyokawa, H. Harada, F. Kitatani, Y.-W. Lui, A. C. Larsen, M. Guttormsen, P. E. Koehler, S. Hilaire, S. Péru, M. Martini and A. J. Koning, 'Photoneutron cross sections for Mo isotopes: A step toward a unified understanding of (γ, n) and (n, γ) reactions', *Physical Review C*, vol. 88, no. 1, p. 015 805, Jul. 2013. DOI: `10.1103/PhysRevC.88.015805`.

[121] T. K. Eriksen, H. T. Nyhus, M. Guttormsen, A. Görgen, A. C. Larsen, T. Renstrøm, I. E. Ruud, S. Siem, H. K. Toft, G. M. Tveten and J. N. Wilson, 'Pygmy resonance and low-energy enhancement in the γ-ray strength functions of Pd isotopes', *Physical Review C*, vol. 90, no. 4, p. 044 311, Oct. 2014. DOI: `10.1103/PhysRevC.90.044311`.

[122] B. V. Kheswa, M. Wiedeking, F. Giacoppo, S. Goriely, M. Guttormsen, A. C. Larsen, F. L. Bello Garrote, T. K. Eriksen, A. Görgen, T. W. Hagen, P. E. Koehler, M. Klintefjord, H. T. Nyhus, P. Papka, T. Renstrøm, S. Rose, E. Sahin, S. Siem and T. Tornyi, 'Galactic production of ^{138}La: Impact of ^{138,139}La statistical properties', *Physics Letters B*, vol. 744, pp. 268–272, 2015. DOI: `10.1016/j.physletb.2015.03.065`.

[123]   A. Spyrou, S. N. Liddick, A. C. Larsen, M. Guttormsen, K. Cooper, A. C. Dombos, D. J. Morrissey, F. Naqvi, G. Perdikakis, S. J. Quinn, T. Renstrøm, J. A. Rodriguez, A. Simon, C. S. Sumithrarachchi and R. G. T. Zegers, 'Novel technique for Constraining r-Process (n, γ) Reaction Rates', *Physical Review Letters*, vol. 113, no. 23, p. 232 502, Dec. 2014. DOI: `10.1103/PhysRevLett.113.232502`.

[124]   T. G. Tornyi, M. Guttormsen, T. K. Eriksen, A. Görgen, F. Giacoppo, T. W. Hagen, A. Krasznahorkay, A. C. Larsen, T. Renstrøm, S. J. Rose, S. Siem and G. M. Tveten, 'Level density and γ-ray strength function in the odd-odd ^{238}Np nucleus', *Physical Review C*, vol. 89, no. 4, p. 044 323, Apr. 2014. DOI: `10.1103/PhysRevC.89.044323`.

[125]   A. C. Larsen, M. Guttormsen, R. Schwengner *et al.*, 'Experimentally constrained $(p, \gamma)^{89}$Y and $(n, \gamma)^{89}$Y reaction rates relevant to p-process nucleosynthesis', *Physical Review C*, vol. 93, no. 4, p. 045 810, Apr. 2016. DOI: `10.1103/PhysRevC.93.045810`.

[126]   G. M. Tveten, A. Spyrou, R. Schwengner *et al.*, 'Completing the nuclear reaction puzzle of the nucleosynthesis of ^{92}Mo', *Physical Review C*, vol. 94, no. 2, p. 025 804, Aug. 2016. DOI: `10.1103/PhysRevC.94.025804`.

[127]   T. A. Laplace, F. Zeiser, M. Guttormsen *et al.*, 'Statistical properties of ^{243}Pu, and ^{242}Pu(n, γ) cross section calculation', *Physical Review C*, vol. 93, no. 1, p. 014 323, Jan. 2016. DOI: `10.1103/PhysRevC.93.014323`.

[128]   T. Renstrøm, H.-T. Nyhus, H. Utsunomiya *et al.*, 'Low-energy enhancement in the γ-ray strength functions of ^{73,74}Ge', *Physical Review C*, vol. 93, no. 6, p. 064 302, Jun. 2016. DOI: `10.1103/PhysRevC.93.064302`.

[129]   L. Crespo Campo, F. L. Bello Garrote, T. K. Eriksen, A. Görgen, M. Guttormsen, K. Hadynska-Klek, M. Klintefjord, A. C. Larsen, T. Renstrøm, E. Sahin, S. Siem, A. Springer, T. G. Tornyi and G. M. Tveten, 'Statistical γ-decay properties of ^{64}Ni and deduced (n, γ) cross section of the s-process branch-point nucleus ^{63}Ni', *Physical Review C*, vol. 94, no. 4, p. 044 321, Oct. 2016. DOI: `10.1103/PhysRevC.94.044321`.

[130]   L. Crespo Campo, A. Larsen, F. Bello Garrote, T. Eriksen, F. Giacoppo, A. Görgen, M. Guttormsen, M. Klintefjord, T. Renstrøm, E. Sahin, S. Siem, T. Tornyi and G. Tveten, 'Investigating the γ decay of ^{65}Ni from particle-γ coincidence data', *Physical Review C*, vol. 96, no. 1, p. 014 312, 2017. DOI: `10.1103/PhysRevC.96.014312`.

[131]   B. V. Kheswa, M. Wiedeking, J. A. Brown *et al.*, '^{137,138,139}**La**(n, γ) cross sections constrained with statistical decay properties of ^{138,139,140}**La** nuclei', *Physical Review C*, vol. 95, no. 4, p. 045 805, Apr. 2017. DOI: `10. 1103/PhysRevC.95.045805`.

[132] A. Spyrou, A. C. Larsen, S. N. Liddick, F. Naqvi, B. P. Crider, A. C. Dombos, M. Guttormsen, D. L. Bleuel, A. Couture, L. C. Campo, R. Lewis, S. Mosby, M. R. Mumpower, G. Perdikakis, C. J. Prokop, S. J. Quinn, T. Renstrøm, S. Siem and R Surman, 'Neutron-capture rates for explosive nucleosynthesis: the case of ^{68}Ni$(n, \gamma)^{69}$Ni', *Journal of Physics G: Nuclear and Particle Physics*, vol. 44, no. 4, p. 044 002, 2017. DOI: `10.1088/1361-6471/aa5ae7`.

[133] T. Renstrøm, H. Utsunomiya, H. T. Nyhus, A. C. Larsen, M. Guttormsen, G. M. Tveten, D. M. Filipescu, I. Gheorghe, S. Goriely, S. Hilaire, Y.-W. Lui, J. E. Midtbø, S. Péru, T. Shima, S. Siem and O. Tesileanu, 'Verification of detailed balance for γ absorption and emission in Dy isotopes', *Physical Review C*, vol. 98, no. 5, p. 054 310, Nov. 2018. DOI: `10.1103/PhysRevC.98.054310`.

[134] G. M. Tveten, T. Renstrøm, A. C. Larsen *et al.*, 'The gamma-ray strength function of ^{89}Y and ^{90}Y', *arXiv:1804.08109 [nucl-ex]*, Apr. 2018. arXiv: `1804.08109`.

[135] E. Litvinova and N. Belov, 'Low-energy limit of the radiative dipole strength in nuclei', *Physical Review C*, vol. 88, no. 3, p. 031 302, Sep. 2013. DOI: `10.1103/PhysRevC.88.031302`.

[136] R. Schwengner, S. Frauendorf and A. C. Larsen, 'Low-Energy Enhancement of Magnetic Dipole Radiation', *Physical Review Letters*, vol. 111, no. 23, p. 232 504, Dec. 2013. DOI: `10.1103/PhysRevLett.111.232504`.

[137] B. A. Brown and A. C. Larsen, 'Large Low-Energy $M1$ Strength for ^{56,57}Fe within the Nuclear Shell Model', *Physical Review Letters*, vol. 113, no. 25, p. 252 502, Dec. 2014. DOI: `10.1103/PhysRevLett.113.252502`.

[138] S. Karampagia, B. A. Brown and V. Zelevinsky, 'Low energy magnetic radiation enhancement in the $f\_7/2$ shell', *Physical Review C*, vol. 95, no. 2, p. 024 322, Feb. 2017. DOI: `10.1103/PhysRevC.95.024322`.

[139] K. Sieja, 'Electric and Magnetic Dipole Strength at Low Energy', *Physical Review Letters*, vol. 119, no. 5, p. 052 502, Jul. 2017. DOI: `10.1103/PhysRevLett.119.052502`.

[140] A. C. Larsen and S. Goriely, 'Impact of a low-energy enhancement in the γ-ray strength function on the neutron-capture cross section', *Physical Review C*, vol. 82, no. 1, p. 014 318, Jul. 2010. DOI: `10.1103/PhysRevC.82.014318`.

[141] R. Lewis, S. N. Liddick, A. C. Larsen, A. Spyrou, D. L. Bleuel, A. Couture, L. C. Campo, B. P. Crider, A. C. Dombos, M. Guttormsen, S. Mosby, F. Naqvi, G. Perdikakis, C. J. Prokop, S. J. Quinn, T. Renstrøm and S. Siem, 'Experimental constraints on the ^{73}Zn$(n, \gamma)^{74}$Zn reaction rate', *Physical Review C*, vol. 99, no. 3, p. 034 601, Mar. 2019. DOI: `10.1103/PhysRevC.99.034601`.

[142]   S. Goriely and V. Plujko, 'Simple empirical $E1$ and $M1$ strength functions for practical applications', *Physical Review C*, vol. 99, no. 1, p. 014 303, Jan. 2019. DOI: 10.1103/PhysRevC.99.014303.

[143]   M. Krtička, S. Goriely, S. Hilaire, S. Péru and S. Valenta, 'Constraints on the dipole photon strength functions from experimental multistep cascade spectra', *Physical Review C*, vol. 99, no. 4, p. 044 308, Apr. 2019. DOI: 10.1103/PhysRevC.99.044308.

[144]   K. Sieja, 'Shell-model study of the $M1$ dipole strength at low energy in the $A > 100$ nuclei', *Physical Review C*, vol. 98, no. 6, p. 064 312, Dec. 2018. DOI: 10.1103/PhysRevC.98.064312.

[145]   J. E. Midtbø, F. Zeiser, E. Lima, A. C. Larsen, G. M. Tveten, T. Renstrøm, M. Guttormsen and F. L. B. Garrote, 'A new software implementation of the Oslo method with complete uncertainty propagation', *arXiv:1904.13248 [physics.comp-ph, nucl-ex,]*, Apr. 2019. arXiv: 1904.13248.

[146]   N. Bohr, 'Neutron Capture and Nuclear Constitution', *Nature*, vol. 137, pp. 344–348, Feb. 1936. DOI: 10.1038/137344a0.

[147]   M. Guttormsen, A. Bürger, T. E. Hansen and N. Lietaer, 'The SiRi particle-telescope system', *Nuclear Instruments and Methods in Physics Research Section A: Accelerators, Spectrometers, Detectors and Associated Equipment*, vol. 648, no. 1, pp. 168–173, Aug. 2011. DOI: 10.1016/j.nima.2011.05.055.

[148]   M. Guttormsen, A. Atac, G. Løvhøiden, S. Messelt, T. Ramsøy, J. Rekstad, T. F. Thorsteinsen, T. S. Tveter and Z. Zelazny, 'Statistical Gamma-Decay at Low Angular Momentum', *Physica Scripta*, vol. T32, pp. 54–60, Jan. 1990. DOI: 10.1088/0031-8949/1990/T32/010.

[149]   M. Guttormsen, T. S. Tveter, L. Bergholt, F. Ingebretsen and J. Rekstad, 'The unfolding of continuum γ-ray spectra', *Nuclear Instruments and Methods in Physics Research A*, vol. 374, pp. 371–376, 1996. DOI: 10.1016/0168-9002(96)00197-0.

[150]   M. Guttormsen, F. Zeiser, J. E. Midtbø, V. W. Ingeberg and A.-C. Larsen, *oslocyclotronlab/oslo-method-software: Oslo Method v1.1.2*, Aug. 2018. DOI: 10.5281/zenodo.2318646.

[151]   V. Blobel, 'Chapter 6: Unfolding', en, in *Data Analysis in High Energy Physics: A Practical Guide to Statistical Methods,* New Jersey, USA: John Wiley & Sons, Inc., 2013.

[152]   M. Guttormsen, T. Ramsoy and J. Rekstad, 'The first generation of γ-rays from hot nuclei', *Nuclear Instruments and Methods in Physics Research*, vol. 255, pp. 518–523, 1987.

[153] Dirac Paul Adrien Maurice and Bohr Niels Henrik David, 'The quantum theory of the emission and absorption of radiation', *Proceedings of the Royal Society of London. Series A, Containing Papers of a Mathematical and Physical Character*, vol. 114, no. 767, pp. 243–265, Mar. 1927. DOI: `10.1098/rspa.1927.0039`.

[154] E. Fermi, *Nuclear Physics*, en. Chicago: University of Chicago Press, 1950.

[155] P. Ring and P. Schuck, *The Nuclear Many-Body Problem*, en, ser. Theoretical and Mathematical Physics, The Nuclear Many-Body Problem. Berlin Heidelberg: Springer-Verlag, 1980.

[156] M. Guttormsen, L. A. Bernstein, A. Bürger, A. Görgen, F. Gunsing, T. W. Hagen, A. C. Larsen, T. Renstrøm, S. Siem, M. Wiedeking and J. N. Wilson, 'Observation of large scissors resonance strength in actinides', *Phys. Rev. Lett.*, vol. 109, p. 162 503, 16 Oct. 2012. DOI: `10.1103/PhysRevLett.109.162503`.

[157] F. Zeiser, G. M. Tveten, G. Potel *et al.*, 'Restricted spin-range correction in the Oslo Method: The example of nuclear level density and γ-ray strength function from (d,p) 240Pu', *arXiv:1904.02932 [nucl-ex]*, Apr. 2019. arXiv: `1904.02932`.

[158] F. Zeiser, G. Potel, G. M. Tveten *et al.*, 'Impact of restricted spin-ranges in the Oslo Method: The example of (d,p) 240Pu', *arXiv:1902.02966 [nucl-ex]*, Feb. 2019. arXiv: `1902.02966`.

[159] F. Zeiser and J. E. Midtbø, 'Including the $z(E_x, E_\gamma)$ correction factor in the Oslo method *(in preparation)*', 2019.

[160] J. Kopecky and M. Uhl, 'Test of gamma-ray strength functions in nuclear reaction model calculations', *Physical Review C*, vol. 41, no. 5, pp. 1941–1955, May 1990. DOI: `10.1103/PhysRevC.41.1941`.

[161] A. Schiller, L. Bergholt, M. Guttormsen, E. Melby, J. Rekstad and S. Siem, 'Extraction of level density and γ strength function from primary γ spectra', *Nuclear Instruments and Methods in Physics Research, Section A: Accelerators, Spectrometers, Detectors and Associated Equipment*, 2000. DOI: `10.1016/S0168-9002(99)01187-0`.

[162] J. E. Midtbø, F. Zeiser and E. Lima, *oslocyclotronlab/ompy: OMpy v0.2-beta*, Apr. 2019. DOI: `10.5281/zenodo.2654604`. [Online]. Available: `https://zenodo.org/record/2654604` (visited on 05/05/2019).

[163] M. J. D. Powell, 'An efficient method for finding the minimum of a function of several variables without calculating derivatives', *The Computer Journal*, vol. 7, no. 2, pp. 155–162, Jan. 1964. DOI: `10.1093/comjnl/7.2.155`.

[164] E. Jones, T. Oliphant, P. Peterson *et al.*, *SciPy: Open source scientific tools for Python*, en, 2001. [Online]. Available: `http://www.scipy.org/` (visited on 06/05/2019).

[165] A. C. Larsen, M. Guttormsen, M. Krtička, E. Běták, A. Bürger, A. Gör-gen, H. T. Nyhus, J. Rekstad, A. Schiller, S. Siem, H. K. Toft, G. M. Tveten, A. V. Voinov and K. Wikan, 'Analysis of possible systematic errors in the Oslo method', *Physical Review C*, vol. 83, no. 3, p. 034 315, Mar. 2011. DOI: `10.1103/PhysRevC.83.034315`.

[166] A. Gelman, J. Carlin, H. Stern, D. Dunson, A. Vehtari and D. Rubin, *Bayesian Data Analysis, Third Edition*, en, ser. Chapman & Hall/CRC Texts in Statistical Science. Taylor & Francis, 2013.

[167] T. Shizuma, H. Utsunomiya, P. Mohr, T. Hayakawa, S. Goko, A. Mak-inaga, H. Akimune, T. Yamagata, M. Ohta, H. Ohgaki, Y.-W. Lui, H. Toyokawa, A. Uritani and S. Goriely, 'Photodisintegration cross section measurements on ^{186}W, ^{187}Re, and ^{188}Os: Implications for the Re-Os cosmochronology', *Physical Review C*, vol. 72, no. 2, p. 025 808, Aug. 2005. DOI: `10.1103/PhysRevC.72.025808`.

[168] A. Simon, S. J. Quinn, A. Spyrou *et al.*, 'SuN: Summing NaI(Tl) gamma-ray detector for capture reaction measurements', *Nuclear Instruments and Methods in Physics Research, Section A: Accelerators, Spectromet-ers, Detectors and Associated Equipment*, 2013. DOI: `10.1016/j.nima.2012.11.045`.

[169] S. N. Liddick, A. Spyrou, B. P. Crider *et al.*, 'Experimental Neutron Capture Rate Constraint Far from Stability', *Physical Review Letters*, p. 242 502, 2016. DOI: `10.1103/PhysRevLett.116.242502`.

[170] S. Frauendorf, 'Spontaneous symmetry breaking in rotating nuclei', *Reviews of Modern Physics*, vol. 73, no. 2, pp. 463–514, Jun. 2001. DOI: `10.1103/RevModPhys.73.463`.

[171] D. W. Hogg, J. Bovy and D. Lang, 'Data analysis recipes: Fitting a model to data', *arXiv:1008.4686 [astro-ph]*, Aug. 2010. arXiv: `1008.4686`.

[172] J. Salvatier, T. V. Wiecki and C. Fonnesbeck, 'Probabilistic programming in Python using PyMC3', *PeerJ Computer Science*, vol. 2, e55, Apr. 2016. DOI: `10.7717/peerj-cs.55`.